LAWRENCE
LIVERMORE
NATIONAL
LABORATORY

UCRL-TR-216659

April 25, 2003, FY2003 Progress Summary and FY2002 Program Plan, Statement of Work and Deliverables for Development of High Average Power Diode-Pumped Solid State Lasers,and Complementary Technologies, for Applications in Energy and Defense

W. Meier, C. Bibeau

October 28, 2005

Disclaimer

This work was performed under the auspices of the U.S. Department of Energy by University of California, Lawrence Livermore National Laboratory under Contract W-7405-Eng-48.

UCRL-TR-216659

April 25, 2003

FY2003 Progress Summary
and
FY2002 Program Plan,
Statement of Work and Deliverables

For

Development of High Average Power Diode-Pumped Solid State Lasers, and Complementary Technologies, for Applications in Energy and Defense

Prepared by
Editor: Dr. Camille Bibeau
Project Leader for Mercury Laser
Phone: (925) 422-7798
bibeau1@llnl.gov

Presented to
Dr. Ralph Schneider, DP/DOE,
Virtual Office of Inertial Fusion Energy

Continuation of DOE Contract Number DE-AI03-94SF19892

For further information contact:

Dr. Stephen A. Payne
Associate LS&T Program Leader
Phone: (925) 423-0570
payne3@llnl.gov
or
Dr. John Lindl
Fusion Energy Program Leader
Phone: (925) 422-5430
lindl1@llnl.gov

Lawrence Livermore National Laboratory
Livermore, CA 94550

This work was performed under the auspices of the U. S. Department of Energy by the University of California, Lawrence Livermore National Laboratory under Contract No. W-7405-Eng-48.

TABLE OF CONTENTS

1. INTRODUCTION

The High Average Power Laser Program (HAPL) is a multi-institutional, synergistic effort to develop inertial fusion energy (IFE). This program is building a physics and technology base to complement the laser-fusion science being pursued by DOE Defense programs in support of Stockpile Stewardship. The primary institutions responsible for overseeing and coordinating the research activities are the Naval Research Laboratory (NRL) and Lawrence Livermore National Laboratory (LLNL). The current LLNL proposal is a companion document to the one submitted by NRL, for which the driver development element is focused on the krypton fluoride excimer laser option. The NRL and LLNL proposals also jointly pursue complementary activities with the associated rep-rated laser technologies relating to target fabrication, target injection, final optics, fusion chamber, target physics, materials and power plant economics.

This proposal requests continued funding in FY03 to support LLNL in its program to build a 1 kW, 100 J, diode-pumped, crystalline laser, as well as research into high gain fusion target design, fusion chamber issues, and survivability of the final optic element. These technologies are crucial to the feasibility of inertial fusion energy power plants and also have relevance in rep-rated stewardship experiments.

The HAPL Program pursues technologies needed for laser-driven IFE. System level considerations indicate that a rep-rated laser technology will be needed, operating at 5-10 Hz. Since a total energy of ~2 MJ will ultimately be required to achieve suitable target gain with direct drive targets, the architecture must be scaleable. The Mercury Laser is intended to offer such an architecture. Mercury is a solid state laser that incorporates diodes, crystals and gas cooling technologies.

In addition to the laser physics and engineering, additional areas to be pursued include target physics, chambers, system studies and final-optic/first-wall x-ray ablation. Target physics includes advanced direct-drive implosions and determination of the "threat spectra" (i.e. x-ray, ions, debris, n^o and gammas). The chamber study of the fast-ignitor has been explored to determine its potential for IFE. Radiation (n^o, γ, x-ray) physics studies of reflective and transmissive optics are being performed. A new initiative in x-ray ablation of optics and the chamber first wall has been started based on the use of a rep-rated z-pinch source procured from PLEX LLC; this device is in the process of being activated. A detailed break-out of tasks and costs are described in Sections 3 and 4.

The end-goal of the Mercury Laser is to demonstrate 10% electrical efficiency at 10 Hz and 100 J with a 2-10 ns pulse length at the 1.047 um wavelength and incorporate frequency conversion to 3ω with beam smoothing. The efficiency and rep-rate requirement relate directly to inertial fusion energy objectives. The primary FY03 goal is to complete the construction and activation of the 1ω laser system. We will also begin developing the beam quality technology (spectral sculpting, bandwidth, temporal formatting, deformable mirror, transmissive phase masks) needed for Mercury to be a true user facility and for the full scale IRE program. When completed, Mercury will allow rep-rated target experiments with multiple target chambers for high energy density physics research.

During FY02 we achieved a significant milestone by activating one power amplifier filled with five Yb:S-FAP slabs and producing 21 joules at 10 Hz repetition rate. This accomplishment required: four 80 kW laser diode arrays, five full-size Yb:S-FAP crystals, alignment of front-end laser through a four-pass angularly-multiplexed optical train, a computer control system, and a suite of optical diagnostics. Finally these experiments have been benchmarked against computational codes. With the attaining of this milestone, many of the highest risk issues associated with realizing 100 J at 10 Hz for 3 nsec have been greatly reduced in that we have demonstrated: functionality at the component-level, viability of the basic optical design, and integrated operation at the system-level.

The Mercury Laser builds on three decades of R&D experience with flash lamp-pumped Nd:Glass fusion lasers. However, there are many crucial differences between the inherent design to the National Ignition Facility (NIF) and the one being pursued for solid state fusion laser drivers. The differences arise because of the additional requirements imposed by IFE such as: >10x higher wallplug efficiency and ~10^5x higher repetition rate. These enhancements are needed while at the same time retaining the beam-smoothness needed for direct-drive targets and realizing an architecture that is suitable to scaling to ~2 MJ at reasonable cost and complexity.

The main technical issues associated with the repetition-rate increase involve the management of the thermal wave front and the statistically greater probability of optical damage. We have verified that the gas-cooling technique for removing heat from the laser slabs gives rise to manageable temperature gradients. This is the case because the thermal gradients in our design are predominantly *in the propagation direction*, which means that they are integrated away by the beam. The more pressing issue is the risk of optical damage, which we have mitigated through the optical design and selection of the gain medium. Management of optical damage is a subtle and complex issue, and a significant "safety factor" is needed at high repetition rates. A highly simplified drawing of the optical layout of NIF and Mercury is pictured below in Fig. 1.1.

In evolving from NIF to Mercury we have incorporated several changes to the architecture:

- Nd:glass is replaced with Yb:S-FAP, thereby reducing the saturation fluence from $5.4\ \mathrm{J/cm^2}$ to $3.8\ \mathrm{J/cm^2}$.
- Laser slabs are effectively "thinned" since the diode output is monochromatic and less path length is needed for adequate pump absorption.
- Laser slabs are rearranged to be juxtaposed and parallel, so that they are all close to an optically imaged plane, thereby minimizing the beam modulation.
- Telescope lenses are moved adjacent to the slabs helping to reduce beam modulation.
- The beam is expanded after the last pass to reduce the fluence at the "out-of-relay" lens.

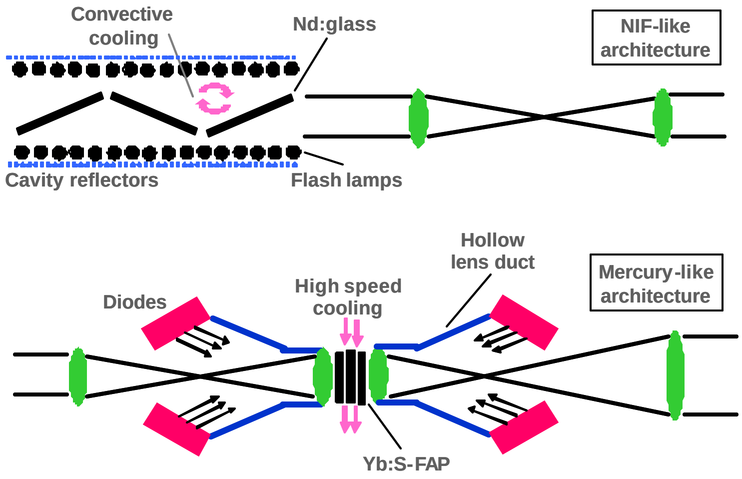

Fig. 1.1 Simplified schematic diagrams of NIF-like and Mercury architectures.

To further clarify the difference in the design strategy of the Mercury Laser compared to NIF, Table 1.1 contains an overview of the major features, the reason for the change, and the new challenges which arise. We have made much progress regarding the challenges enunciated in Table 1.1, and we are optimistic that they will be resolved.

In order to assure that the *efficiency* of the laser is as high as possible:

- Flash lamps are replaced with laser diode arrays for the purposes of reliability, pump brightness, and efficient delivery and absorption of the light into the gain media.
- Extraction occurs at a fluence near $3F_{sat}$, to assure that the stored energy is efficiently removed. (NIF is operated at about $1.5F_{sat}$ at 3 ns.
- The amplifier slabs are pumped longitudinally (in the same direction as the laser beam) for optimal overlap of the pumped and extracted regions.

Overall, the architectural changes described in Fig. 1.1 and Table 1.1 relate to the need for greater efficiency, reliability (owing to the high rep-rate), and management of diode costs (by deploying a gain medium with a long storage time).

Table 1.1: Comparison of Mercury and NIF design strategies

Feature	**NIF**	**Mercury**	**Basis for change**	**Challenges**
Pump source	Flash lamps	Laser diodes	- Efficiency - Reliability - Monochromatic (less heating)	- Cost of diodes
Pump delivery	Side-pumped in reflective cavity	Longitudinally-pumped using hollow reflective mirrors	- Intensity for quasi- three level laser operation - Efficient absorption - Polarized pump light desired	- Alignment sensitive to laser beam clipping
Extraction geometry	Perpendicular to slab face	Brewster's angle orientation	- Consistency with pump geometry	- Slabs slightly wedged to avoid ghosts
Gain medium	Nd:glass	Yb:S-FAP	- Longer storage time - 40% higher gain cross-section (mitigates damage) - Uniaxial (averts thermally-induced birefringence)	- Growth of large crystals difficult - ASE and SRS in large aperture
Cooling	Convection	High-speed helium	- 10 Hz repetition rate	- Helium pumping power (for IFE)

The selection of Yb:S-FAP as the gain medium was the result of an extensive and systematic search among hundreds of potential candidates. Table 1.2 lists the five top leading candidates along with brief descriptions as to why they were not chosen.

Table 1.2 Comparison of gain media for potential use in Mercury.

Gain Medium	**Saturation Fluence F_{sat} (J/cm^2)**	**Storage time t_{st} (msec)**	**Nonlinear index n_2 (10^{-16} cm^2/W)**	**Most pressing problem**
Ideal medium	~ 3 - 5	> 1 – 2	< 3 - 4	- Easy to fabricate
Yb:S-FAP	3.8	1.15	4.1	- Difficult to grow
Nd:Phosphate-Glass	5.4	0.4	2.8	- Shorter τ_{st} impacts diode cost
Yb:Phosphate-Glass	60	1.0	2.8	- $3F_{sat}$ too large for damage-free operation
Yb:YAG	9.6	0.95	6.3	- Nonlinear distortions due to high F_{sat} and n_2
Nd:YAG	0.7	0.24	6.3	- high ASE losses from low F_{sat}

The scope of the current proposal is consistent with the goals outlined in the DPSSL five-year program plan, which was developed to create a pathway for scientific and engineering readiness to build and Integrated Research Experiment (IRE). The IRE, together with data on IFE technologies (e.g. chamber and final optic survival) and target physics validation on the NIF, is thought to be sufficient for proceeding to the next step of integration for making IFE a reality. The plan calls for critical component development (Yb:S-FAP crystals, diodes, Pockels cell, frequency converter), demonstration of the 100 J Mercury Laser facility, and a multi-kilojoule IRE design. A broad view of the DPSSL plan is shown in Figure 2 below.

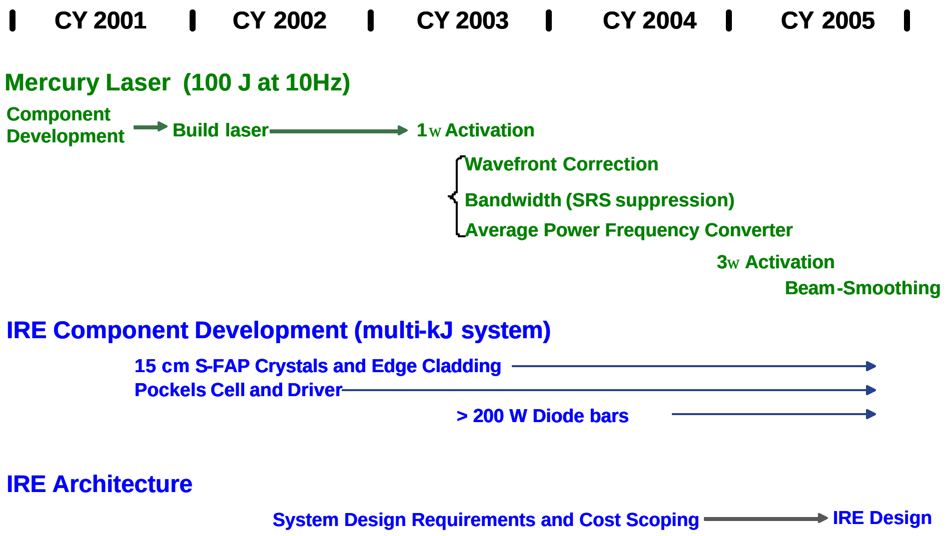

Fig. 1.2 Five-Year Plan for validation rep-rated DPSSL technology for IFE.

To minimize the cost of future DPSSL systems, the cost of the diode arrays needs to be reduced as much as possible. Our estimation suggests that τ_{st} ~1 msec for the gain medium storage time represents the lower end of acceptable diode costs. Assuming the laser functions with ~ 20% optical-to-optical efficiency, the diode price would need to be reduced to ~ \$1/W_{peak} for the IRE, and ~5¢/W_{peak} for IFE. The number of beam-lines is predicated on the maximum energy/beam that is possible. For solid state lasers, the scaling of the aperture is most fundamentally limited by parasitic optical processes occurring transverse to the beam propagation (i.e. amplified spontaneous emission, parasitic oscillations, stimulated Raman and Brillouin scattering). We are in the process of evaluating these effects. From a practical point of view, greater energy per beam-line simplifies the overall architecture of the fusion laser, by reducing the total number of components. It is thought that, although the larger optical elements are more expensive, the reduced complexity of the system outweighs this disadvantage. Most of the cost lies in the diode arrays in any case. Table 1.3 details our rough projections for future DPSSLs that may be useful for IFE and Stockpile Stewardship.

Table 1.3 Comparison of Mercury Laser to potential future laser systems

Laser System	**Energy per beam-line**	**Clear aperture size (cm^2)**	**Number of beam-lines**	**Diode Cost**
Mercury	100 J	15	1	\$5/W_{peak} (actual)
Venus	1 – 5 kJ	150 - 500	1	~ \$1/W_{peak}
Terra	1 – 5 kJ	150 - 500	~ 8	~ 25¢/W_{pea}
Helios	1 – 5 kJ	150 - 500	400 - 2000	~ 5¢/W_{peak}

The high average power lasers may be required to operate at ~ 10 Hz, or simply in a shots-on-demand mode. Below we list the potential missions that may be served by the development of advanced target shooters and laser drivers, such as the Mercury Laser and its successors:

- *Energy*
- ➢ Driver development for achieving the scalability, efficiency, rep-rate, beam smoothness, and reliability required for power plant operation
- ➢ Develop target tracking and injection, beam transport through chamber gases, and debris mitigation
- ➢ X-ray ablation studies of candidate first-wall materials
- ➢ Studies of beam uniformity (for direct drive) with time-resolved x-ray imaging of irradiated foils
- ➢ Development of a radiation-hard final optic

- *National Security*
- ➢ Ultra-precise equation-of-state and shock break-out measurements, as well as shock-induced phase change measurements, based on use of statistical averaging of x-ray probes
- ➢ Fundamental pump-probe studies of nonlinear laser-plasma interactions (e.g. stimulated Raman and Brillouin scattering, and Thomson scattering probes) relevant in ICF targets
- ➢ Three-dimensional x-ray tomographic imaging of nuclear components
- ➢ Ultra-precise atomic absorption measurements based on extensive statistical averaging, for improved radiation transport modeling

- *National Ignition Facility technology*
- ➢ Large area optical damage testing of NIF components
- ➢ Calibration, fine-tuning and development of NIF x-ray and optical diagnostics
- ➢ Debris assessment for various target materials and laser intensities
- ➢ Pre-staging of NIF experiments, based on future availability of kJ-class "cheap shots"
- ➢ Definition of laser technology for next-generation stockpile stewardship

- *Science Spin-Offs*
- ➢ Development of laboratory x-ray lasers, including collisionally-excited plasmas
- ➢ Relativistic propagation of laser beams in plasmas
- ➢ Laser technology suitable for the next generation linear collider
- ➢ Three-dimension x-ray microscopy of biological and electronics samples
- ➢ Synchrotron-like sources with higher brightness and accessibility

- *Governmental Spin-Offs*
- ➢ Development of laser components such as high performance, low-cost laser diode arrays, large crystals, and cooling technology relevant to solid state laser tactical weapons (ground / ship / aircraft point-defense)
- ➢ Yb:S-FAP has been featured in many SBIRs
- ➢ Space debris clearing by deflection (i.e. repetitive plasma impulse on debris in orbit)
- ➢ Power beaming to recharge satellites in earth's shadow to prolong solar cell lifetime

- *Industrial Spin-Offs*
- ➢ Technology-transfer of diode technology to several companies
- ➢ Peening of metal parts

The development of the Mercury Laser and the evaluation of fusion chamber, final optic, and target technologies, all have dual use applications to the defense and energy missions of the Department of Energy.

2. SUMMARY PROGRESS IN FY 2002

TABLE OF CONTENTS

2. 1 DPSSL Development

2.1.1 Mercury Laser Executive Summary

Our main goal this year was to extract energy from an amplifier populated with Yb:S-FAP slabs and diagnose the performance using a full suite of diagnostics. With four backplane arrays and five Yb:S-FAP slabs, we were able to extract up to 21 joules of energy at a 10 Hz repetition rate. The Yb:S-FAP slabs were mounted in aerodynamic aluminum vane structures to allow turbulent helium gas flow across the faces. Six diagnostic packages including two four damage detection sensors were activated and used during operation. The experiments involved sending a seed beam through the amplifier and optical train in a 4-pass angular multiplexed alignment scheme. In order to correct for static phase distortions incurred during crystal fabrication, a phase corrector plate was custom fabricated at LLNL using a novel wet etch technique and installed. The corrector plate was able to improve the beam quality by a factor of three. A a full beam Pockels cell was developed for suppressing parastics and was successfully tested in the system.

A picture of the laboratory is shown below. The control system and diagnostics monitors are located in the background. These systems were fully exercised for 10 Hz rep-rated operation and provided real time feedback to the operator during the experiments.

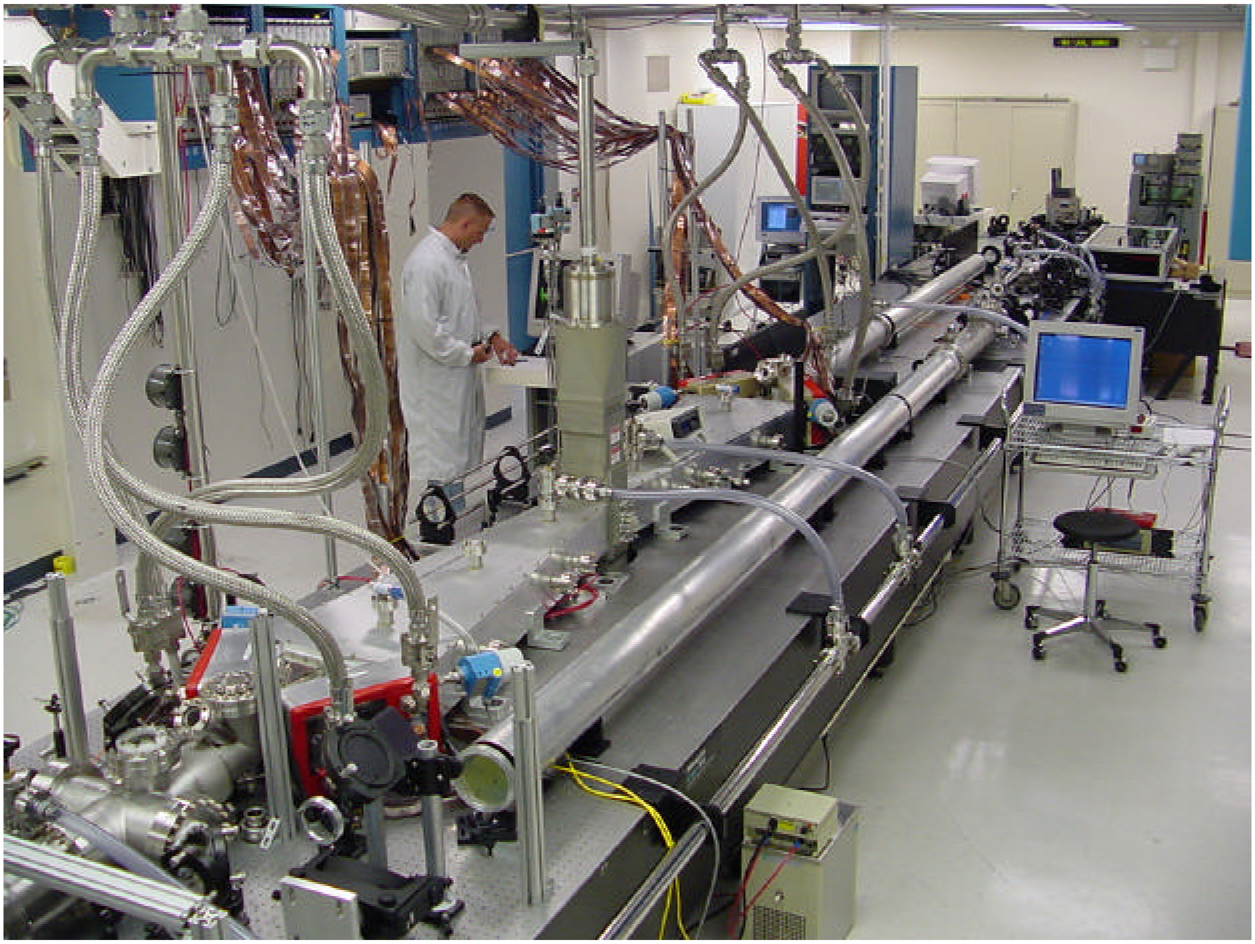

2.1.1.1 Mercury laser laboratory.

The growth and fabrication of the Yb:S-FAP slabs constituted another major element of our program objectives. Our goal was to produce at least seven 4x6 cm^2 crystalline slabs. Five were successfully fabricated and installed in the system while the other two are currently in fabrication. Twelve boules are currently in the production queue. A major improvement to the fabrication process was gained by switching to a water jet cutting process and a new cutting geometry. Results thus far indicate a 100 % cutting rate with these new techniques. Growth efforts at Northrop-Grumman, our industrial collaborator, resulted in the production of three 6.5 cm diameter boules. These represent the first large diameter Yb:S-FAP boules to be grown with the Czochralski method. We are encouraged by these results and are fine tuning the process to eliminate the index variations or striations with methods previously used in smaller boules. The LLNL effort focused on producing smaller diameter boules. These boules yielded half size slabs that were bonded together by Onyx to form full size parts. The bonding process created wavefront distortions directly along the bonded region. However, better alignment and heat treatment methods are being pursued to eliminate these distortions. In the final configuration, the Mercury laser will require two amplifiers a total of 14 slabs.

The remaining diode bars needed to pump a second amplifier assembly were purchased from Coherent Inc. and packaged at LLNL using a state of the art technology required to cool the diode bars and maintain the stringent requirements pertaining to peak power, bandwidth, wavelength chirp and reliability. This year over 140, 23-diode-bar packages were fabricated and mounted on a copper-cooling block called a backplane. Each backplane produced 80 kW of peak power. The pulse power units were modified by the manufacturer to improve performance and operated with a computer control system.

The following sections discuss the above accomplishments in more technical detail and are followed by a proposal for FY03 plans and a budget request.

2.1.2 Conceptual Layout

The conceptual layout for the full laser design is shown in Fig. 2.1.2.1. The layout incorporates an angularly multiplexed beam path. The front-end laser is injected off-axis into the first amplifier. After the beam passes through the second amplifier, it is reflected from the end mirror and returns to a different spatial location near its original injection location (see image inset). A set of mirrors in the "beam reverser" path are used to reinject the beam back into the amplifier chain for two additional passes making a total of 4 passes through the system. Several telescopes are used to relay a spatially smooth beam profile from amplifier to amplifier to reduce the probability of damage. (Fig. 2.1.2.2). A Pockels cell will be located in the reverser optics to help stop unwanted parasitic reflections for being amplified along with the main beam.

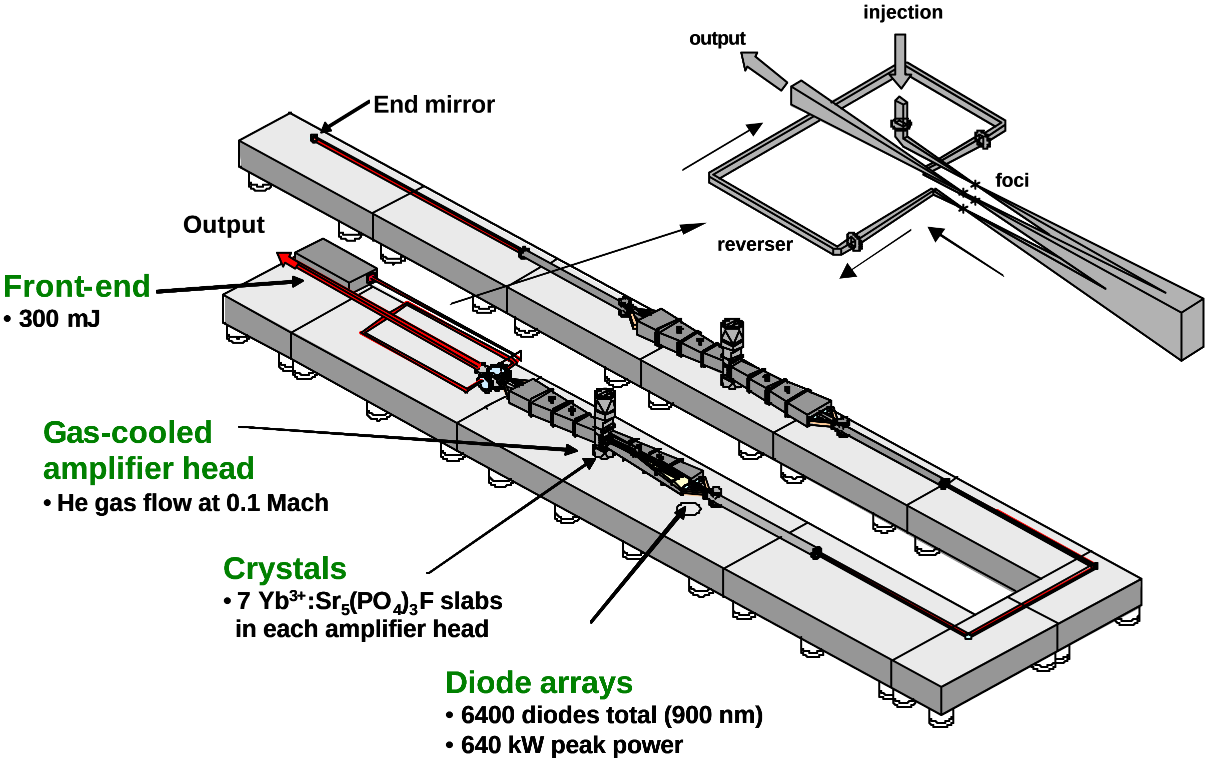

Fig. 2.1.2.1 Mercury laser system layout and enlargement of injection and reverser system.

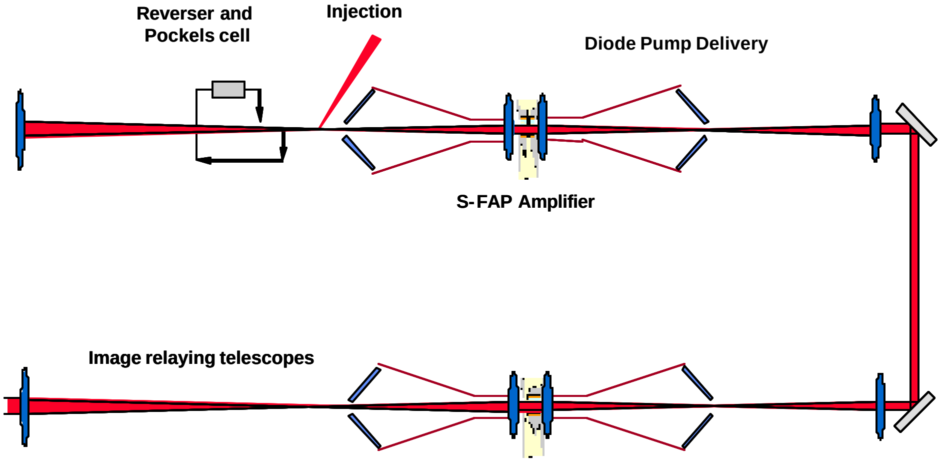

Fig. 2.1.2.2 Schematic top view of the optical layout.

The amplifier head is optically pumped from both sides. The dual-ended pumping design allows for uniform pumping and thermal loading on the crystals. The light from the diode array light is concentrated down with hollow reflective optics that help to homogenize the spatial profile of the pump beam. The optics are coated on the inside surfaces with a silver coating that have high reflectivity (>99%) at grazing incidence angles. Up to 80% of the diode light is expected to reach the first amplifier slab. Each of the seven amplifier slabs (Fig. 2.1.2.3a) are mounted or potted into aerodynamic aluminum vane elements as shown in Fig. 2.1.2.3. The seven vanes are precision mounted within a helium gas flow assembly.

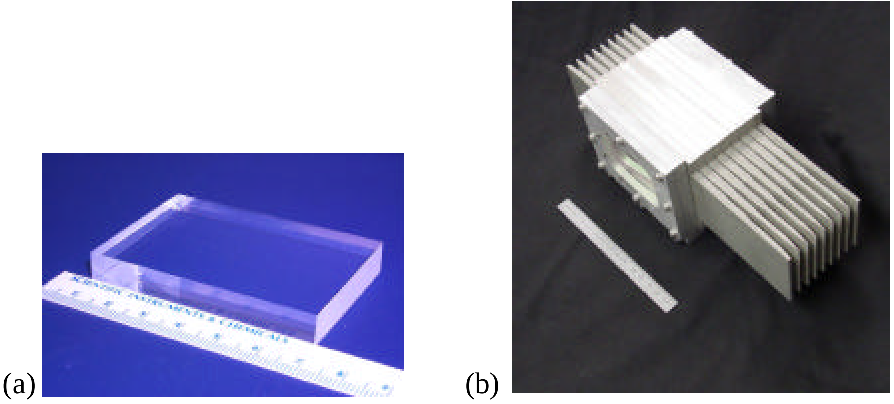

Fig. 2.1.2.3 (a) Yb:S-FAP slab (b) Aluminum vanes

The diode pump arrays on either side of the amplifier consist two 6x6 arrays of tiles. The arrays emit light with a divergence of 1x10 degrees. The spacing between the arrays shown in Figure 2.1.2.4 allows the main laser beam to pass through. Since the diode pump delivery and laser beam optics are coupled this allows the pump-amplifier module to be quite compact. However this also requires careful attention stray light analysis to track unwanted reflections.

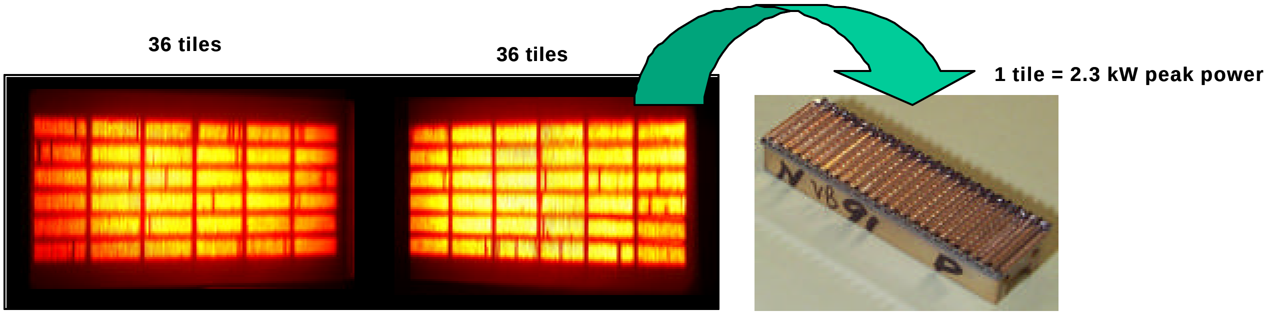

Fig. 2.1.2.4 A picture of diode tiles (pump laser) firing producing up to 160 kW of peak power at 900 nm.

2.1.3 Integrated Experiments

Our FY2002 tasks were:

- Integrated operation of the laser system at 20 J and 10 Hz with Yb:S-FAP slabs in one amplifier.
- Comparison of experimental data and theoretical predictions

During the past year, the Mercury gas cooled amplifier was tested under a variety of operating conditions. As the Yb:S-FAP amplifier slabs became available, we began replacing the Nd:Glass slabs with Yb:S-FAP and increasing the rep-rate. The table below lists the three set of experiments that were conducted and the corresponding power and energy obtained from a single amplifier. We will focus on the Configuration III experiments since they most closely represent the ideal amplifier configuration of 7 Yb:S-FAP slabs.

Table 2.1.3.1 Summary of experiments

Details	**Configuration I**	**Configuration II**	**Configuration III**
Gain media	7 Nd:Glass 0 Yb:S-FAP	3 Nd:Glass 4 Yb:S-FAP	5 Yb:S-FAP 2 undoped glass
Slab shape	Parallel faces	Wedged faces	Wedged faces
Single pass gain	1.23	3.6	4.3
Maximum energy attained (J)	-	21	31.6
Maximum rep-rate attained (Hz)	1	3.3	10
Maximum power attained (W)	-	36.3	200
Measure depolarization	-	~ 10%	< 1%

Gas cooled amplifier flow measurements with wedged slab geometry

New amplifier vanes were fabricated to allow for slabs with a 0.5 degree overall wedge (Fig. 2.1.3.1). The wedge was introduced to reduce etalon reflections from imperfect AR coatings and to steer these reflections off the system axis to prevent amplified buildup. The amplifier slabs (4x6x~0.75 cm^3) are mounted into aerodynamic aluminum vane elements as shown in Fig. 2.1.3.1a below. The seven vanes are precision mounted into a cassette (Fig. 2.1.3.1b) that is inserted into the helium gas flow assembly. The fabricated vanes were delivered and met all mechanical tolerances (Fig. 2.1.3.1c).

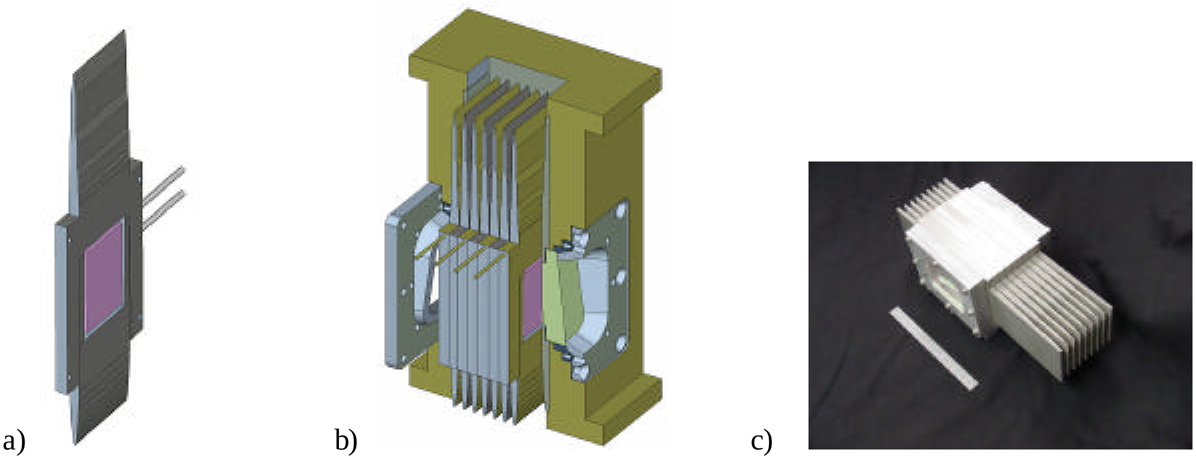

Fig. 2.1.3.1 a) Single vane element schematic, b) Seven vane elements mounted into amplifier cassette, c) Solid vanes for flow and vibration testing.

Two set vanes were fabricated; with and without cutouts for the slabs. The solid vanes (no cut outs) were used to test the gas flow conditions under optimal conditions. Tests were conducted with helium flowing at 100 cubic feet per minute (cfm) and at an absolute pressure of 45 psi. All support equipment including diode chillers and power supplies were also operated to give a true "operations" conditions. The rms deviation of the pressure drop from channel to channel was measured to be 3.7% (Fig. 2.1.3.1a). The goal was 5%.

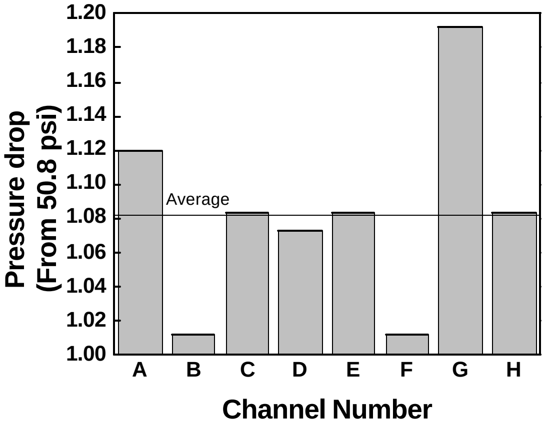

Fig. 2.1.3.2 a Measured pressure drop within a channel for solid vanes; rms = 0.037 psi

The differential pressure drops between channels was measured for both solid and cutout vanes. The rms differential between two adjacent solid vanes was measured to be 0.058 psi, and for the potted vanes was 0.054 psi (Fig. 2.1.3.2b&c). The similarity in results gave us confidence that the potting procedure does not introduce any large scale flow disturbances.

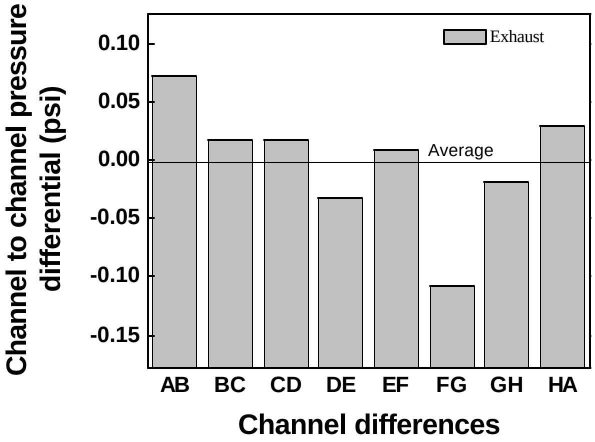

Fig. 2.1.3.2 b Measured differential pressure drops between channel for solid vanes; rms = 0.058 psi

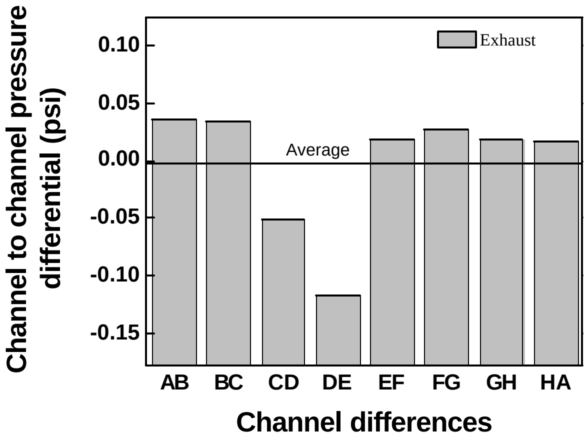

Fig. 2.1.3.2 c) Measured differential pressure drops between channel for vanes with slabs inserted; rms = 0.054 psi

Front end laser

The front-end laser is based on a Q-switched Nd:YLF oscillator which operates a 1047 nm and produces pulse energies of 40 mJ with temporal FWHM of 20 ns at a frequency of 10 Hz. The oscillator has a Gaussian spatial profile with FWHM of 1 mm at the output and an M^2 of 1.5. The beam is double passed through one Nd:YLF amplifier and then image relayed and single passed through a second Nd:YLF amplifier. The output energy of the front end is roughly 800 mJ in a nearly flat-topped 8 mm beam. The front-end laser then passes through a Pockels cell, which is used to switch out desired pulses to the amplifier section, as well as protect the front end from parasitics generated in the main laser. The spatial profile of the beam is then magnified by a factor of 9 and anamorphically compressed by a factor of 0.5 in one axis to produce an elliptical flat-topped beam to more closely match the 3x5 cm^2 beam size requirements. The final step in beam shaping is passing the elliptical beam through a saw-toothed aperture.

The saw toothed design softens the hard edges to minimize the growth of diffraction ripples at the edge of the beam. After accounting for beam shaping losses the remaining energy is 360 mJ. A set of pointing and centering mirrors send the beam into the main laser telescope at the required 5 mrad multiplexing angle.

Wavefront Measurements

The static wavefront of the beam after passing through the main laser was measured to be 3.7 waves. The largest contributing element of the distortion is from the vertical bonded region in the slabs. Since the slabs are fabricated from two sub-size pieces joined together through a process called diffusion bonding, the resulting phase profile is distorted along the bond line as seen in Fig. 2.1.3.3

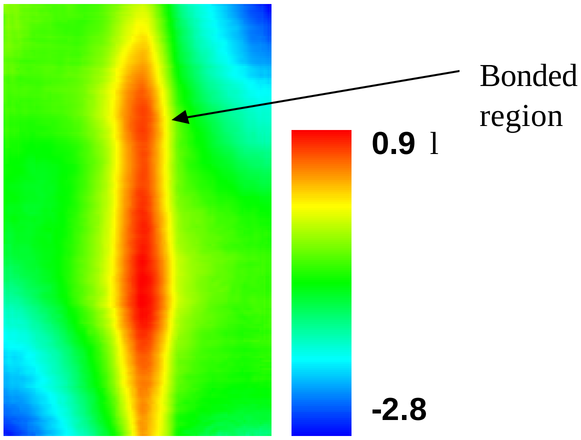

Fig. 2.1.3.3 Static wavefront of the 5 S-FAP and 2 SK15 slab amplifier

Until the crystals can be grown large enough to harvest full size slabs we will have to correct for this phase distortion with thin phase corrector plate placed immediately after the amplifier. The phase plates are made at LLNL using an hydrofluoric acid etch solution in an automatic feedback loop with an interferometer. Arbitrary wavefront distortions can be directly written into glass plates (Fig. 2.1.3.4 a&b). The hydrofluoric acid is pumped to the glass surface where it pools like the top of a fountain. A combination of alcohol vapor and hydrophilic collars are used to control the size and shape of the "fountain head" and how it wets the surface. The size of the tool defines the minimum resolvable spatial frequency, while the etchant concentration and flow rate control the rate and depth of cuts into the surface. Depending on tool size and spatial frequency, the group claims to be able to cut smooth profiles 7 microns deep with a minimum tool size of approximately 1 mm. Using this technology, a phase plate was generated with the opposite sign relative to the static wavefront distortion. A screen capture of their interferometric analysis of our phase plate is shown in Fig. 2.1.3.4c.

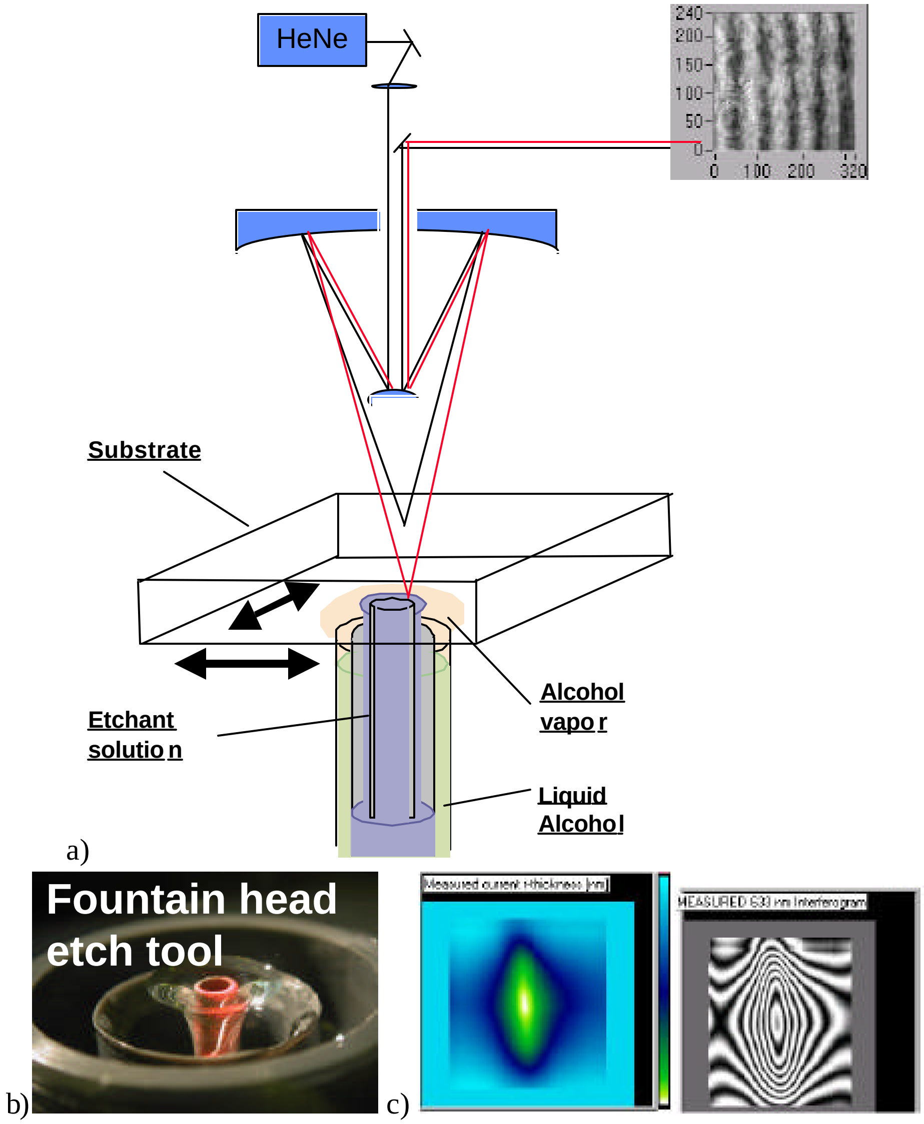

Fig. 2.1.3.4 a) Phase plate fabrication apparatus showing the etching tool, phase plate substrate, and active interferometry of the etched surface, b) Actual picture of one of the fountain head etch tools, c) Screen shots from the active interferometry of one of a phase plate for our system.

We tested the phase plate by measuring the far field focus of a beam passing through the amplifier and phase plate. The results for this experiment are shown in Fig. 2.1.3.5. For the single pass offline tests, the energy inside a five times diffraction limited spot increased from 90% to 94% by utilizing the phase plate, while the energy in a 1 times diffraction limited spot increases from 11% to 39.

System performance

A single shot gain curve was mapped out by steadily increasing the diode pump pulsewidth from 300 ms up to 1100 ms. The results are shown in Fig. 2.1.3.5. The theoretical fit shows good overlap with the experimental data.

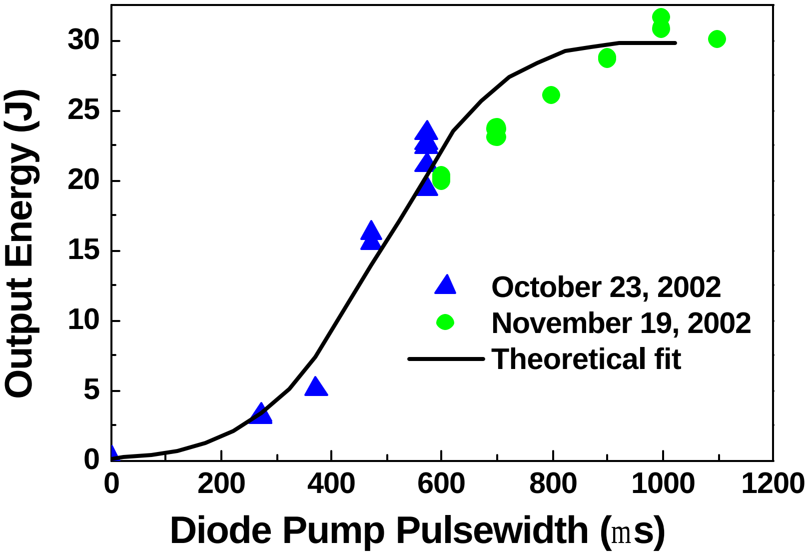

Fig. 2.1.3.5 Gain curve showing output energy as a function of diode pump pulsewidth

The next set of experiments involved increasing the repetition rate from 0.1 Hz to the 10 Hz . We initially observed a decrease in energy, but later found this to be due to the diode arrays tuning off wavelength. Calculations shown in Fig. 2.1.3.6 b) confirm the sensitivity to diode pump with more than a 50% drop in energy for only 2 nm shift in the peak wavelength.

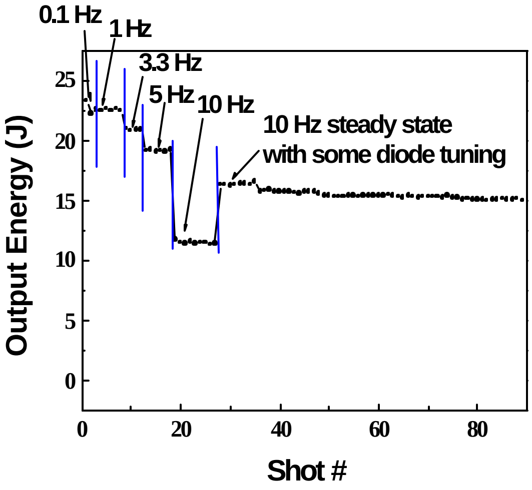

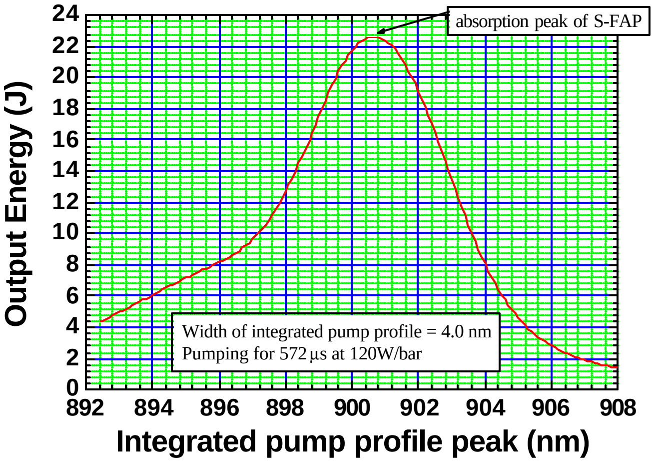

Fig. 2.1.3.6 a) Output energy versus repetition rate showing gain drop due to diode detuning, b) Sensitivity curve showing output energy versus the diode wavelength.

To achieve peak gain and output the diodes are carefully tuned during operation. By observing the diode light transmitted by the amplifier head one can tune the diodes such that the diode peak wavelength overlaps the absorption of the S-FAP crystals. With the diodes properly tuned, the system was operated with a diode pulsewidth of 600 μs for approximately 1.4 minutes at 5 Hz, producing over 20 J per shot or 100 W average power (Fig. 2.1.3.7). Dropouts have been left in the data to show separate runs where the system was brought down to check for damage.

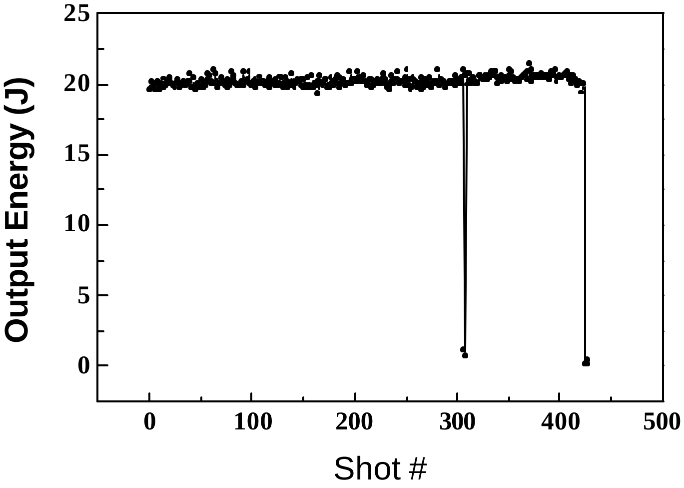

Fig. 2.1.3.7 Output energy shots for a 5 Hz run for a total time of approximately 1.4 minutes showing only a 1.4% rms energy fluctuation.

The near field intensity profiles are shown Fig. 2.1.3.8 before and after single-shot extraction. The 20 J profile shows a 10% rms intensity modulation. Fig. 2.1.3.9a shows the far field of the front end laser which has an M^2 ~ 2, with 98% of the energy in a five times diffraction limited spot, and 31% in a one times diffraction limited spot. With the addition of a static phase corrector (Fig. 2.1.3.9b), the static far field spot after 4 passes through the system has more that 83% enclosed in a five times diffraction limited beam and 15% in a one times diffraction limited beam. Upcoming measurements of the far field will include thermal distortions.

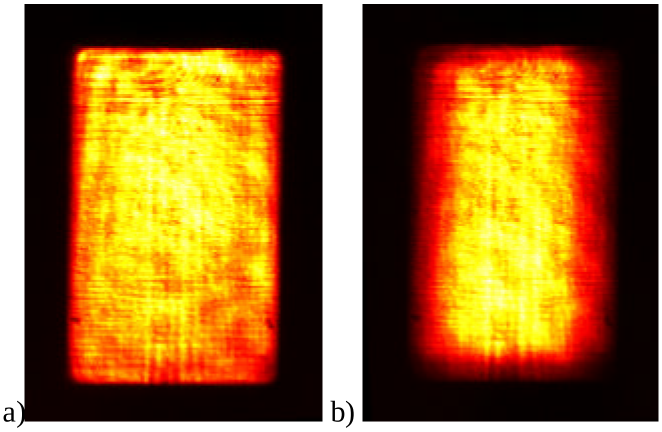

Fig. 2.1.3.8 a) Near field intensity profile after 4 passes with just the front-end running, b) Near field intensity profile at 20 J output energy showing imprint from diode pump profile.

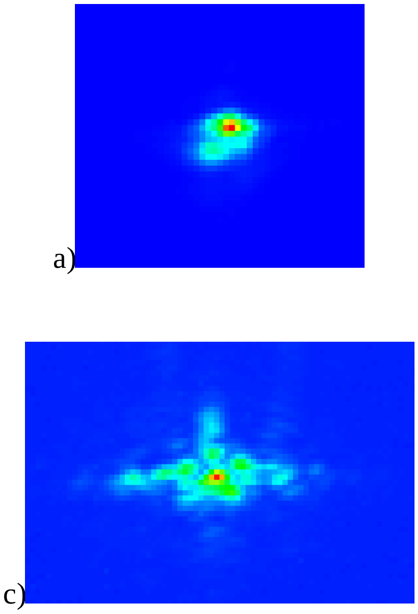

Fig. 2.1.3.9 a) Far field of the front-end laser, c) Static Far field after four passes with the phase plate

The laser was run at 10 Hz and up to 20 J was extracted from the amplifier (Fig. 2.2.3.10). The shot run showed only a 2.7% rms energy fluctuation, however on the last set of shots the laser damaged a small mirror in the reverser optics. Future runs are aimed at operating the system up to an hour.

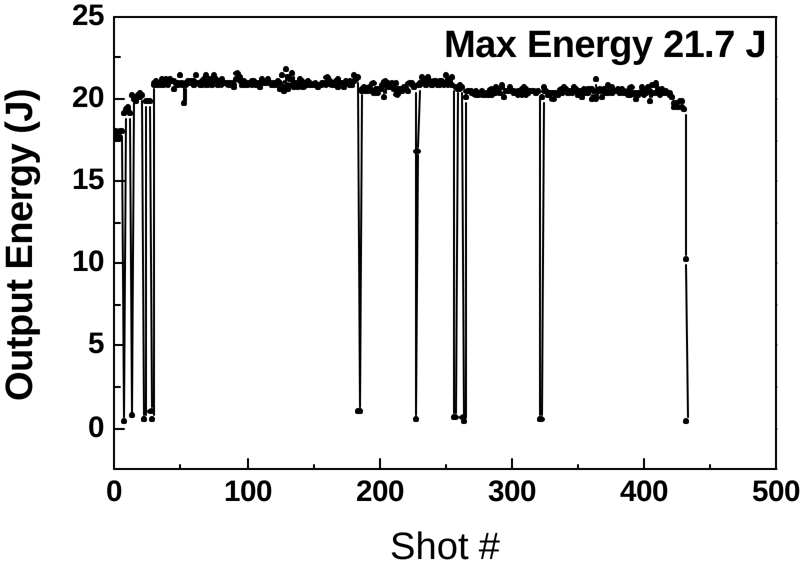

Fig. 2.2.3.10 Output energy shots for a 10 Hz run for a total time of approximately 40 seconds showing only a 2.7% rms energy fluctuation

2.1.4 Laser Diagnostics

Our FY2002 tasks were:

- Full integration of diagnostics packages with laser and control systems

The angularly multiplexed, four-pass architecture of Mercury allows the laser beam to be easily diagnosed on every pass without the use of fast optical switches since each of the passes can be spatially separated from one another. A total of four packages (input, pass1, pass2, pass4) were used in the system to monitor energy and beam quality during 10 Hz operation (Fig. 2.1.4.1).

Fig. 2.1.4.1 A view showing the small footprint of the vertically mounted diagnostic packages next to the Mercury laser beamline

A single diagnostic package (Fig. 2.1.4.2) contains cameras for laser alignment and beam quality measurements, an energy detector for gain, a photo detector for evaluating temporal reshaping of the pulse during extraction, and the dark field camera for real-time damage detection. All systems must be capable of 10 Hz operation. The data for each diagnostic is stored on a separate computer and archived for later retrieval.

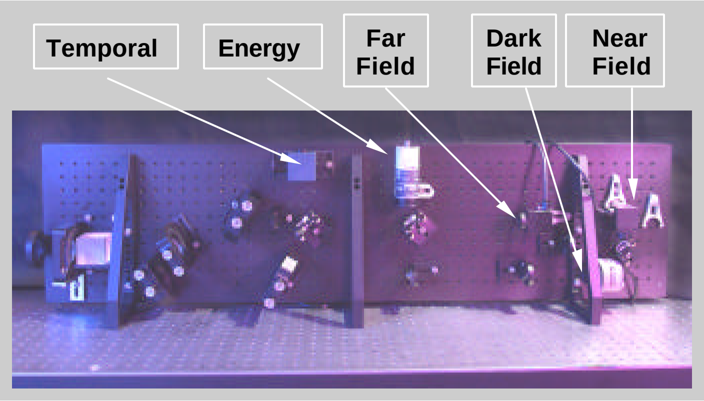

Fig. 2.1.4.2 Single diagnostics package

Damage detection

The damage diagnostic is a critical instrument in the initial activation stages since components such as diode arrays and crystalline slabs in the amplifier are of high value. The tracking of damage on a shot-to-shot basis is important for rep-rated systems where damage sites can grow quite rapidly and cause optics to crack. Of greatest concern is the prevention of damage to downstream optics from a damaged optic due to a highly modulated beam. Therefore, the damage diagnostic is directly interfaced to our control system so that diodes and the extraction beam can be quickly stopped if damage is detected.

The dark field image is taken by blocking the beam at the focus of a telescope and re-imaging the beam on a high resolution camera. The re-imaged beam has only high frequency spatial components and therefore allows small damage features to be more easily seen and analyzed by computer software as seen in Figure 2.1.4.3. The damage diagnostic presents a challenge since it must operate at high repetition rate, high resolution and processes the data on ever shot. A camera was identified (Q-Imaging inc., Model 1350) which satisfied these requirements including with megapixel resolution allowing detection of damage spots to 100 microns in size.

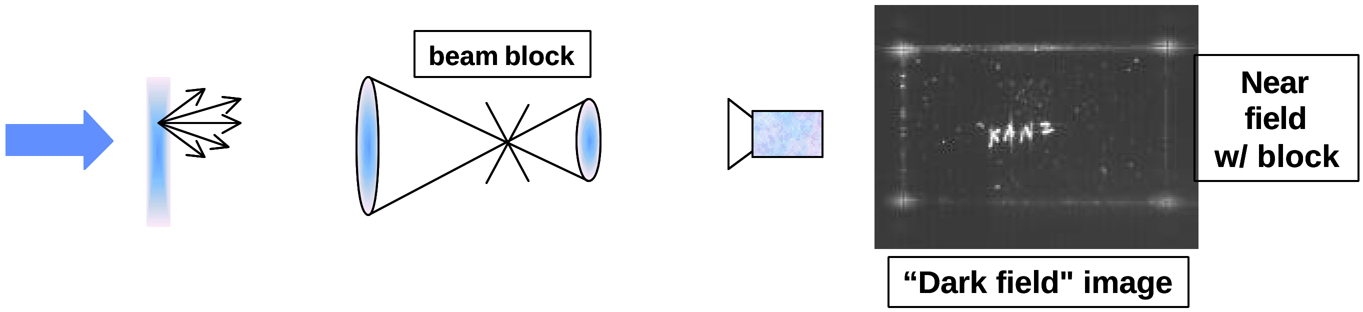

Fig. 2.1.4.3 Conceptual layout for taking a darkfield image and sample data.

We have developed a software algorithm to allow a computer to make a decision as to whether damage has occurred as illustrated in Fig. 2.1.4.4. The first shot of the day is recorded as a background image. An experimental run is then started and each shot is evaluated as follows: the shot is captured, then the background is subtracted, the residual is converted to a binary image with a user defined threshold, this binary image is analyzed and the system is either shut down or allowed to continue based on a user defined maximum damage size.

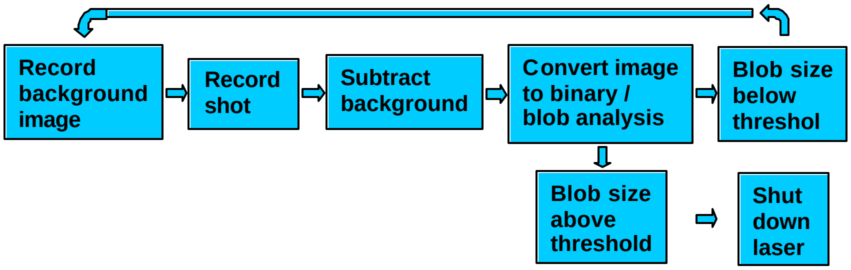

Fig. 2.1.4.4 Algorithm for detecting damage

The algorithm has been experimentally verified and utilized on the system for all average power measurements reported in the previous experimental section. An offline facility with a full scale optical layout of the beam was used to test the algorithm. Fig. 2.1.4.5 shows the images resulting from the algorithm processing.

where the shot is converted to a binary object analysis image that is then evaluated for damage. During the 10 Hz campaign runs the threshold object size had to be adjusted to decrease the sensitivity to thermal shot to shot intensity fluctuations. The dark field is set up to image relay the amplifier, and is primarily sensitive to edges. This means that sharp gradients in intensity will be clearest in the dark field, while low gradient changes will typically fall below threshold. As a companion diagnostic, a near field image can be used as a bright field damage diagnostic. In this case, drops in the intensity become indication of damage. The maximum sensitivity to damage occurs for optics out of relay since diffraction enlarges the occlusion to the near field image. An example of the onset of damage on an out of relay reverser mirror is shown on Fig. 2.1.4.6. The damage spot which is < 1 mm in diameter in actuality takes up nearly 1 cm of the beam due to diffraction. Thus the dark field and bright field work together to detect the onset of damage on optics near image relay versus those out of image relay.

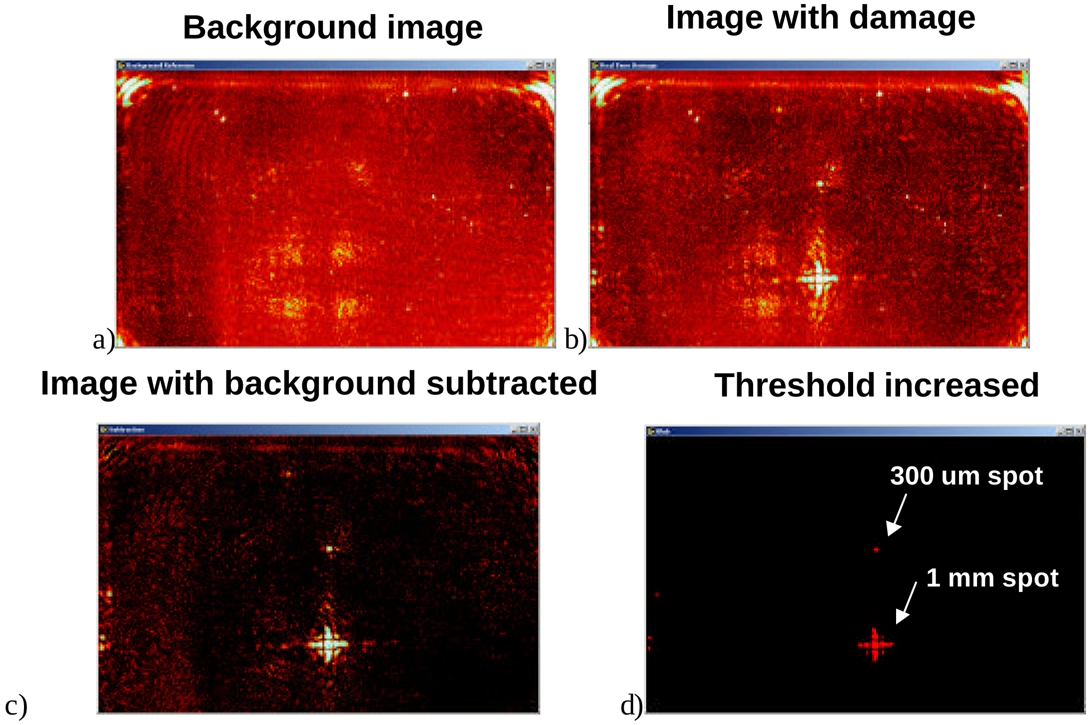

Fig. 2.1.4.5 a) Background image, b) image with damage, c) image with background subtracted, d) image converted to binary and thresholded to show darkfield sensitivity to various spot sizes

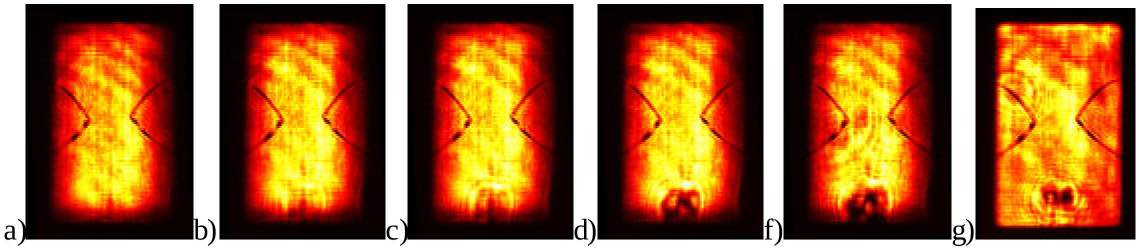

Fig. 2.1.4.6 Near field images of the output beam at 10 Hz showing the formation of damage at 10 Hz (a-f) and the static near field illuminated by only the front end (g). The v-shaped cutouts are due to a fracture in a prototype phase plate.

2.1.5 Average Power Pockels Cell

Our FY2002 tasks were:

- Build and test 3x5 cm^2 Pockels cell and high voltage driver and integrate into laser system.
- Produce conceptual design for a Kilowatt IRE aperture (10x15 cm^2) Pockels cell and driver

Introduction

We have completed the construction of the full-size (3.5 cm x 6 cm aperture) Pockels cell for the Mercury laser and examined the relative merits of two architectures for high average power (100 J, 10 Hz, 1 kW), large aperture (10 cm x 15 cm) Pockels cells.

A Pockels cell (also know as a Q-switch, electro-optic switch, or electro-optic modulator), is a device that can control the polarization state of light electrically. Using dual-crystal, thermally compensated, $LiNbO_3$ and $KTiOPO_4$ (KTP) electro-optic modulators, we have previously demonstrated 250 and 65 watts, respectively, of Q-switched average power at thermal loadings approaching 1 kW/cm2. [1-2] The low surface damage threshold of $LiNbO_3$ and the limited aperture of KTP pose a problem for devices operating at moderate fluences (3-5 J/cm^2) or requiring apertures greater than 2 cm^2. For the Mercury Laser application, KD_2PO_4 (DKDP) remains as the only commercially available electro-optic crystal available in large apertures with high optical homogeneity and with damage thresholds exceeding 10 J/cm2. However, the relatively low thermal conductivity, relatively high near-infrared optical absorption, and relatively low fracture strength makes DKDP difficult to use for high average power applications. [3]

A moderate aperture (3.5x6 cm^2) electro-optic cell which can handle 100 W of average power is required for use as an isolation device in the Mercury reverser path. Last year we built and tested a scaleable, near ½ aperture, dual DKDP crystal Pockels cell, which, in off-line testing, exhibited less than 0.5% depolarization when thermally loaded with a 100 W near-infrared laser. Based on the success of this design, we built and tested a full Mercury aperture (3.5 x 6 cm^2 aperture) Pockels cell, shown in Fig. 2.1.5.1 The full aperture Pockels cell exhibits a contrast ratio better than 200:1. This report also addresses the scaling of this device to a large aperture for the IRE (nominally 10 x 15 cm^2) that will also handle a 10-fold increase in average power (nominally 1 kW in the Pockels cell).

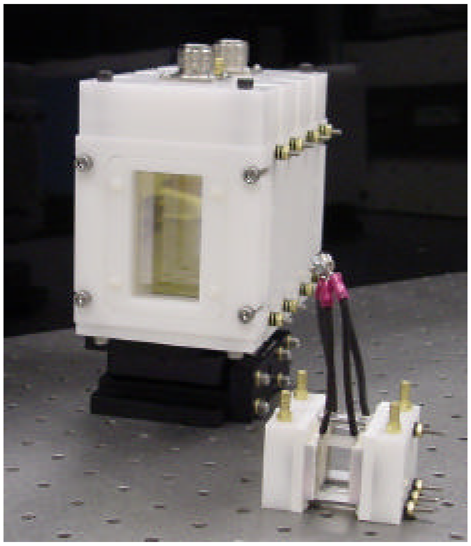

Fig. 2.1.5.1 The full aperture (3.5 x 6 cm^2) aperture Pockels cell adjacent to the small aperture demonstration cell.

Full aperture Pockels cell construction and testing

The construction and thermal characterization of the sub-aperture test Pockels cell has already been documented. [4] To summarize, under a thermal loading of over 100 W of average power, the Pockels cell demonstrated less than 0.5% depolarization. This represents the highest average power demonstrated utilizing a low aspect ratio, slab-aperture DKDP Pockels cell. Several issues were addressed during the construction and utilization of the sub-aperture cell, lessons that were subsequently applied to the larger aperture cell needed for Mercury. These issues included: (1) Design of the housing to minimize capacitance during switching (an issue affecting the speed at which the Pockels cell can be electrically switched), (2) Specification of the crystal fabrication requirements to allow accurate and consistent fabrication of matched crystal pairs, and (3) Specification of the Pockels cell assembly instructions to ensure that the highest contrast ratio is obtained during construction.

Fig. 2.1.5.2 shows the arrangement of a pair of DKDP crystals in a thermally compensated Q-switch. The DKDP crystals and a 90 degree quartz rotator are thermally bonded to an alumina substrate, which provides a sink for the modest amount of heat (~1-2 W) deposited in the crystal. The DKDP crystals we utilized were polished to a flatness of lambda/10 with parallelism better than 30”. In an ideal pair of identical length crystals, the static birefringence, thermally induced birefringence, and the stress-optic induced depolarization would vanish. When the ideal crystal arrangement of Fig. 2.2.6.2 is placed between parallel polarizers (with polarization axis at 45^o to the Z axis) no light would be transmitted across the aperture. If a 90^o rotator is placed after the compensated crystal pair, the maximum intensity is transmitted. For a non-ideal crystal pair, the fraction of light which is depolarized due to uncompensated birefringence is determined from the expression:

$$I_{\text{depolarization}} = I_{\text{rotator removed}} / (I_{\text{rotator removed}} + I_{\text{rotator inserted}})$$

Our test setup, shown in Fig. 2.1.5.3, utilizes a 1047 nm source. Static depolarization is examined utilizing both a high resolution camera as well as a photodiode. As constructed, the full aperture Pockels cell exhibits less than 0.2% static depolarization at 1047 nm and has an insertion loss of 0.8%. Finally we have completed testing of the high voltage (13.5 kV) electro-optic pulser required for electrical switching and have demonstrated optical switching at 1047 nm.

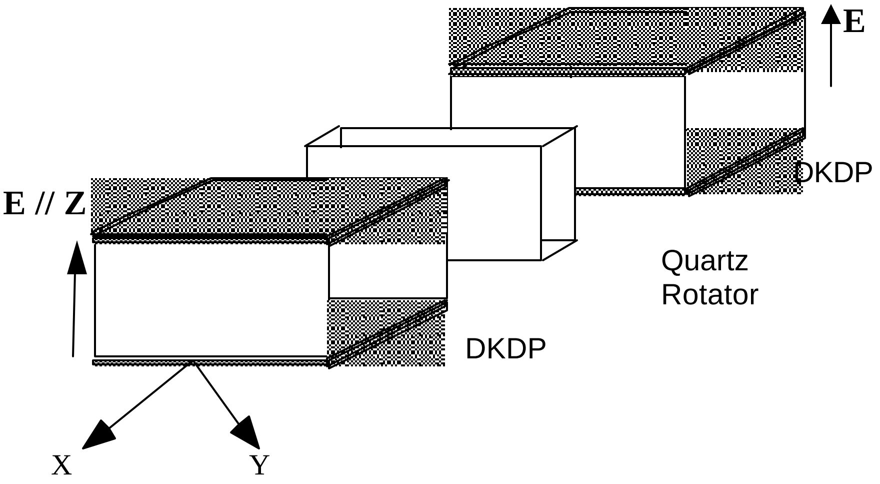

Fig. 2.1.5.2. Transverse, bicrystal, thermally compensated switch consisting of DKDP crystals and 90 degree quartz rotator.

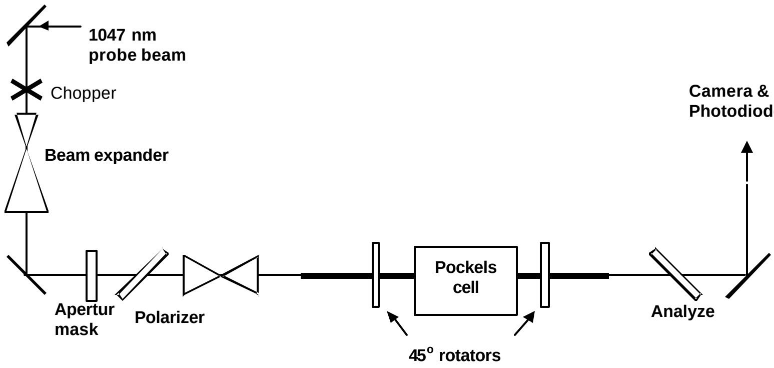

Fig. 2.1.5.3. Apparatus used to thermally load Pockels cell assembly and examine depolarization.

Wavefront was also measured for the Pockels cell assembly (3 rotators, 2 KDP crystals) and was found to contribute 0.15 waves.

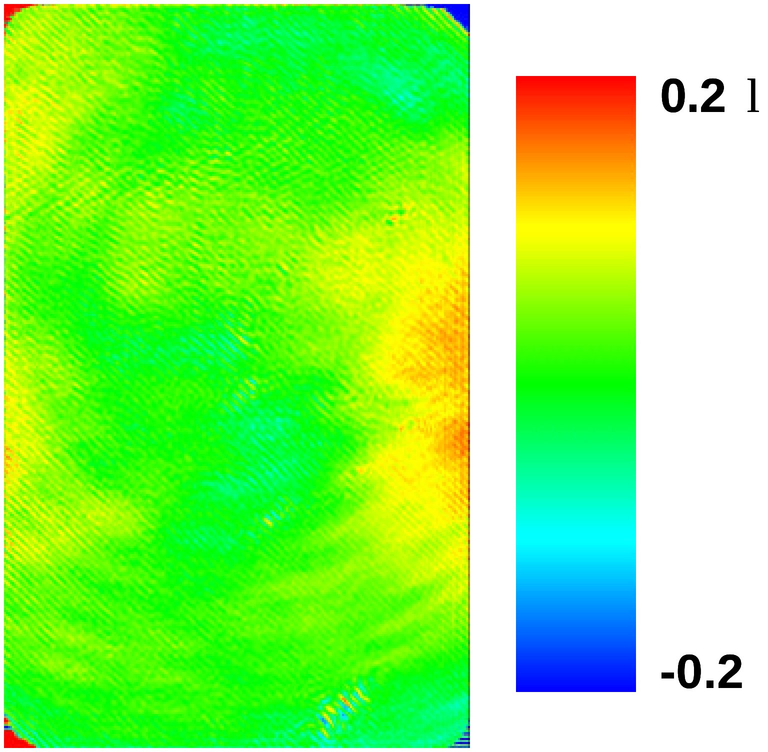

Fig. 2.1.5.4. Wavefront of the Pockels cell assembly.

Kilowatt IRE class Pockels cell designs

The current 3.5 x 6 cm^2 aperture Pockels cell is sufficient for Mercury laser. The Pockels cell itself experiences 100 W) of average power in the reverser, as only the energy from the first and second pass extraction traverses the path including the Pockels cell. Off-line testing and modeling suggests that the actual performance limit of this particular cell is 400 W. [4] The crystals will experience an average power of approximately 100 W distributed across the 15 cm^2 aperture and an energy fluence of approximately 0.6 J/cm^2. The 99% deuterated DKDP crystals have an estimated optical absorption on the order of 500 ppm/cm [5] leading to 1-2 Watt of absorbed power with a maximum thermal loading of 0.13 W/cm^2.

Two issues act to limit the average power capability of the cell: optical damage limitations and thermally induced depolarization. KDP and DKDP have moderate damage thresholds near 10 J/cm^2 for 3 ns pulses. The average power damage limit of the existing Pockels cell is 15 kW. Thus, optical damage is not expected to be a limiting issue for scaling to large aperture devices. Long before the peak power damage becomes an issue, average power (thermal loading) will induce stress-optic depolarization and lead, perhaps, to catastrophic cracking and failure of the crystals. The thermal average power limit of the Pockels cell is dependent upon the thermal fracture strength of the DKDP crystal. That is, stress induced by thermal expansion, caused by the temperature difference between the center and edges of the crystal (the crystal is only cooled through the upper and lower surfaces), will eventually lead to failure of the crystals. Simply scaling the DKDP crystals to a 10 x 15 cm^2 aperture (from the 3.5 x 6 cm^2) with constant thermal loading increases the thermal gradient across the aperture 4x, and at the same time reducing the maximum average power handling capability by ¼ or 100W. Therefore a different approach must be taken for designing the IRE Pocklels cell since it will experience an average power loading of 1000W.

Aanamorphic scaling of the transverse cooled – transverse electrode slab aperture design

One approach to increase the thermal power handling of the Pockels cell is to anamorphically change the aspect ratio of the laser footprint. That is, the laser beam must be reduced in the dimension parallel to the thermal gradient (i.e. the 10 cm x 15 cm aperture is reduced in one dimension to 3.5 x 15 cm^2). Reducing the aperture across which the Pockels cell is cooled by 2x increases the average power capability 4x. Scaling the current electro-optic switch requires an minimum anamorphic expansion of at least 3.2 (a 10x increase in thermal handling) – leading to a minimum beam aperture in of 3.2 x 15 cm^2. This is the minimum acceptable aperture for the Pockels cell, scaling from the proposed 400 W maximum average power limit for the 3.5 x 10 cm^2 cell. Including a margin of safety, the required aperture for the 1 kW device will probably be 2.5 x 15 cm^2 – corresponding to a 4:1 anamorphic reduction of the 10 x 15 cm^2 aperture of the IRE. The switching voltage of the Pockels cell remains similar to the current design (13.5 kV), as the relative ratio of the electrode thickness to the propagation thickness remains the same as in the current cell.

To ensure a high contrast ratio, all crystal pairs utilized in these large aperture Pockels cells must be identical thickness (to within a few microns). By careful control of the fabrication process, the availability and machining and polishing of large aperture DKDP crystals to these tolerances is not thought to be an issue. However, the requirement of an optical rotator, currently made of crystalline quartz, poses significant limitations on the final aperture. Quartz is available in the required 3.5 x 6 cm^2 aperture (thickness of approximately 13.8 mm). Scaling to the 15 cm aperture is probably beyond the available aperture of hydrothermally grown quartz. Two possible risk reduction approaches have been examined. The first is to take smaller aperture quartz pieces and optically bond the smaller aperture crystals to form a large aperture crystal (our baseline strategy). A second approach is to grow optical rotator crystals that can be solution or melt-grown to the desired aperture. (Quartz is grown by the hydrothermal growth method (hot water at high pressures), a process that does not scale easily in volume). One potential candidate for the latter option is an optical rotator crystal such as potassium dithionate, $K_2S_2O_6$, which can be either melt grown or solution grown to the desired aperture.

Transverse electrode, gas cooled face, multiple crystal plate design

A second high average power Pockels cell architecture, utilizing full aperture crystals (10 cm x 15 cm) has also been examined. This would be a transverse electrode, face-cooled, gas-cooled Pockels cell, consisting of a series of DKDP plates with cooling gas passing over the 10 cm x 15 cm^2 aperture. In this type of Pockels cell, the thermal gradient is now in the direction of the beam propagation, and the thermal limit derives from the thickness of the individual plates that comprise the overall cell. With the proposed thermal loading, the plates must be less than 2.5 cm thick. In this design, the switching voltage is kept a constant only if the electrode distance (10 cm) relative to the propagation thickness remains constant.[3] The plate thickness and number of plates is directly related to the switching voltage, i.e. if the electrodes are placed on the 10 cm aperture, a 1 cm propagation thickness will lead to a switching voltage of 134 kV whereas a 10 cm propagation thickness will lead to a switching voltage current switching voltage of 13.4 kV. Constructing plates 10 cm x 15 cm in aperture, with a thickness of 2.5 cm will again allow thermal scaling of the Pockels cell to the kilowatt average power limit. If a total of 6 DKDP plates with 10 cm x 15 cm aperture and 1.6 cm thickness are used, the device will still switch with a voltage near 13.4 kV.

Summary

We have completed the construction and testing of a large aperture Pockels cell (3.5 cm x 6 cm^2 aperture) suitable for use in the Mercury laser. We have also proposed two designs suitable for scaling to the IRE kilowatt average power design. The first design utilizes anamorphic compression of the beam while the second Pockels cell design requires multiple thin plates whose faces are cooled by flowing gas. Both designs would benefit from large aperture rotator materials, generated either by optical bonding of smaller aperture quartz plates, or growth of a new optical rotator crystal.

References

[1] S. P. Velsko et. al. “100 W Average Power at 0.53 um by external frequency conversion of an electro-optically Q-switched diode-pumped power oscillator”, Applied Phys. Lett. 64 pp. 3086-3088 (1994).

[2] C.A. Ebbers, S.P. Velsko, “High average power KTP Electro-optic Q-switch”, Applied Phys. Lett. 67 pp. 593-595 (1995).

[3] D. Eimerl, “Thermal aspects of high-average-power electro-optic switches”, IEEE J. Quantum Electronics 23 pp. 2238-2251 (1987).

[4] H. Nakano, K. Kanz, C. Ebbers, ‘A thermally compensated deuterated KDP Q-switch for high average power, large aperture lasers”, Conference on Lasers and Electro-Optics, Anaheim, CA (May 2002).

[5] C.A. Ebbers, J. Happe, N. Nielsen, S.P. Velsko, “Optical absorption at 1.06 microns in highly deuterated potassium dihydrogen phosphate”, Applied Optics, 31 (1992).

2.1.6 Czochralski Crystal Growth

Our FY2002 tasks were:

- Place contract with Northrup Grumman to produce at least one high optical quality crystal.
- Dedicate two furnaces to produce crystals for slab fabrication and a third for testing growth parameters.
- Fabricate and install 7 crystalline slabs into amplifier.
- Investigate techniques to grow up to 5 cm sized boules with Czochralski and the Heat Exchanger Method.

Introduction

The goals of the crystal growth effort are to produce high quality Yb:S-FAP [Yb^{3+}:$Sr_5(PO_4)_3F$] crystalline slabs; The Mercury design requires a total of 14 crystalline slabs of dimension 4 x 6 x 0.75 cm (Fig. 2.1.6.1) which will be potted into vanes and mounted into two amplifier heads. Each head holds seven slabs. Currently, high quality crystalline boules are being produced that can be fabricated into crystalline slabs for the Mercury Laser. However, the growth of high optical quality boules has been a challenge due to a number of defects, including: cloudiness, bubble core defects, grain boundaries, anomalous absorption, cracking, and inclusions near the surface of the boule.

Significant progress has been made in understanding the growth characteristics and defect chemistry of Yb:S-FAP crystals. At this time, crystal growth parameters are understood well enough at LLNL to produce crystals from which half slabs can be harvested and diffusion bonded to form full size slabs. As part of the effort to understand the defect issues in Yb:S-FAP and determine a feasible growth technique for producing high optical quality crystals we have formed a collaboration with experts in industry and research institutions including Dr. Robert C. Morris (formerly of Allied Corporation and a world-renowned leader in solving defect problems in optical crystals), Northrop-Grumman Poly-Scientific (formerly Litton-Airtron/Synoptics Group) and Crystal Systems, Inc.. Our work with Northrop is primarily directed towards developing a commercial source for Yb:S-FAP. Northrop has the expertise and facilities in place for growing large diameter crystals such as 6 inch GGG. As an alternative to this technique, we are working with Crystal Systems, Inc. to assess the feasibility in growing Yb:S-FAP by the Heat Exchanger Method, which has successfully been used for the growth of >15 inch crystals such as sapphire, Ti:sapphire, silicon, and YAG.

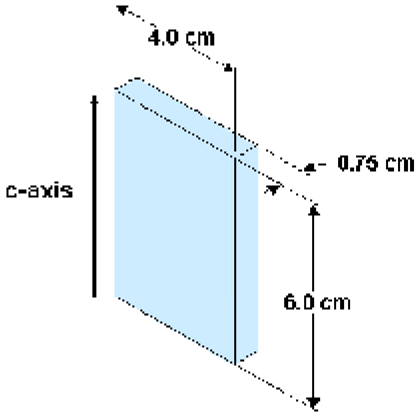

Fig. 2.1.6.1 Schematic of the slab dimensions required for the Mercury design

Growth Methodology and Process

Crystals of Yb:S-FAP are grown by using the Czochralski method in three growth stations one of which is shown in Fig. 2.1.6.2a along with a schematic of the furnace design and basic growth parameters, Fig. 2.1.6.2b. The growth station consists of a Czochralski crystal puller, a 25 kWatt induction power supply, and a computer program that is used for automatic diameter control of the crystal. Automatic diameter control is achieved by weighing the crystal as it is growing and calculating the mass gain per unit time (grams/hour or g/h). It is utilized so that the diameter of the crystal is constant at a given pull rate. In order to carefully regulate the growth process, chillers have been added to control cooling water temperatures to the power supplies and regulate the heat load and a motor generator was installed to dampen signal fluctuations to the power supplies. Most recently three power supplies were purchased to increase the power stability and reliability during crystal growth and will be installed next year. A 4” diameter by 4” tall iridium crucible was chosen to contain the melt because it does not chemically react with Yb:S-FAP and has a high melting temperature. Zirconia is the main insulation component in the furnace as shown in Fig. 2.1.6.2b. The 4” diameter by 4” tall iridium crucible and melt therein is heated by inductive coupling of the crucible and copper induction coil.

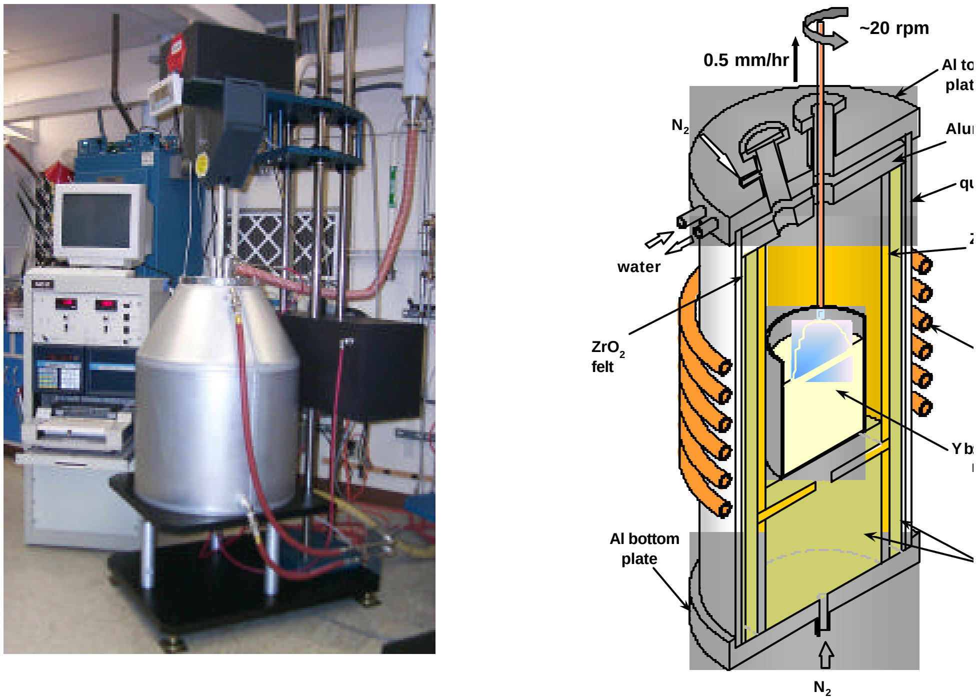

Fig. 2.1.6.2 (a) Picture of the Czochralski crystal growth station used for Yb:S-FAP growth. (b) Schematic of the furnace design with approximate growth parameters.

The time required to grow Yb:S-FAP crystalline boules of suitable size to harvest slabs is approximately 17 days and encompasses four steps that are critical to producing high quality material, Fig. 2.1.6.3. The first step requires that the initial part of the growth be kept at a very small diameter in order to force grain boundary defects to grow towards the sides of the crystal where they will terminate. The cone section of the boule is the next critical step since the overall growth rates tend to be much higher than in other parts of the growth process and defects can form. For this reason the cone angle is kept very small so that during the growth process the boule size is slowly increased until it reaches the full diameter. In the cylinder section of the boule, where the diameter is kept constant, it is essential that stable growth conditions be maintained since this is the region from which the slabs will be cut. Finally, the crystal is tapered in at the bottom and allowed to cool while attached to the melt. This helps decrease the thermal gradients through the boule during cooling and reduce cracking. A pull rate of 0.5 mm/hr is currently used since higher rates have shown an increase in the magnitude of the defects. The rotation rate is typically 15 rpm to provide a convex melt-interface shape that is stable and does not introduce unwanted fluctuations that can perturb the growth. This specific growth technique has significantly reduced the number of defects.

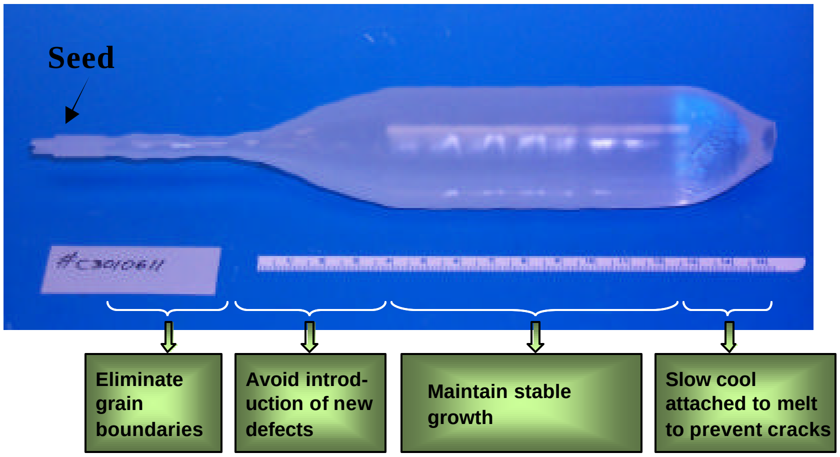

Fig. 2.1.6.3 Current technique for the growth of Yb:S-FAP crystals.

Defect Issues

Defect structures in Yb:S-FAP crystals can occur in various forms. We have observed: cloudiness, anomalous absorption, bubble core defects, grain boundaries, cracking, and inclusions around the outside of the boule. Each of these defect structures has been studied in considerable detail and solutions to reduce and /or eliminate them have been implemented as outlined below in Table 2.1.6.1. [1] Remaining concerns include bubbles down the center of the boule, cloudiness and cracking in a limited number of crystals during fabrication from internal stresses.

One method to reduce the magnitude of the bubble core or concentrate it to the center of the Yb:S-FAP crystal, is to stabilize the interface between the crystal and melt and decrease the amount of unwanted chemical constituents near the growth boundary layer. This has been accomplished by increasing the thermal gradients in the furnace above and within the growth crucible. By doing this, the temperature drives the convective melt mixing at the interface and reduces the thickness of the boundary layer of unwanted components that can cause unstable interface conditions. This approach has allowed us to grow 3.5 cm diameter boules, where the smaller diameter allows for better interface control and two half slabs can be cut from the outside of a crystal and bonded together as shown in Fig. 2.1.6.4.

With a growth process in place that minimizes the defects and allows slabs to be fabricated by bonding two half-sized slabs together, we dedicated two of the three available furnaces to slab production for the Mercury laser. The third furnace was used to address the remaining defect issues to further minimize and understand them. In this furnace, we changed the furnace design to more easily alter thermal profiles and growth atmosphere. Experiments to date have helped us to understand the effects of thermal gradient on the anomalous absorption (Table 2.1.6.1). Our next set of experiments will focus on scaling the diameter from 3.5 cm to greater than 5 cm.

In the two furnaces dedicated to slab production, we implemented the resolutions to the defect issues listed in Table 2.1.6.1 and have been able to produce material for the fabrication of five full size 4 x 6 cm slabs for the Mercury laser, see Fig. 2.1.6.5. In a parallel effort to LLNL, we continued a contract with Northrop for growth of 3.5 cm diameter crystals to try and double the production level. However the work had limited success due to a large bubble core and cracking. We therefore refocused the contract to growing 65 cm diameter boules to determine if the Northrop furnaces were better suited to growing larger diameter crystals.

Table 2.1.6.1 Summary of defect issues and the solutions.

Issue	Fundamental Cause	Resolution
Cloudiness	Precipitation on line defects	• excess SrF_2 in melt • annealing over melt
Anomalous absorption	Yb^{3+} in a different site	• c-axis along growth direction • axial thermal gradients <60°C/cm
Grain boundaries	Dislocations from the seed or growth instabilities	• seed extensions to grow out boundaries
Bubble core	Constitutional supercooling	• growth stability • maximize thermal gradients
Cracking	Internal stresses	• cool crystals attached to melt • reduce defects
Second phase inclusions	Limited Yb solubility in melt	• Yb-doping of <0.75 At.% in melt • increase thermal gradients

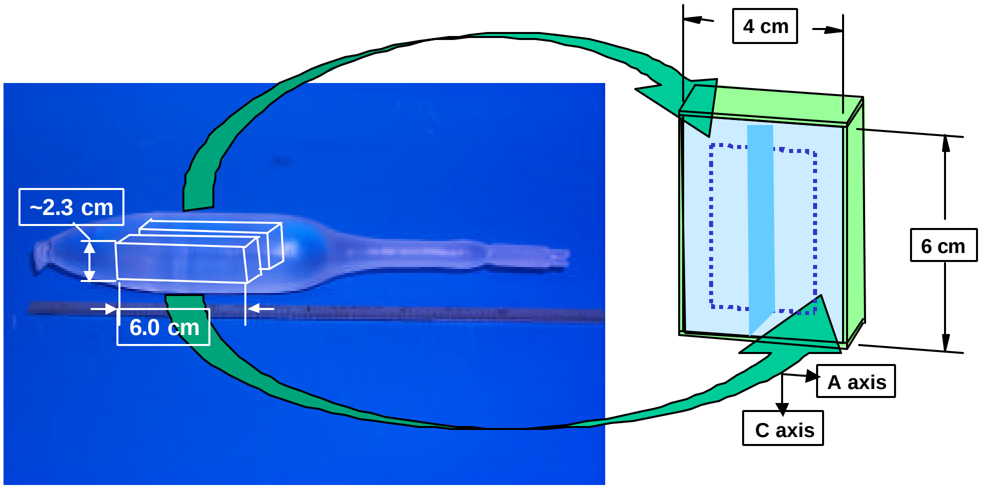

Fig. 2.1.6.4 Picture of the current growth geometry of a Yb:S-FAP boule and the orientation of slabs for diffusion bonding.

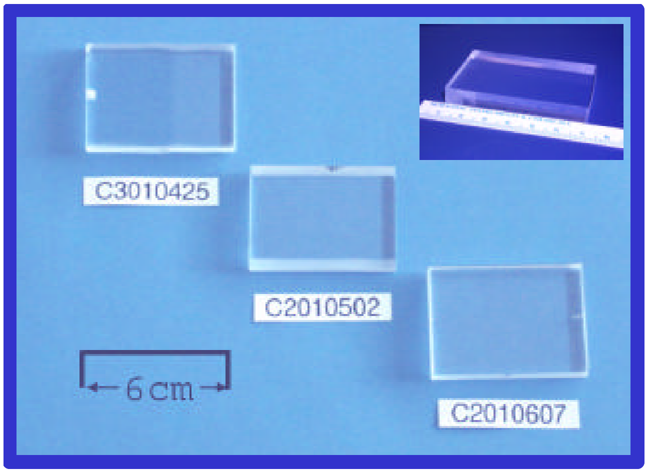

Fig. 2.1.6.5 Picture of the five bonded full size slabs.

Slab Fabrication

Once the crystal is grown there are several fabrication steps required to create a full sized slab. The crystals are first cut and polished for inspection of defects and suitability for slabs. The crystals are then cut into two parts around the central refractive index core by using a water jet cutting method described below. The two half sections are shaped into half-sized slabs for the bonding process which is the final step. Each of these steps and the progress to date are outlined in Fig. 2.1.6.6 and Fig. 2.1.6.7, respectively.

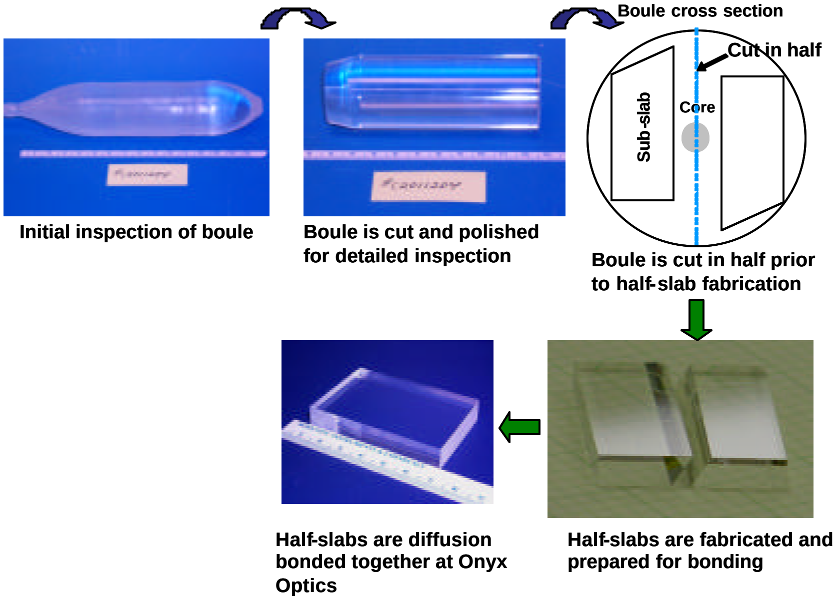

Initial inspection of boule

Boule is cut and polished for detailed inspection

Boule is cut in half prior to half-slab fabrication

Half-slabs are diffusion bonded together at Onyx Optics

Half-slabs are fabricated and prepared for bonding

Fig. 2.1.6.6 Crystal fabrication steps for the production of a bonded slab from a Yb:S-FAP boule.

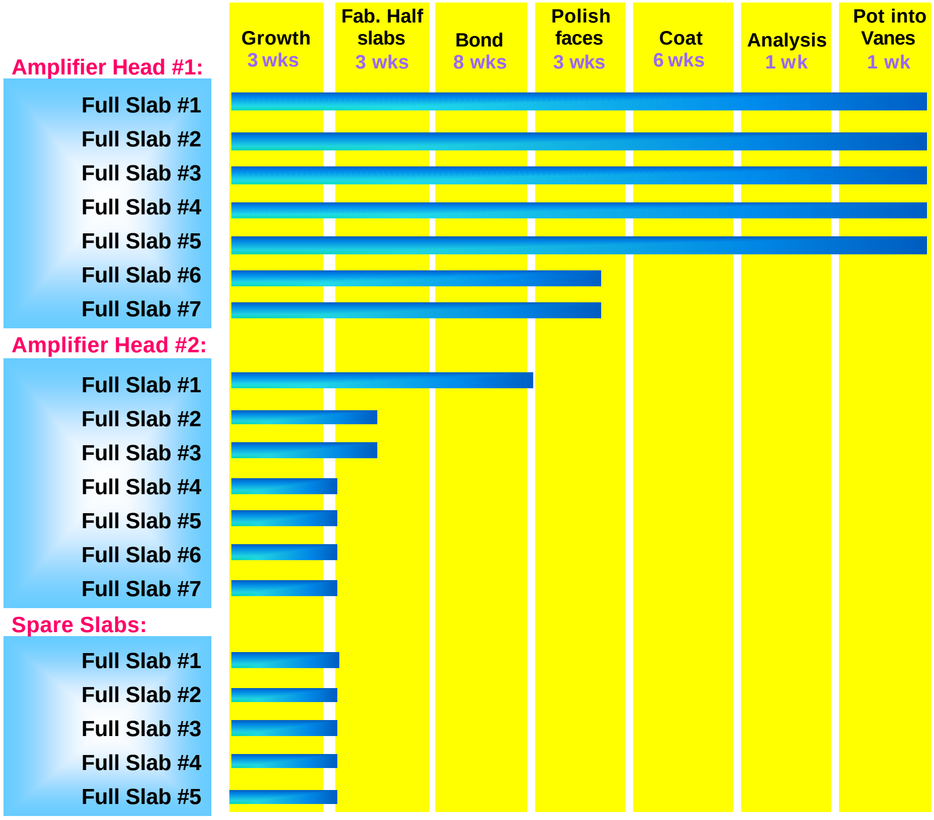

Fig. 2.1.6.7 Accounting of the progress made in fabricating the crystalline slabs for Mercury. We expect 30-60% of the boules to be successfully potted in the amplifier vanes

We have contracted Central Coast Gem Labs to cut the Yb:S-FAP crystals with a unique water jet cutting method to alleviate cracking during slab fabrication process. This company developed the water jet cutting technique for cutting soft fluoride-type crystals; it utilizes a specially designed nozzle that emits a very fine, high pressure, stream of water useful for cutting crystals without causing any localized heating that could promote cracking. By employing modeling of the stress in the crystals, which is discussed in the next section we been 100% successful in cutting the boules.

We have been working closely with a company (Onyx Optics, Inc., Dublin, CA) to bond the half-size slabs of Yb:S-FAP crystals together as shown in Fig. 2.1.6.4. [2] In FY02, we collaborated with Onyx to improve their polishing process. Scratches and particulates have inhibited the ability to bond Yb:S-FAP without incurring large phase distortions near the bond line. At this time we are trying heat treatments, better crystallographic orientation between the slabs, and more gentle polishing techniques. The last two slabs out of seven to completely fill the amplifier head, are in fabrication and will be finished late in the calendar year. Difficulties with polishing the bonded interface at Onyx Optics lead to cracking during the finishing stages and the slabs had to be cut apart and the process restarted a total of three times, thus severely impacting the delivery schedule.

Stress Analysis

While Yb:S-FAP crystals were initially plagued by a number of growth related defects, these have been brought under control and new difficulties have arisen during the fabrication. Due to internal stresses, 75% of the crystals would crack during different stages of the fabrication process (cutting, polishing and bonding). From previous experience we surmised that the high thermal gradients, (that reduce the crystalline defects) were creating residual internal stresses during the cool down process.

To help solve this problem, we engaged a group at University of California, Davis whose expertise in is measuring and modeling stress in materials. The internal stress field in an S-FAP boule was measured using the slitting method, which assumed the stress state was axially symmetric about the c-axis [3]. The magnitude of the axial stress in the boule was found to be as high as 50 MPa at the center of the boule and the general shape of the stress field was parabolic (Fig. 2.1.6.8a). Stress redistribution occurring during various cutting planes was then modeled using elastic finite element analysis. An optimum geometry and procedure for cutting was established by minimizing stress at the cut tip that would drive cracking. This cutting path is off the central axis of the crystal, avoiding the area where stress is greatest (Fig. 2.1.6.8b). Since the point at which fracture typically occurs in these crystals was found to be when the stress exceeded 27-35 MPa, we have employed a water jet cutting technique developed by Central Coast Gem Labs to minimize fracture and boule cutting stress (by minimizing heating). However, cracking during slab shaping and bonding continues to present a problem in many of the crystals. For this problem we are looking to post annealing of the crystals.

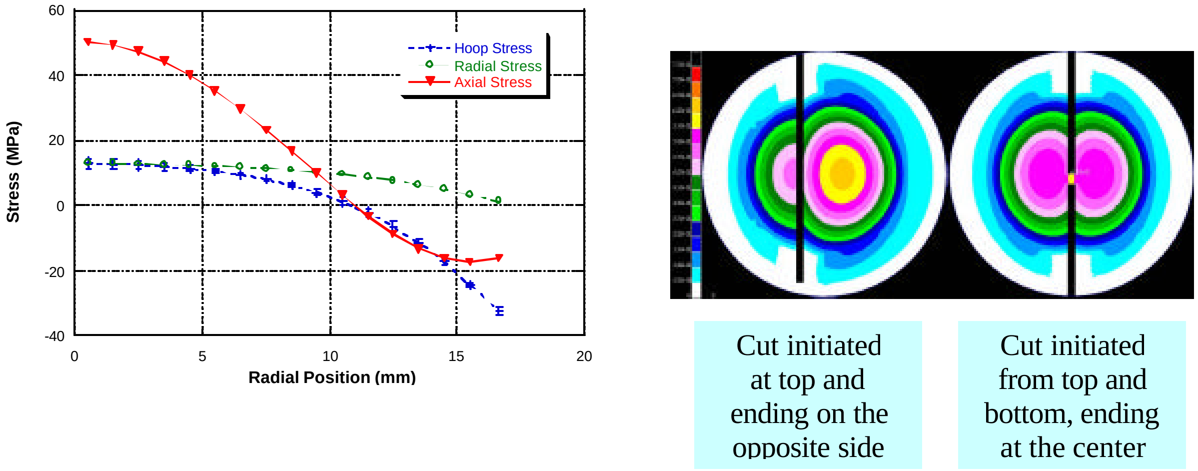

(a) (b) (c)

Fig. 2.1.6.8 a) Plot of the measured hoop, radial, and axial stresses for a boule and b) a diagram showing the preferred cutting geometry for the boules illustrated by maximum stress achieved as well as c) a diagram showing the stress when cut through the center of the crystal.

The annealing is done in a separate isothermal furnace. After the crystal is removed from the growth furnace and packed into crushed old remnant melt material from prior growths to maintain a "growth-type" atmosphere, it is heated to an approximate temperature of 1400-1500 C for 6-24 hours. The crystal is then cooled in an isothermal environment, which prevents any introduction of new stress into the crystal. We have found that annealing can also remove cloudiness in the crystals. It is possible that the second phase precipitate that caused the cloudiness can be re-dissolved into the lattice of the crystal during annealing. Therefore, post-growth annealing is a way to alleviate stress as well as reducing the cloudiness in the crystals to make previously unusable material useful. These experiments will continue and will become more important as crystal size increases and furnace gradients change.

Finally, we are working with a group at LLNL to use ultra-sound as a non-destructive method for measuring stress in crystals. This method looks at the differences in the speed of sound traveling through a material which will vary from a stressed region to a non-stressed region because of material lattice changes. In this way, stress can be mapped out in a crystal and one crystal can be compared to another without destroying the crystals. Also, this is a good method for determining if stress has been relieved in annealed samples.

Advanced Growth Efforts

A two-fold approach was taken to look at conventional large diameter Czochralski crystal growth techniques as well as a less conventional technique called the Heat Exchanger Method. We began working with Northrop to shift the original contract emphasis from small diameter growth to large diameter growth employing the Czochralski method. Northrop was able to grow two 6.5 cm diameter boules. We are very encouraged with these first growths in that the 2.7 cm central bubble core appears to be small enough to still harvest slabs (Fig. 2.1.6.9). In addition, there were a limited number of low angle grain boundaries and cracking of the boule near the bottom. Northrop is experimenting with the cool down process in hopes of reducing the internal stresses. In addition, future experiments will require fine-tuning the furnace design and growth parameters to better accommodate the growth of larger diameter crystals. We are working to develop a reproducible growth method that will control the defects and minimize fracturing from thermally induced stress, making it possible to fabricate large parts for various laser geometries.

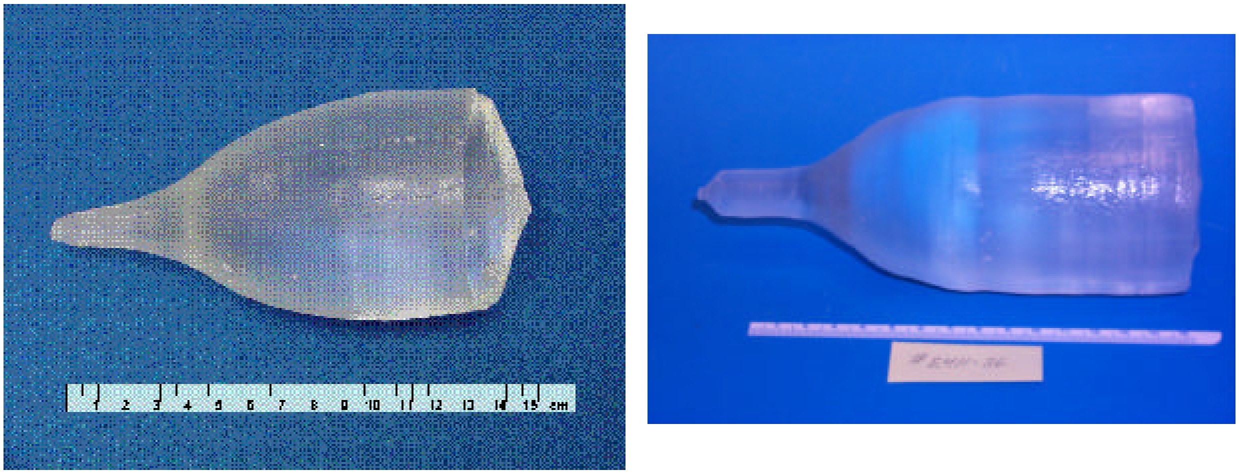

Fig. 2.1.6.9 Picture of two 6.5 cm diameter Yb:S-FAP crystals grown at Northrop Grumman.

In a continuing effort to explore the feasibility for growing Yb:S-FAP crystals by the Heat Exchanger Method, we placed a second contract with Crystal Systems, Inc. In this method, crystals are grown from a seed of Yb:S-FAP placed at the bottom of a crucible under the melt. The growth is controlled by cooling the seed and slowly lowering the seed and furnace temperature to maintain a stable interface while the crystal is grown from the bottom of the crucible to the top. A picture of the furnace design is shown in Fig. 2.1.6.10. Growths done during the contract produced approximate 2 cm square by 1 cm thick single crystals. The crystals were brownish in color, which has been attributed to color centers. However, recent annealing experiments done by packing the crystals in the crumbled melt left from a Czochralski crystal growth and annealing at 1450°C for 2 days have shown that the brownish color disappears and clear crystals can be produced see Fig. 2.1.6.11. In the last two contracts, a total of 17 growth runs have been completed. A final assessment of these runs has indicated that the composition of the crucible may still need to be determined as the brownish coloring could partially result from the Mo crucible. In addition, the exact composition of the melt material necessary for producing high optical quality crystals is still a question. Since this method is quite different from Czochralski growth, a direct correlation cannot be made and a composition must be discovered that does not create the defects seen to date. In the final part of the second contract, we will attempt to design experiments that address the crucible and melt composition issues.

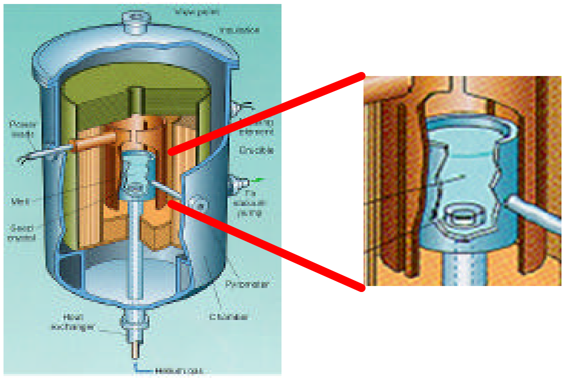

Fig. 2.1.6.10 Schematic of the furnace used in the Heat Exchanger Method at Crystal Systems, Inc.

Fig. 2.1.6.11 Picture of a Yb:S-FAP crystal grown by the Heat Exchanger Method, before and after annealing.

Summary

In summary, significant progress has been made in understanding and controlling each of the defect structures in an effort to develop a reproducible growth process for high optical quality Yb:S-FAP crystals. To date, 25 boules have been grown of which 16 have produced usable material. Five slabs were fabricated and installed in the laser and 3 more are being fabricated. Our efforts to reduce defects have allowed us to produce optical material that meets the Mercury specifications. In addition, a significant modeling effort was initiated to better understand and control stress cracking in crystals during fabrication to increase the yield for slab fabrication.

References

[1] K. I. Schaffers, J. B. Tasano, A. J. Bayramian, and R. C. Morris, "Review of the Growth of Yb:S-FAP [Yb^{3+}:$Sr_5(PO_4)_3F$] Crystals for the Mercury Laser," to be published in J. Crystal Growth.
[2]Diffusion bonding is done at Onyx Optics, Inc. in Dublin, California. Patent Number 5,441,803, H. E. Meissner, Onyx Optics, "Composites made from single crystal substrates, August 15, 1995.
[3] Cheng, Finnie and Vardar, 1992, Journal of Engineering Materials and Technology v114, p. 137.

2.1.7 Laser Diodes

Our FY2002 tasks were:

- Purchase 4000 diode bars and produce 150 V-BASIS tiles.

900 nm Diode Bars

An additional 4,000 diode bars were ordered in order to fabricate four new diode arrays or "backplanes" required to pump a second amplifier. Coherent Inc. supplied the diode bars to the specifications listed in Table 2.1.7.1.

Requirement	**Status**
10 nm FWHM at 750 us pulse	< 5 nm FWHM demonstrated
100 W peak output power per bar	Bars burned in at 115 W per bar
10% droop over pulse	5% droop demonstrated on 1 msec pulse
50% wall plug efficient	44% wall plug efficiency demonstrated
10:1 polarization (TE)	>10:1 TE to TM polarization discrimination
10^8 shot lifetime	1.4×10^8 shots

Table 2.1.7.1 Diode bar requirements and status

All of the specifications shown above have been successfully demonstrated, with the exception of the 50% wall plug efficiency. Although we elected to freeze the diode design since all the other specifications were met, we are confident that the internal looses could be further reduced with improved semiconductor growth procedures to achieve >50% efficiency. Of particular importance to the Mercury Laser design is that the entire collection laser diode bars have a very narrow wavelength distribution. This allows the diode light to efficiently overlap with the 900 nm Yb:S-FAP absorption linewidth. Fig. 2.1.7.1 shows a histogram of the wavelength distribution for 319 V-BASIS packages, corresponding to 7,337 laser diode bars. Binning the tiles by wavelength has allowed us to more accurately meet the wavelength specification by separately temperature tuning the wavelength of each of the eight diode backplanes.

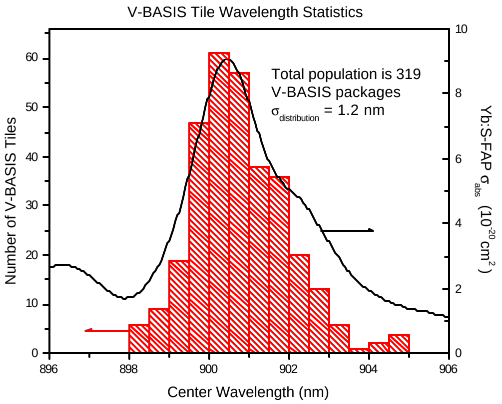

Fig. 2.1.7.1 Wavelength histogram and 900 nm Yb:S-FAP absorption feature

Diode Heatsinks

The diode bars are mounted onto a heatsink to remove the heat during operation. Since the operating requirements of 10 Hz and 1 ms only require a 1% duty factor, the heatsink design is significantly simplified in that all of the electrical connections and cooling manifolds are placed on a separate piece of hardware called the backplane, discussed in the next section. The laser diode package, which we call V-BASIS, is produced at LLNL and allows the diode bars to be packed with a pitch of 1 diode bar per millimeter. This year we have completed 150 packages. The packaging requires several fabrication steps as shown in Fig. 2.1.7.2 (a). A finished V-BASIS tile is shown in Fig. 2.1.7.2 (b). Each "tile" is 1 cm x 4 cm and holds 23 diode bars.

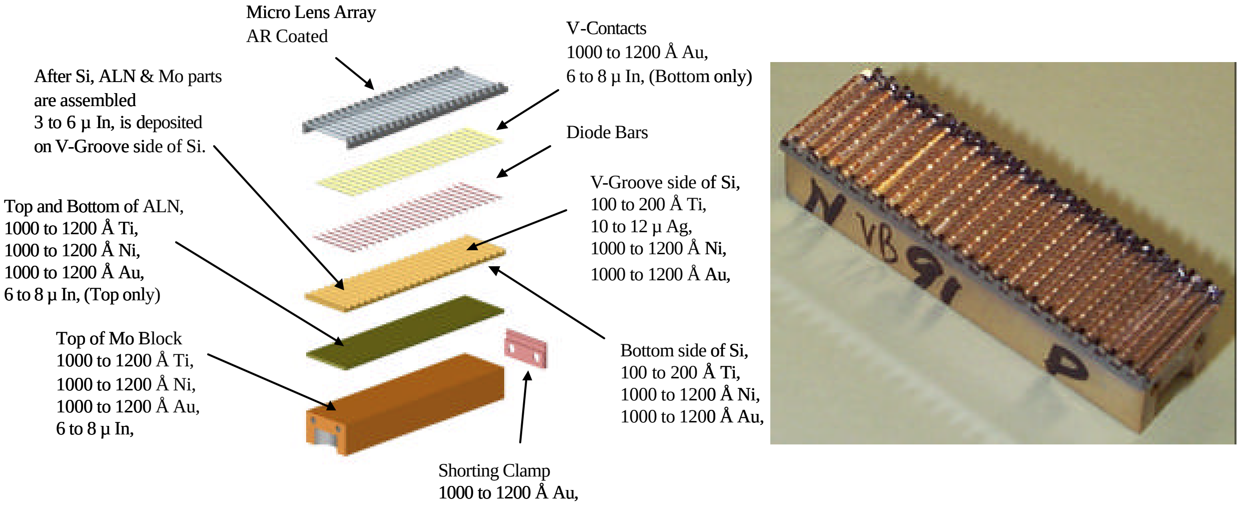

(a) (b)

Fig. 2.1.7.2 (a) Exploded diagram showing the various components of the V-BASIS package. (b) Photograph of a V-BASIS package.

Each V-BASIS diode package must go through an accelerated burn-in test for 18 hours at 75 Hz prf (~5 million shots) at a peak power corresponding to 115 W/bar. The tests allow us to weed out poorly performing tiles or repair ones in which only a few diodes bars fail. The repairs are done by disabling the electrical connections to the individual bars with small jumper plates. To date we have burned in more than 700 kW of tiles under these conditions, representing more than 7,000 individual diode bars giving us a bar yield above 98% as shown in Fig. 2.1.7.3.

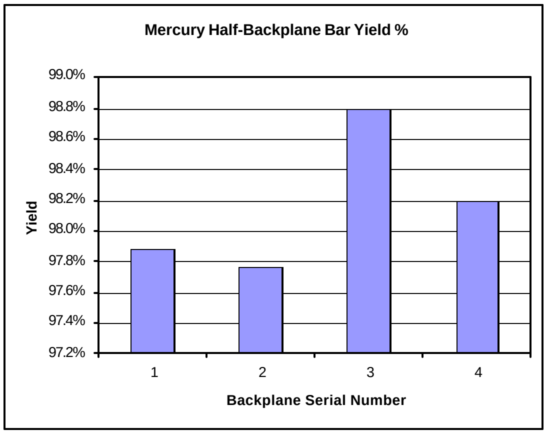

Fig. 2.1.7.3 The diode bar yield for the diode arrays fabricated this year is above 98%.

Backplanes

This year we planned to build four additional backplanes. Thus far, three units have been assembled (Fig. 2.1.7.4). The fourth backplane is currently being completed (Fig. 2.1.7.5). All four backplanes will eventually be used for pumping the second amplifier head. Each of the backplane units holds a total of 36 V-BASIS packages arrayed in a 6 x 6 configuration and can output a peak optical output pump power in excess of 80 kW at 900 nm. The design of the backplanes was modified to include: mounting plates that allow the backplanes to be easily locked in place, improved positioning and pointing controls, better insulation, and improved hardware on the backside to hold the electrical cabling more securely.

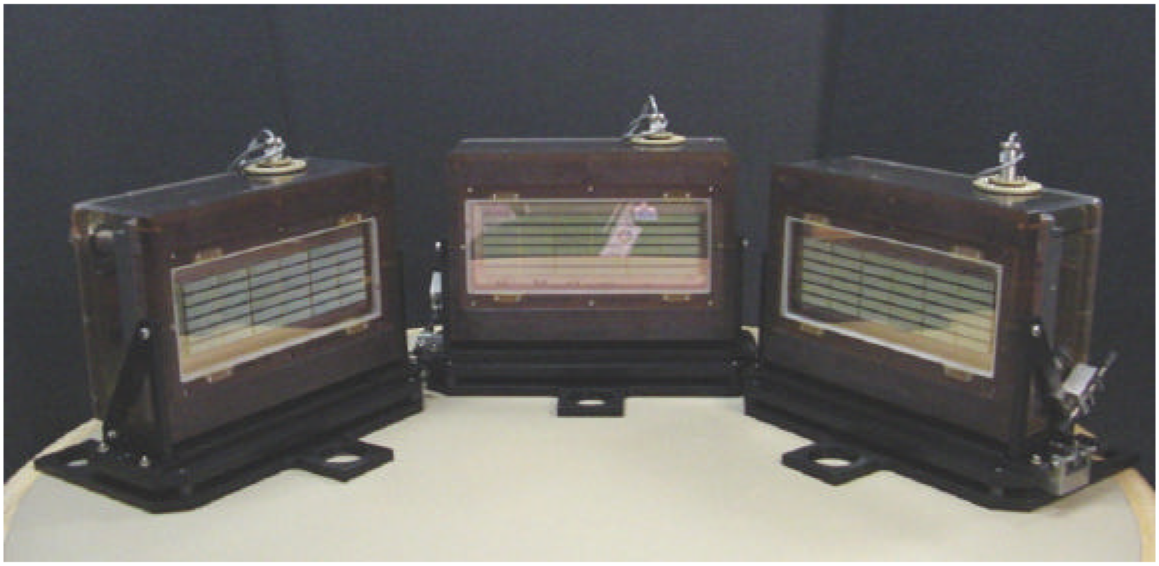

Fig. 2.1.7.4 Three new backplane units have assembled.

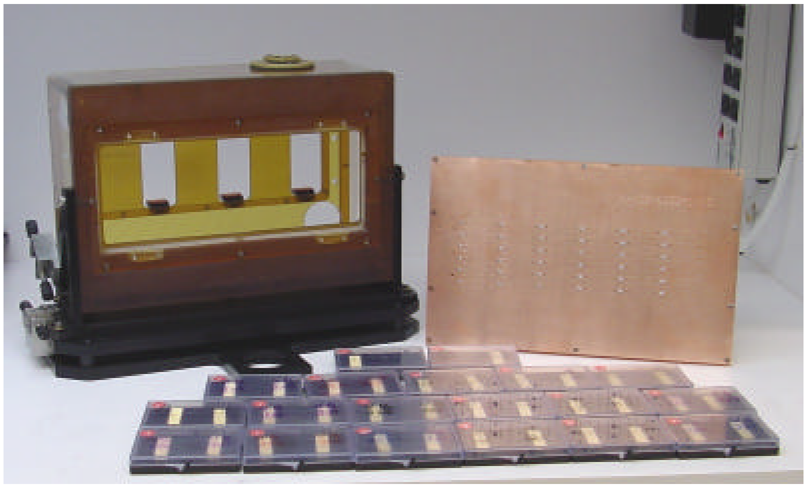

Fig. 2.1.7.5 Backplane #8 is under construction

2.1.8 Diode Power Conditioning

Our FY2002 tasks were:

- 36 power supplies and pulsers will be purchased and installed.
- Installation and full operation with at least $1x10^5$ shots for 4 new backplanes with upgraded control system

The activation of four 80 kW diode arrays for one amplifier head requires operating four bays each containing nine pulser chassis. Each set nine pulser chassis are located in hardware racks above the laser system (Fig. 2.1.9.1). All 36 pulser chassis were installed and operated along with the control system to regulate the voltage and current levels. The second amplifier will require 36 additional pulser chassis of which installation has been completed in Bays 5-8 as seen in the figure below. The new diode backplanes are soon to be operated and tested for individual performance milestones such as power and brightness.

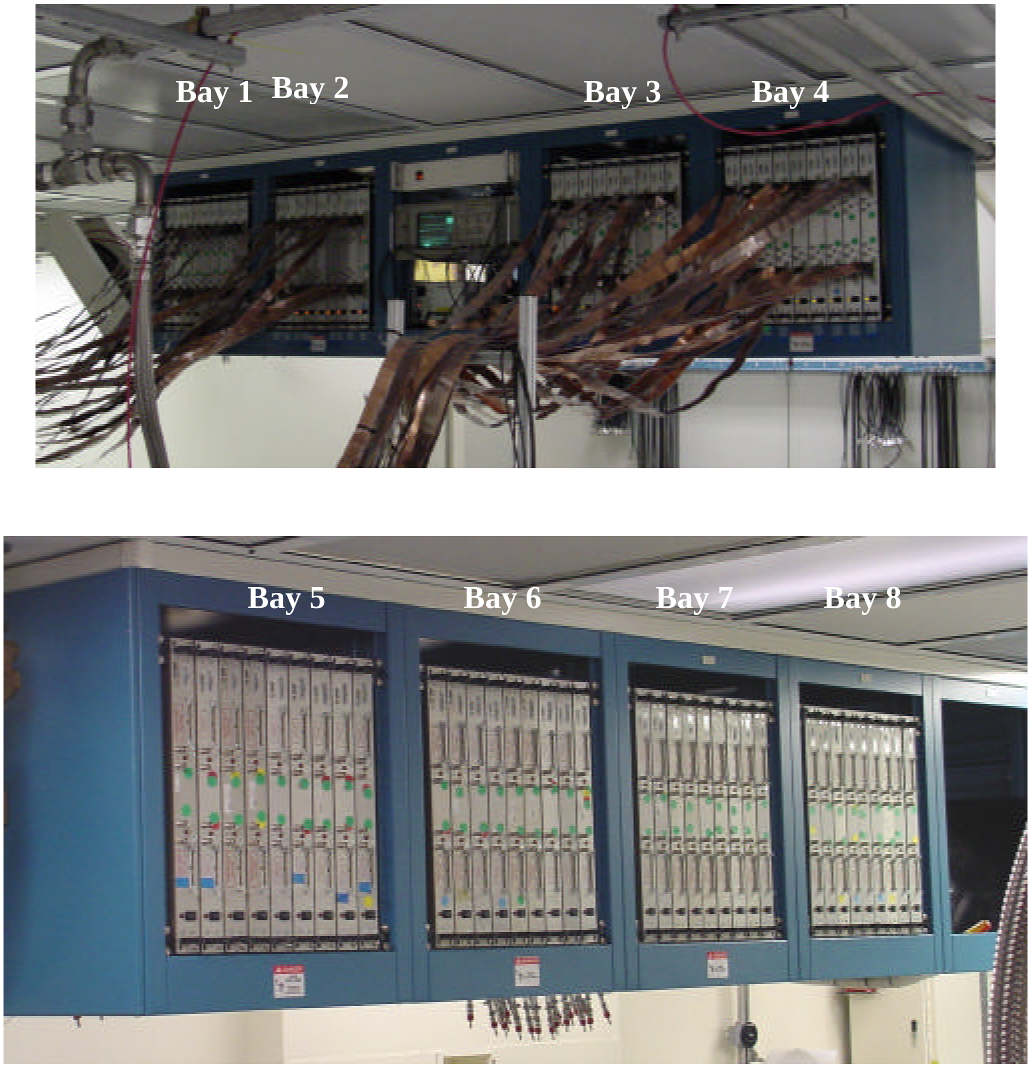

Fig. 2.1.8.1 Mercury pulser bays.

The pulse chassis are manufactured by Directed Energy, Inc. of Fort Collins, Colorado. Electrical connections to the power supplies and water cooling lines are on the backside of the units. Low inductance cable strips that bring power to the diode tiles and communication ports are located in the front. A typical waveform is shown in Fig. 2.1.8.2.

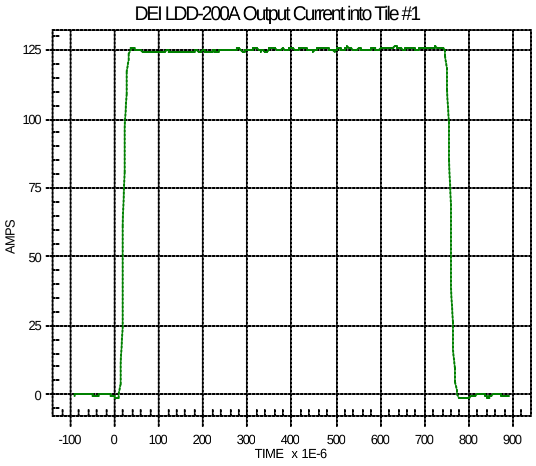

Fig 2.1.8.2 DEI pulser current waveform.

External DC power is shared among nine pulser chassis. The driver consists of two independent channels in a common enclosure. The drivers share common AC support power and DC high voltage. Each channel is independently controlled via an RS-485 port. The driver features advanced circuitry to protect both the diode and driver. The nominal and maximum operating parameters of the diode pulsers are given in Table 2.1.8.1

Table 2.1.8.1 Comparison of diode operating points and pulser limitations

PARAMETER	**NOMINAL LASER DIODE OPERATING POINT**	**MAXIMUM PULSER OUTPUT**
Current	110 A	200 A
Voltage	105 V	150 V
Pulse Width	750 µS	2 mS
Repetition Rate	10 Hz	10 Hz

A block diagram of the configuration of the system is shown in Fig. 2.1.8.3. Each set of nine pulsers has one dedicated power supply.

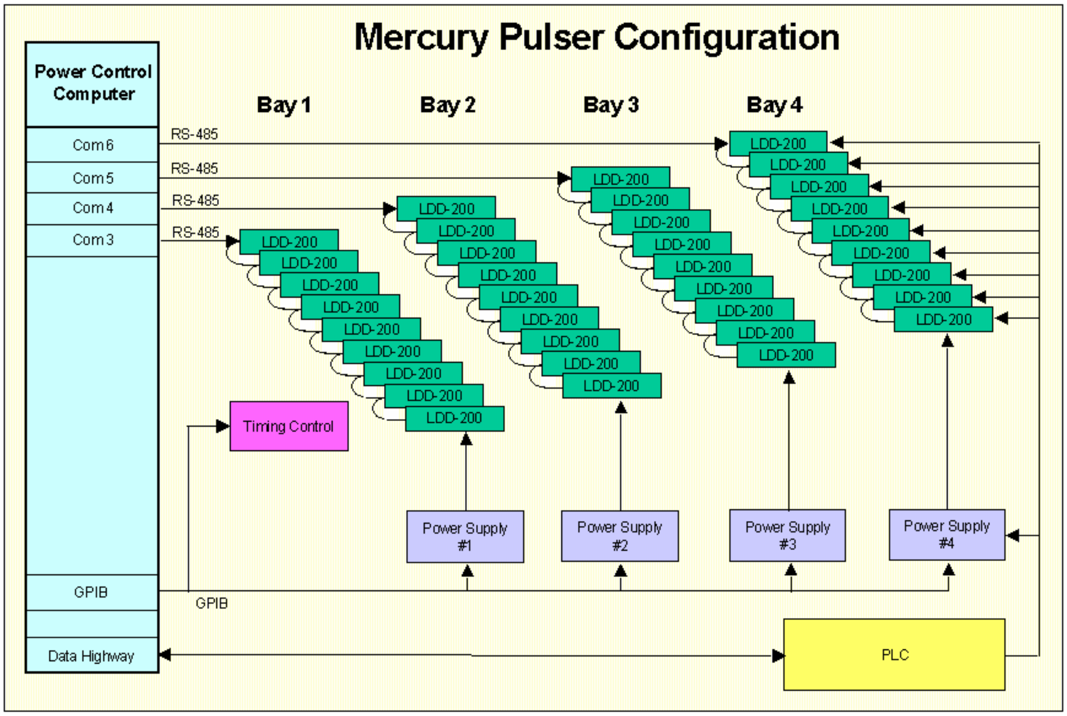

Fig. 2.1.8.3 Mercury pulser configuration.

Before the pulsers are assembled into the main laser, they are tested in an offline characterization lab (Fig. 2.1.8.4). The tests involve exercising the communication firmware and operational functionality at low powers. The test stand also allows 9 pulsers to be operated simultaneously to check for errors incurred during parallel operation. Once the pulsers have passed through the test stand, their status is entered into a data base, which serves to maintain the specific location, operational status, and repair history of each pulser.

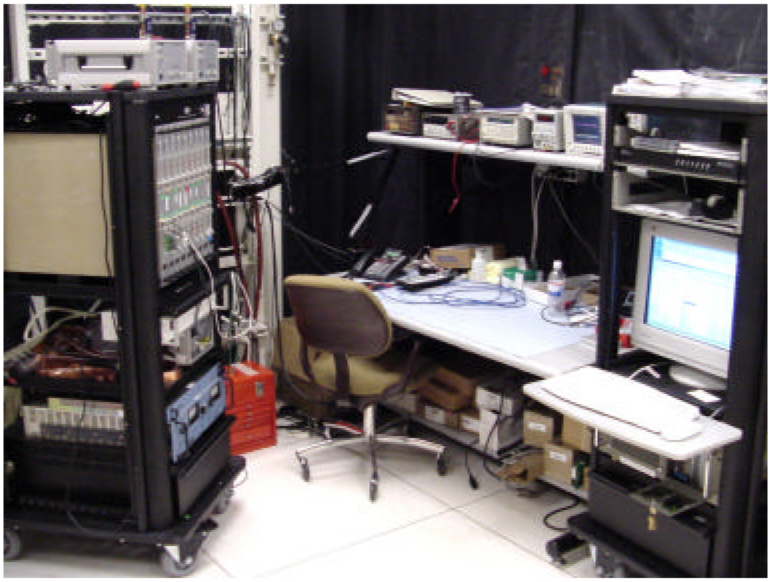

Fig. 2.1.8.4 Pulser test stand.

With the test stand and data base we have been able to systematically identify both design faults and random failures in the Mercury pulsed power system. The faults that we have identified and corrected are listed in Table 2.1.8.2. We have worked closely with the manufacturer of the pulsers to correct the faults and work toward the fully operational system that we have today. Table 2.1.8.3 lists the current set of problems that have not been resolved and will be addressed in the coming year. Since these problems do not severely restrict the operation of Mercury we have concentrated on resolving the most pressing problems.

Table 2.1.8.2 Summary of previous pulser faults and solutions

Pulser Fault	**Underlying Cause**	**Resolution**
Voltage sags during pulser operation	Current limiting diodes on the Cap banks were under sized and failed, resulting in undercharged cap banks.	Replace current limiting resistors with higher power components.
Pulsers report erroneous voltage sag error	Voltage sag test was set to close to beginning of the diode pulse. Diodes that were not yet "ON" would trigger a fault.	Voltage sag test was moved to center of the pulse and widened to reduce sensitivity to noise.
Pulsers stop communicating	Communications code in the pulser intermittently failed in a multiple pulser configuration.	The vendor altered the communications code and changed test procedures to include multi-pulser communication.
Voltage and current reported incorrectly	Each pulser has two methods of reporting voltage and current. Front panel monitors are used for connection to external test equipment and internal A/D converters are used for reporting through the serial port. The external monitors were calibrated by the vendor but the internal ones were not.	The design of the pulser's digital section was modified to allow for calibration of the internal and external monitors.
Fault communications loop to control system too long	The pulsers can only be communicated with via serial I/O and 18 pulsers are on a single I/O line. This results in up to a nine second delay from the time a pulser faults until the control system queries the pulser status.	The pulsers have been modified to include an additional I/O point that only reports the fault status of the pulser. The status on all 18 pulsers is monitored in parallel reducing loop time down to ~100ms.

Table 2.1.8.3 Unsolved pulser issues.

Pulser Fault	**Underlying Cause**	**Probable Resolution**
Pulser misses a command	Not fully known. A Pulser will intermittently not respond to a command	The driver in the control computer will be modified to re-issue a command if the pulser does not report proper status. A detailed investigation into the pulser will need to be launched to find the problem in the pulser communication section
All pulsers that are bussed together need to be at zero input voltage when they are enabled	If one pulser faults it is disconnected from the power source and cannot be re-connected until the DC supply is brought to zero. This forces all pulsers connected to that power supply to be turned off. This is due to the fact that the pulser input relay cannot be switched under load	The specification for the pulser for future procurements will be modified to rectify this problem

Summary

We have operated 36 dual channel pulsers and driven 4 diode backplanes. We have received and tested an additional 36 dual pulsers of which 27 of these units are installed in the Mercury laboratory and will be used to operate 4 additional backplanes in the coming year. We have an additional 9 pulsers for spare units. These spares will be used to investigate an upgraded control architectures designed to increase the response time of the system and thus its functionality.

2.1.9 Computer Controls

Our FY2002 tasks were:

- The control system software will be upgraded to accommodate the additional tiles added to the system and allow for the operation of 8 backplanes or 640 kW of diode power

The architecture of the Mercury Laser necessitates that an automatic control system be employed to meet the needs of the Laser. In its final configuration the Mercury Laser will have 288 diode pulsers, 8 DC power supplies, 4 timing control boxes, 4 diode cooling systems, 2 slab gas cooling systems, and several diagnostic systems.

System Hardware Architecture

A block diagram of the Mercury control system hardware architecture is shown in Fig. 2.1.9.1. The existing control system utilizes a single computer and programmable logic controller (PLC) to control the various aspects of the Mercury laser system. The computer is tasked with controlling the power to the diodes, the timing of the system, and acts as a user interface to the PLC. The PLC is tasked with control of the diode cooling systems, glass slab cooling systems, and with personnel and equipment safety.

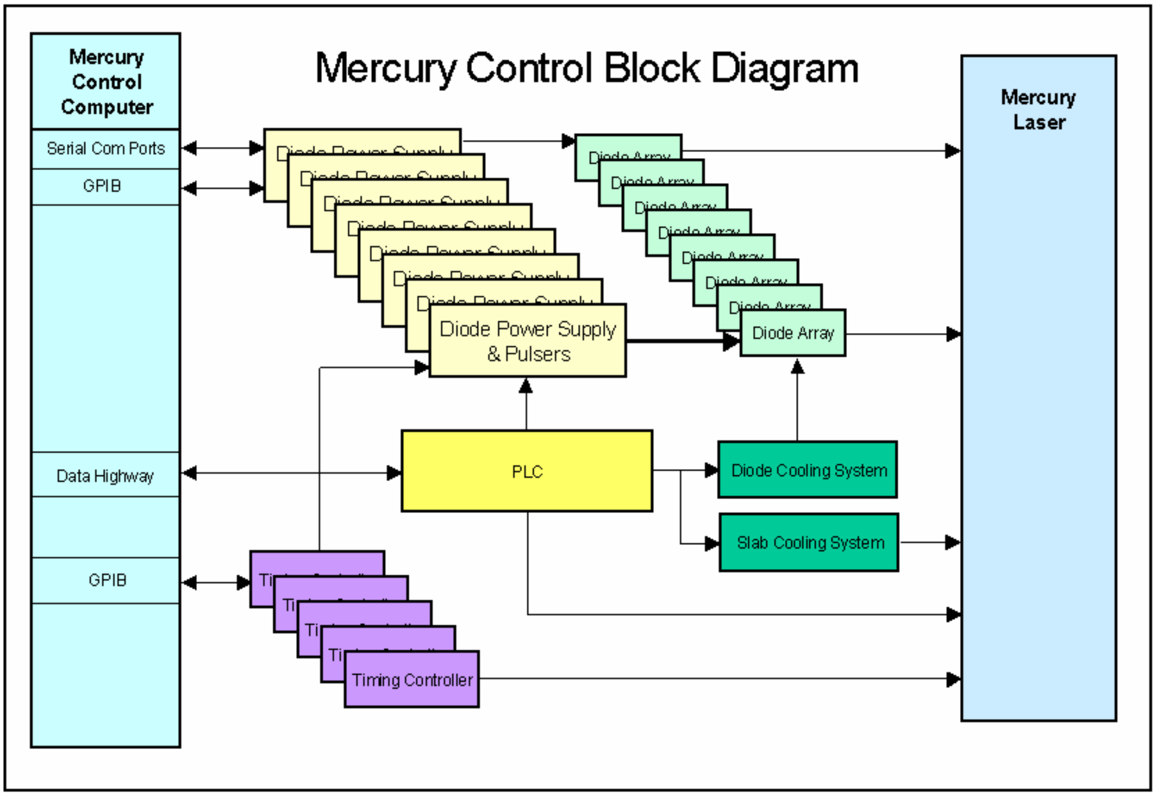

Figure 2.1.9.1 Current mercury control system architecture

System Software Architecture

The software in the control computer is written in LabVIEW and is designed to operate the diode power supplies and pulsers, the PLC, and the timing controllers. The software consists of modules providing a PLC Graphical User Interface and a Pulser Control Interface as shown in Fig. 2.1.9.2. The operator is kept appraised of overall status with the GUI in Fig. 2.1.9.2 and can get a more detailed view of any one bay of pulsers by viewing a pop-up screen like the one shown in Fig. 2.1.9.3. Each function in the software has a dedicated program loop such that a delay in one loop will not slow operation of the remaining control loops as long as there remains free CPU time. However, we have found that the current configuration of hardware and software (72 pulsers, 4 power supplies, 5 timing boxes, and 1 PLC) consumes 100% of the CPU and severely limits the responsiveness of the system.

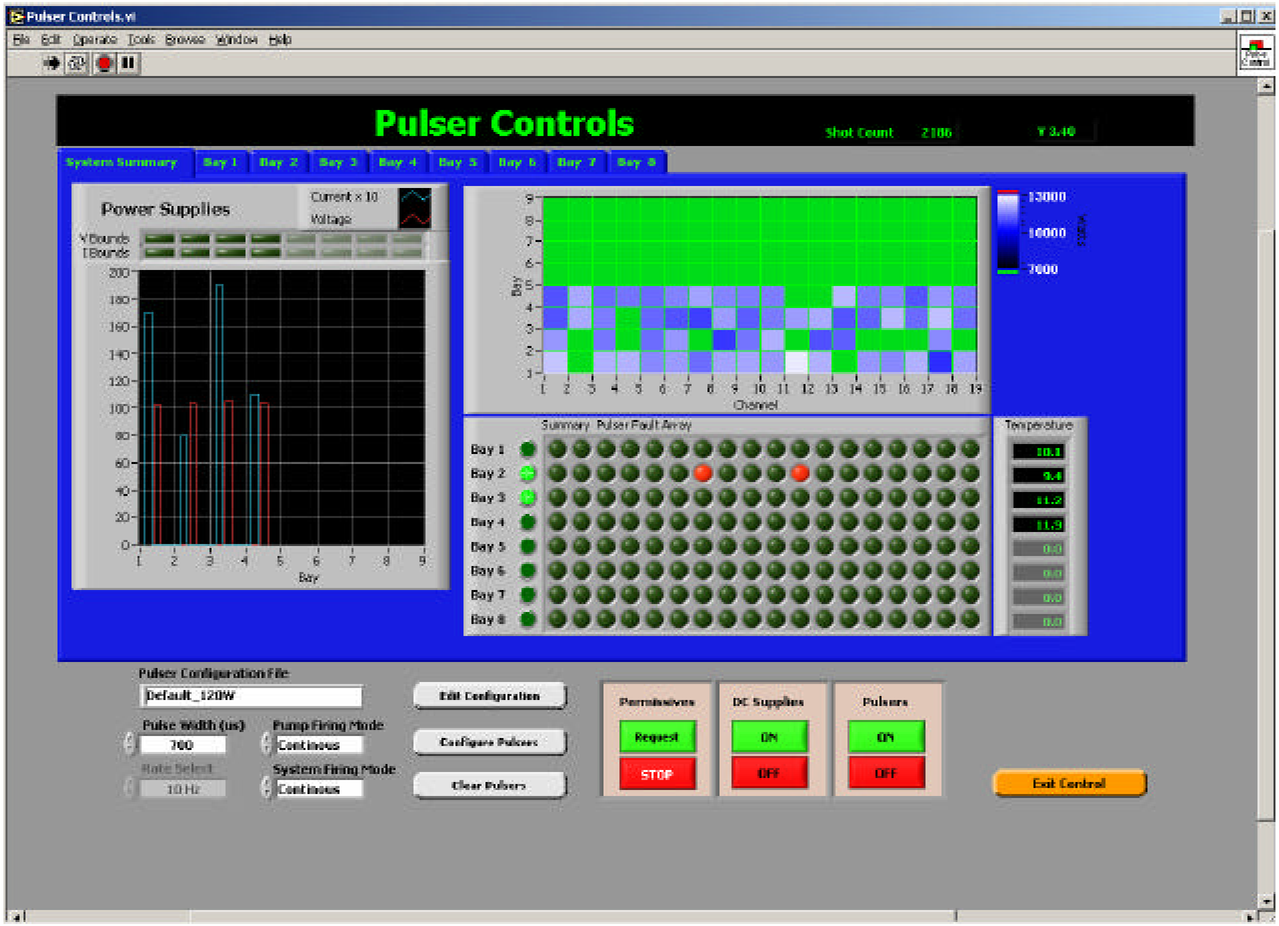

Shot Count 2186

V 3.40

Temperature: 10.1, 9.4, 11.2, 11.9, 0.0, 0.0, 0.0, 0.0

Pulser Configuration File: Default_120W

Pulse Width (us): 700

Pump Firing Mode: Continous

Rate Select: 10 Hz

System Firing Mode: Continous

Fig. 2.1.9.2 Operator interface overview

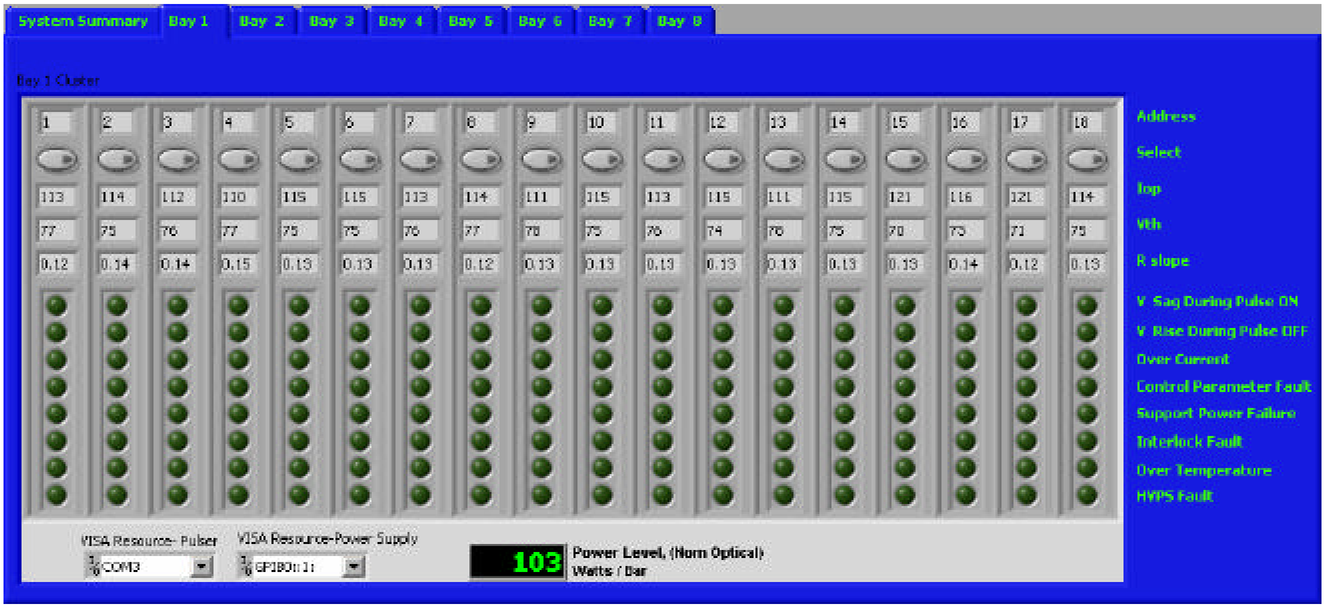

Address	1	2	3	4	5	6	7	8	9	10	11	12	13	14	15	16	17	18
Iop	113	114	112	110	115	115	113	114	111	115	113	115	111	115	121	116	121	114
Vth	77	75	76	77	75	75	76	77	78	75	76	74	78	75	70	73	71	75
R slope	0.12	0.14	0.14	0.15	0.13	0.13	0.13	0.12	0.13	0.13	0.13	0.13	0.13	0.13	0.13	0.14	0.12	0.13

VISA Resource- Pulser: COM3

VISA Resource-Power Supply: GPIB0::1::

103 Power Level, (Norm Optical) Watts / Bar

Fig. 2.1.9.3 Operator interface pulser bay status panel

In order to improve responsiveness of the system, as well as allow for the additional 72 pulsers and 4 power supplies that will need to be controlled we are preparing to distribute the controls among a number of different processors. Each bank of diode pulsers and attached power supply will be controlled by a separate computer whose function will be to control the hardware and report status back to a central control unit. A block diagram of this is shown in Fig. 2.1.9.4. The user interface shown here in this report will not change but the responsiveness of the control system will be vastly improved. The system will also be able to handle the increased number of pulsers and power supplies required for a full complement of eight diode backplanes. The current architecture of the software will allow for the transition to a distributed control system with very few software changes.

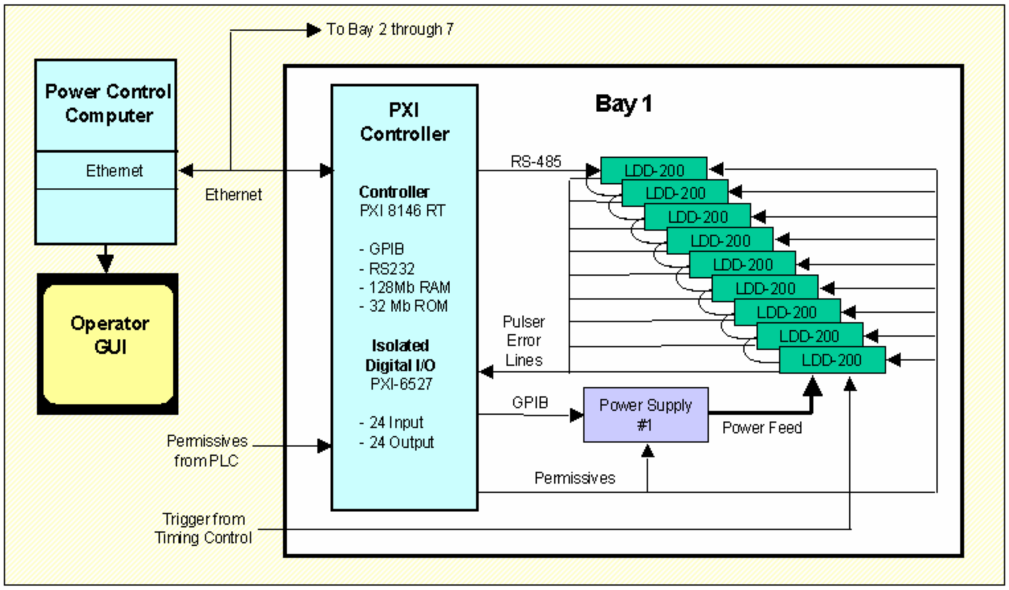

Fig. 2.1.9.4 Distributed control architecture.

2.1.10 Facility and hardware upgrades

- Full characterization and assembly of two pump delivery systems
- Activation of second amplifier head with seven Nd:glass surrogate slabs and evaluate flow performance.
- Installation of injection and reverser hardware into mail beamline
- Full installation, operation and interface of diode chillers and helium gas blower to control system

The amplifier, pump delivery, and reverser hardware were designed to accommodate many "lessons learned" changes and upgrades. The amplifier assembly shown in Figure 2.1.10.1

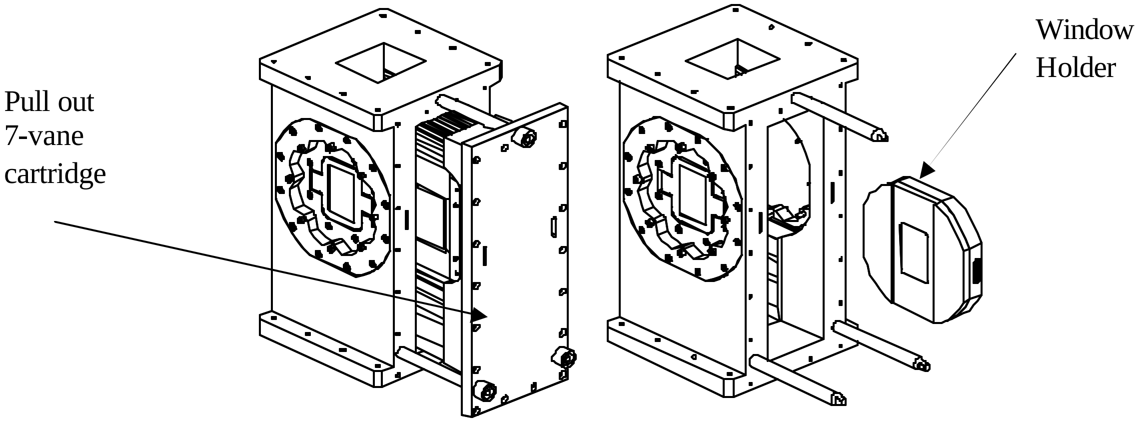

Fig. 2.1.10.1 Drawing of the new amplifier head assembly

The original amplifier cassette was modified to include several upgrades to allow for ease of use and access of optics. The internal 7-vane assembly was not altered only the housing hardware. Some of the improvements include:

- The vane cassette can be removed without disturbing the cassette holder and optical alignment of the laser and pump beams
- Three precision alignment pins help relocate the vane cassette upon reinsertion
- The amplifier window is now held in a separate mount and is removable through the same opening as the vane cassette
- The phase plate can be located within the amplifier assembly and has a water cooled option to the phase plate frame.
- An external feed line of helium can be used to minimize air turbulence around the plate.
- The cooling line capacity to the slab edge cladding in the vanes has been increased to help reduce the heat loading.
- The cassettes for both amplifiers are interchangeable
- The amplifier column rigidly has been improved by a factor of two.
- The cassette has been modified to allow for close coupling of the diode pump delivery optics.

The last option is the most significant since this will improve the pump uniformity and reduce the overall thermal wavefront distortions to the beam. The current amplifier hardware has a physical standoff which creates a 7% pump light loss and contributes to the pump and gain non uniformity. Photographs of the hardware assembly are shown in Fig. 2.1.10.2.

Fig. 2.1.10.2 Photos of the amplifier assembly.

The new amplifier assembly is shown along with the new pump delivery hardware in Fig. 2.1.10.3. The pump delivery components (lens duct and homogenizer) have been modified to allow x, y, z, tip and tilt adjustment while under vacuum and the lens at the end of the assembly can now be removed without disturbing the alignment of the lens duct and homogenizer. The lens will now also have 5-degrees of adjustment as well to help with collimation for the laser beam.

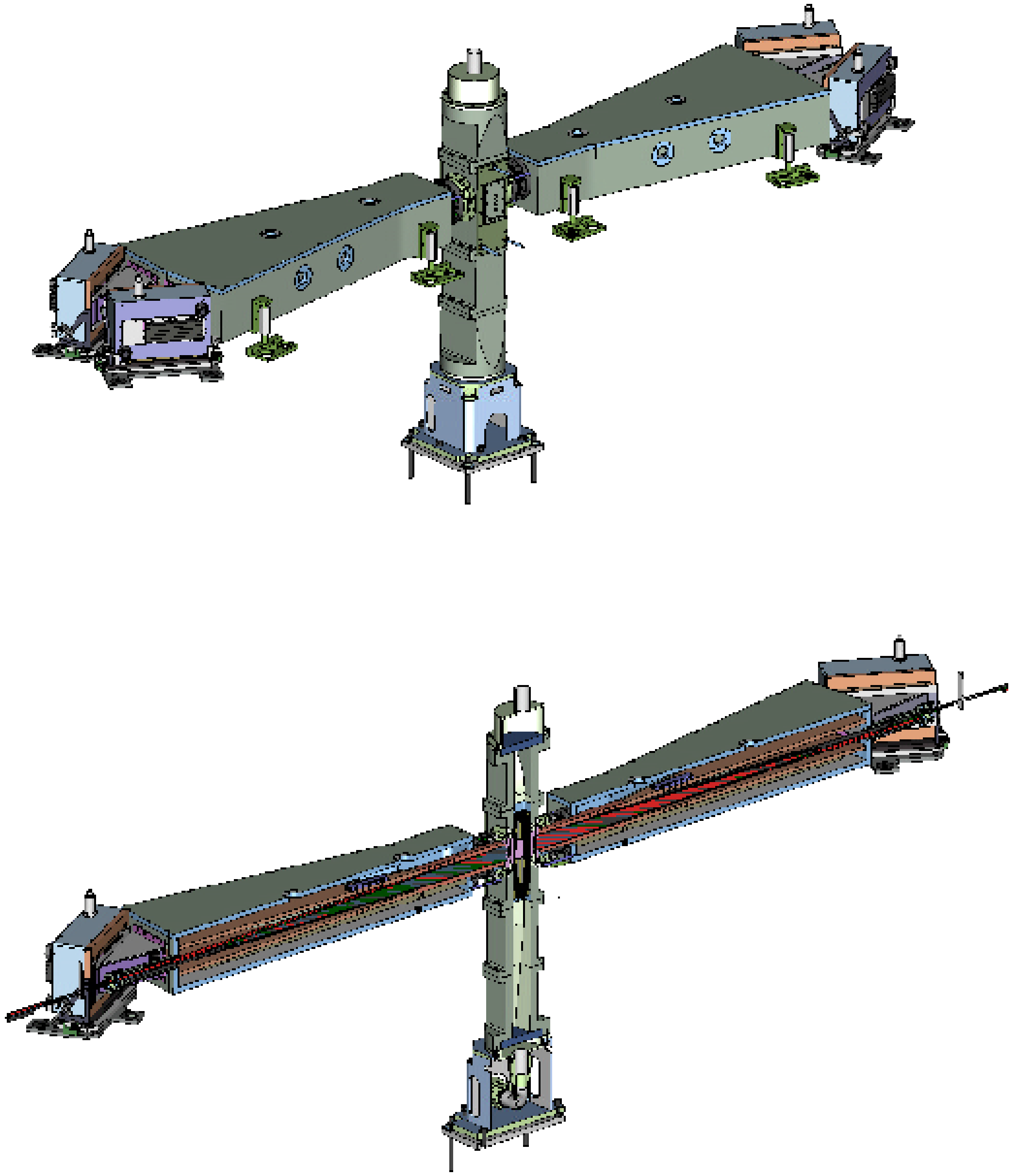

Fig. 2.1.10.3 The pump light delivery system and amplifier schematic showing the closely coupled hardware arrangement.

The new full scale reverser hardware and optics will accommodate the full expansion of the beam. The optics will be mounted on a vibrationally isolated optical platform (Fig. 2.1.10.4) and have four view ports to allow user to look at all optics within the enclosure. The reverser mirrors will have motorized controls. In this new design two windows and one turning mirror have been eliminated and the reverser mirrors will have kinematics mounts to allow for various alignment scenarios. The pinhole assembly will allow removal of pinhole plates with out breaking vacuum which will be important for pinhole closure studies at how power levels.

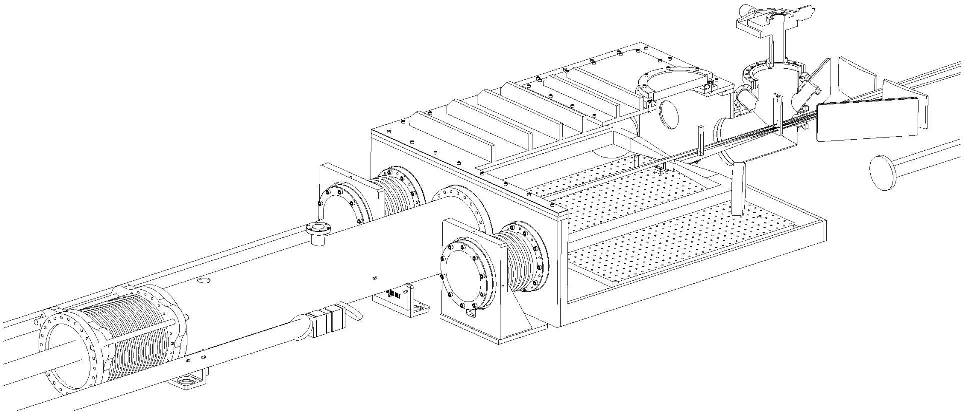

Fig. 2.1.10.4 Reverser assembly

The room layout and facility upgrades were designed and shown I Fig. 2.1.10.5. The new table enclosures with HEPA filters will allow the room to go from class 10,000 to class 100 environment and reduce air turbulence. Additional beam tubes will also help keep air turbulence low. Additional tables will allow for activation of the second amplifier and gas flow will be re-plumbed to allow one blower to accommodate two amplifiers. Dampening upgrades will also help reduce vibration.

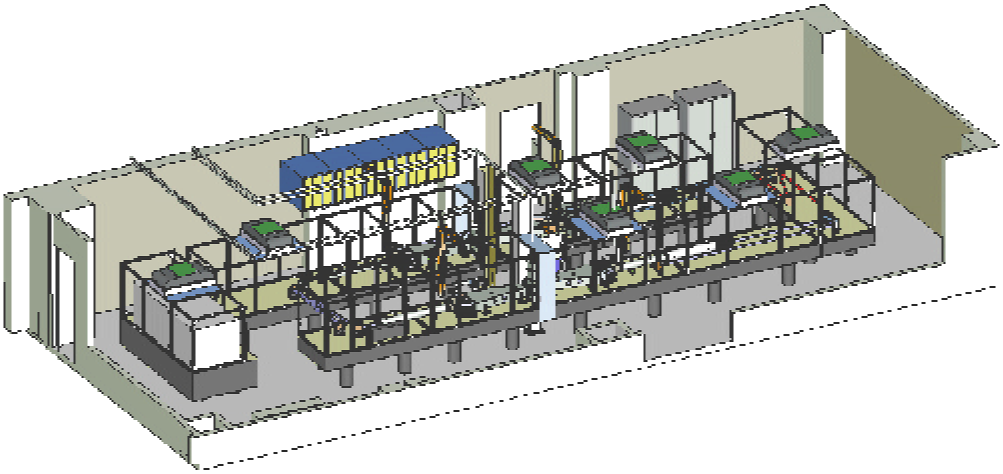

Fig. 2.1.10.5 Mercury laboratory with clean room closures and additional tables to accommodate the second amplifier.

In conclusion we have completed the amplifier, reverser, and pump delivery drawing packages. The amplifier was purchased and assembled offline. The room upgrades were modeled and costed however the installation of the amplifier and the purchasing of the other optics and room upgrades were delayed.

2.1.11 IRE System Modeling

Introduction

We are beginning to turn our attention to detailed energetic modeling of the successor to the Mercury Laser (Venus). Two issues that must be carefully considered when scaling laser apertures using the presently adopted Mercury laser amplifier geometry, are amplified spontaneous emission (ASE) and pump radiation delivery efficiency to the slabs. For Yb:S-FAP, the standard ASE treatments that have been used previously are inadequate because of the uniaxial nature of the S-FAP crystal and the very strong directional dependence that this causes in the Yb^{3+} emission and gain properties. As transverse and longitudinal amplifier slab dimensions are changed, the overlap of the delivered pump radiation to the gain region of the slabs also has to be carefully considered and is expected to change due to the finite divergence characteristics of the laser diode array pump sources. In the following sections a short description of our modeling work on these two aspects of aperture scaling is given.

ASE Model

Yb:S-FAP is a uniaxial crystal exhibiting a unique crystallographic direction, denoted as the c-axis, with different radiative emission and absorption characteristics depending on the radiation's polarization direction relative to this c-axis. For uniaxial crystals such as S-FAP, the refractive index properties are characterized by two values; the ordinary value, n_o=1.617, for light polarized perpendicular to the c-axis, and the extraordinary value, n_e=1.612, for light polarized parallel to the c-axis. For any light propagation direction in the crystal there will be two principal linear polarization directions for that direction, each characterized by its own unique index value. One of these principal polarization directions will be perpendicular to the c-axis and will be characterized by index value n_o. The other principal polarization direction is perpendicular the first one and can have spatial components both parallel to and perpendicular to the c-axis. This second principal polarization direction, is characterized by an index value given by the well known equation,

$$\frac{1}{n^2} = \frac{\cos^2(\theta)}{n_o^2} + \frac{\sin^2(\theta)}{n_e^2}\,, \tag{1}$$

where θ is the propagation direction of the light relative to the c-axis. Just as the refractive index value depends on the spatial polarization direction of the radiation, so do the emission and absorption cross section values.

To meaningfully model ASE in the Mercury Laser and larger systems, the dependence of emission and absorption cross sections with propagation and polarization directions must be understood. Just as with refractive index, absorption and emission cross section values are completely described by two sets of numbers corresponding to those for light polarized parallel and perpendicular to the c-axis. For light polarized perpendicular to the c-axis, the ordinary cross section values are used. The value for the other principal polarization direction is somewhat more complicated though. To derive the emission and absorption cross-sections for this principal direction, analogous to the refractive index value given by (1), we consider the refractive index to be a complex quantity with an imaginary part to account for both absorption and emission in the laser crystals,

$$n_c = n + j\,\frac{2\pi}{\lambda_0}\frac{\alpha}{2}\,, \tag{2}$$

where n_c indicates the complex refractive index value, and α represents the gain or loss per unit distance. The parameter α that is directly related to the Yb emission and absorption cross sections through,

$$a = n_2 s_{em} - n_1 s_{abs}\,. \tag{3}$$

Substituting (2) into (1) and noting that the magnitude of the imaginary part of the refractive index is typically 1000 to 10,000 times smaller than the magnitude of the real part, the following expression can be derived for the cross section seen by light propagating as an extraordinary ray,

$$s = \frac{s_o \dfrac{\cos^2(q)}{n_o^3} + s_e \dfrac{\sin^2(q)}{n_e^3}}{\left(\dfrac{\cos^2(q)}{n_o^2} + \dfrac{\sin^2(q)}{n_e^2}\right)^{\frac{3}{2}}}\,, \tag{4}$$

where the o and e subscripts refer to ordinary and extraordinary directions, respectively. Since the birefringence of S-FAP is so small, a further approximation to (4) can be made by setting n_o equal to n_e. Under this approximation (4) is conveniently rewritten as,

$$s = s_o \cos^2(q) + s_e \sin^2(q)\,. \tag{5}$$

The assignment of cross section values are summarized in Fig. 2.1.11.1.

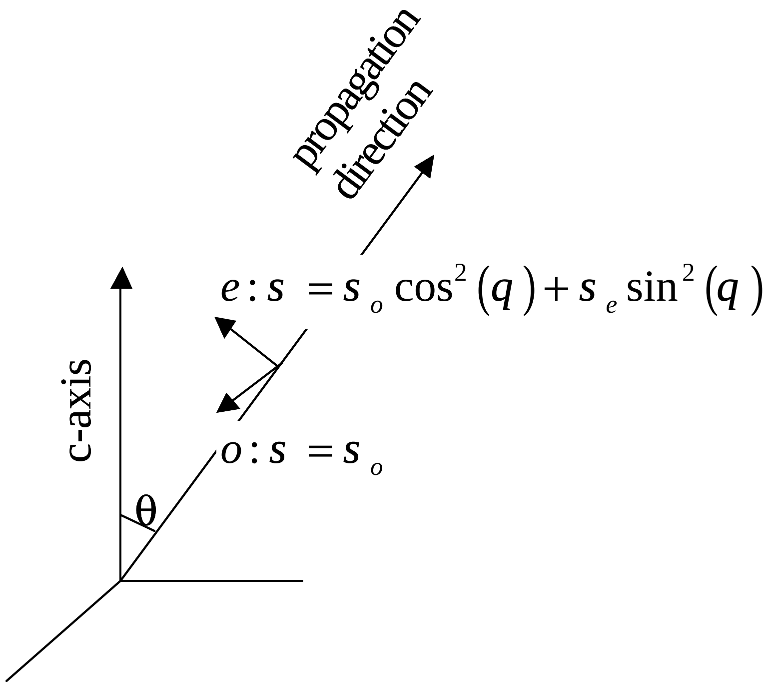

Fig. 2.1.11.1 The assignment of ordinary (o) and extraordinary (e) cross section values to the principal polarization directions for a given propagation direction.

The data plot in Fig. 2.1.11.2 shows the spectrally resolved σ_o and σ_e values for both absorption and emission that will be used in the subsequently presented modeling.

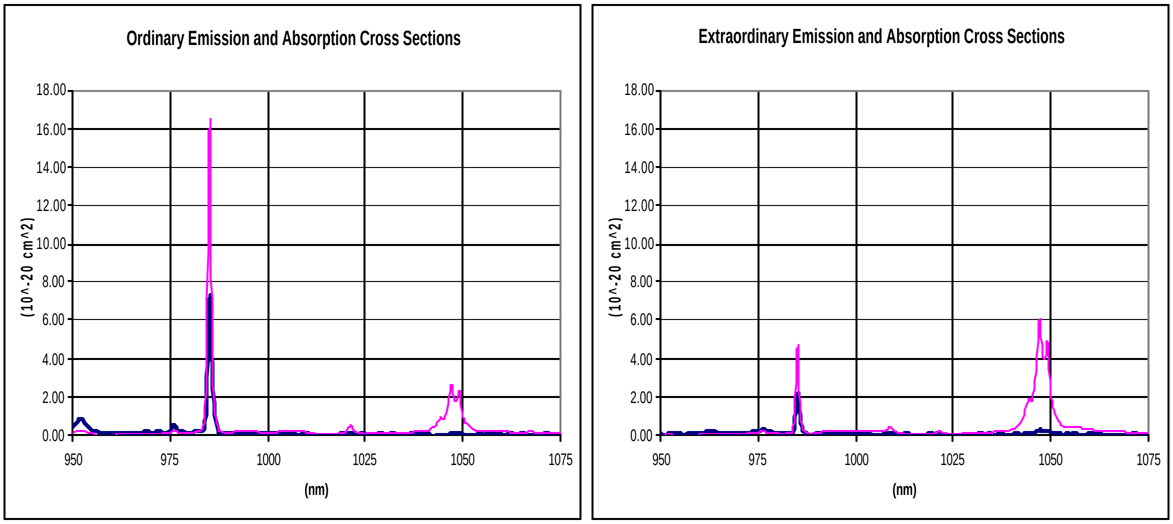

Fig. 2.1.11.2 Spectrally resolved ordinary and extraordinary emission (red) and absorption (blue) cross sections.

In modeling the impact of ASE on energy storage for Mercury-like laser systems, account must be taken of the close spacing between the individual slabs in a given amplifier head. ASE generated in a slab can, on intersecting that slab's output faces, be both reflected back into the original slab and transmitted into a neighboring slab. Assuming that no ASE energy is lost in traveling out of one slab and into a neighboring slab, an amplifier head can be modeled as one continuous solid of thickness equal to the thickness of the individual slabs as shown in Fig. 2.1.11.3.

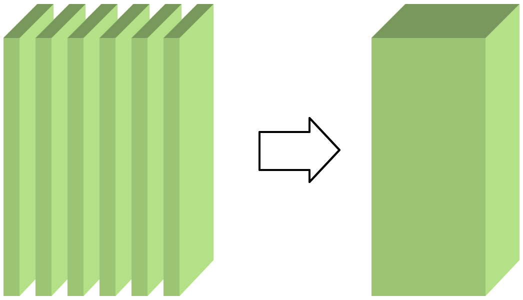

Fig. 2.1.11.3 In modeling the impact of ASE on energy storage, it is assumed the individual slabs in a given amplifier head behave the same as a single contiguous slab having a total thickness equal to the sum of the thickness' of the individual slabs.

We have developed a ray trace model to account for the impact of ASE on energy storage. The model calculates the ASE multiplier, M_{ASE}, which gives the ratio of the storage lifetime in the absence of ASE to the storage lifetime in the presence of ASE. In this model, spontaneous emission events are randomly distributed throughout the single contiguous slab representing the amplifier. To each spontaneous emission event, a random propagation direction is also chosen and stimulated emission is tracked along that direction. The ray is tracked until the ray either terminates by exiting an output face of the slab, or else hitting the clad region surrounding the slab. It is assumed the cladding is perfectly index matched to the slab so that any ray encountering the cladding is entirely removed from the slab.

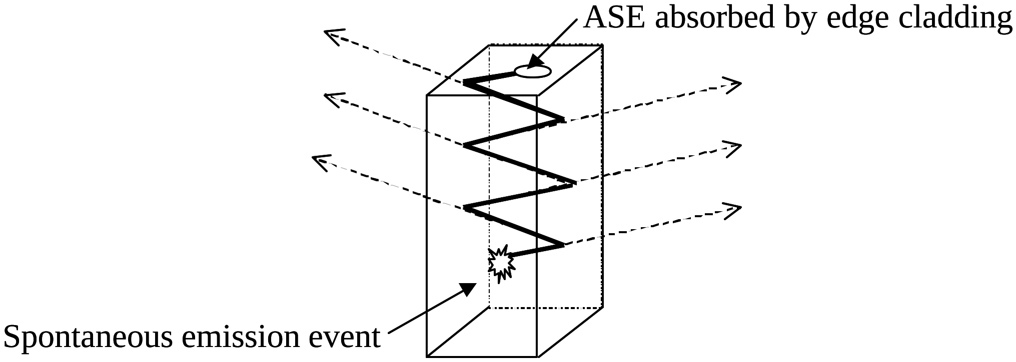

Fig. 2.1.11.4 Ray path traced in our ASE model tracks a ray from it's birth at spontaneous emission event to its death at the edge-cladding surrounding the slab. At each reflection off a slab face account is taken of the radiation lost to the surroundings as well as radiation reflected back into the slab.

To determine M_{ASE} by tracking individual ray paths as shown in Fig. 2.1.11.4, on needs to calculate the total number of photons that escape from the sample per spontaneous emission event. The sum of the total number of photons leaving the sample to the number of spontaneous emission events is then the desired ASE multiplier. The anisotropic nature of the Yb:S-FAP is accounted for using the foregoing formalism to assign two principal cross section values to each ray tracked, corresponding to the ordinary and extraordinary polarization directions. In our modeling several approximations are made in tracking the individual rays to keep the calculations manageable. First, rather than calculate individual paths corresponding to many straight line propagations between reflection interfaces as shown in Fig. 2.1.11.4, a method of images treatment is used to trace the rays in which the single contiguous laser slab, representing the individual slabs in a give amplifier, is reflected about its output faces, essentially straightening out the ray path as shown in Fig. 2.1.11.5.

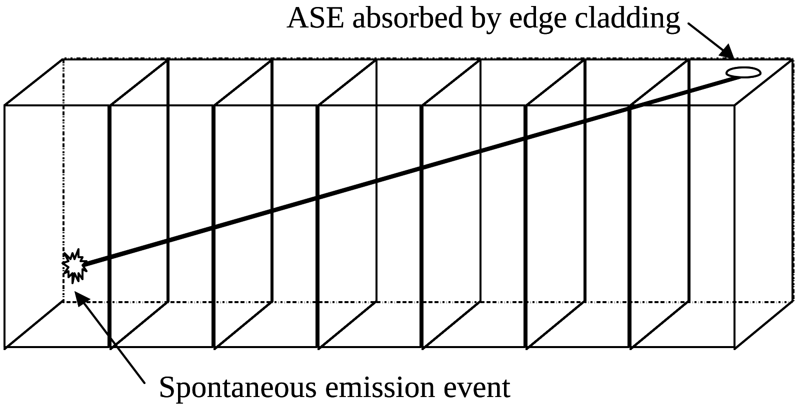

Fig. 2.1.11.5 A method of images construction in which the contiguous slab volume is repeatedly reflected about its output faces' is used to straighten the ray paths being tracked.

Another approximation made is that the individual rays do no change their polarization state on reflection, allowing the same ordinary and extraordinary principal cross section values to be used along the entire ray path. Finally, the polarization state of the light is ignored in calculated reflection and transmission coefficients at the contiguous slab output faces, and the average of the S and P polarized reflection and transmission coefficients are used. With these approximations the total number of photons emitted per spontaneous emission event due to ASE is straightforward to calculate:

$$N_{total} = e^{\alpha s_{first}}(T + R e^{\alpha s_{middle}}(T + R e^{\alpha s_{middle}} \ldots (T + R e^{\alpha s_{middle}}(T + R e^{\alpha s_{last}}))\ldots)), \qquad (6)$$

where R and T are the reflection and transmission coefficients at the slabs faces, respectively, α is the slab gain or loss per unit distance, s_{first} is the total distance traveled in the first contiguous slab in the method of images construction, s_{middle} is the total distance traveled in the middle contiguous slabs, and s_{last} is the total distance traveled in the last contiguous slab. The number of interfaces of the contiguous slab that are intersected by the ray between its birth at the spontaneous emission event, and its death at the cladding, is straight forward to calculate with the method of images construction shown in Fig 2.1.11.5. Labeling "n" as the number of times a ray intersects the contiguous slab output faces, (6) can be simplified as,

$$N_{total} = e^{\alpha s_{first}} \left\{ T \frac{1 - \left(R e^{\alpha s_{middle}}\right)^{n+1}}{1 - R e^{\alpha s_{middle}}} + \left(R e^{\alpha s_{middle}}\right)^{n} R e^{\alpha s_{last}} \right\}. \qquad (7)$$

Finally, M_{ASE} is calculated by tracking many rays,

$$M_{ASE} = \frac{\sum_{spontaneous\,events} P_{event} N_{total}}{\sum_{spontaneous\,events} P_{event}}, \qquad (8)$$

where P_{event} is used to account for the differing spontaneous emission probabilities depending on emission direction and polarization. It is worth noting that the analysis and modeling being done here accounts equally well for both ASE and radiation trapping effects. Particularly in quasi-three level systems such as Yb:S-FAP, trapping can be important, and is generally beneficial to overall laser performance.

As a specific example of the model, Fig 2.1.11.6 shows the calculated M_{ASE} parameter as a function of excited state fraction in the currently configured Mercury amplifier head. The particular assumptions regarding the calculation are summarized in Table 2.1.11.1.

Table 2.1.11.1 Current Mercury Amplifier Configuration

5	slab height (z-axis aligned with extraordinary index) (cm)
3	slab width (x-axis aligned with ordinary index) (cm)
3.75	total slab thickness (y-axis aligned with ordinary index) (cm)
1.617	ordinary refractive index
1.612	extraordinary refractive index
8.00E-20	wavelength averaged spectroscopic absorption cross section (cm^2)
2.00E+05	pump power (W)
1.00E-03	pump pulse duration (s)
900.00	pump wavelength (nm)
0.81	lower level Boltzmann factor (fa_p)
0.01	upper level Boltzmann factor (fb_p)
1.10E-03	lifetime without ASE or trapping (sec)
1000	number of rays launched for ASE calculation

At each excited state fraction for which M_{ASE} was calculated in Fig. 2.1.11.6, 1000 rays were randomly launched and then tracked in the calculation. Also shown is the functional fit to the data,

$$M_{ASE} = p1 + (p2 - p1)e^{EF/p3} \tag{9}$$

where p1, p2 and p3 are adjustable fit parameters.

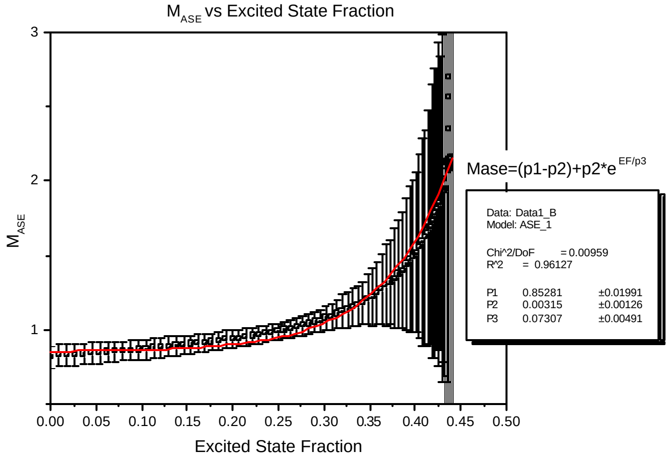

Fig. 2.1.11.6 M_{ASE} plotted as a function of excited state fraction for the current Mercury amplifier configuration summarized in Table 2.1.11.1. The error bars show the standard deviation of the calculated M_{ASE} parameter. The red line shows a functional fit to the data as described in the text.

The data shown in Fig. 2.1.11.6 is useful for calculating the pump excitation of Mercury-like amplifier systems. In doing this however, it is important to keep in mind that one of the approximations made in our present treatment is that the M_{ASE} parameter is uniform through all the slabs, i.e., there are no transverse or longitudinal spatial variations included in M_{ASE} in the present model. Fig. 2.1.11.7 depicts the calculated excited state fraction as a function of time into the pump pulse for the pump excitation sequence summarized in Table 2.1.11.1 and using the M_{ASE} parameter data of Fig. 2.1.11.6.

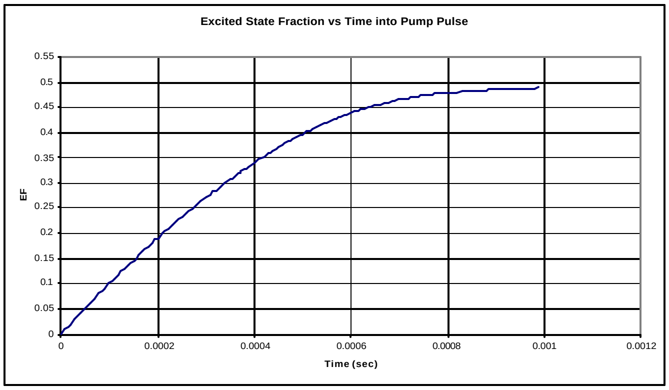

Fig. 2.1.11.7 Excited state fraction vs time into the pump pulse for the pump excitation sequence summarized in Table 2.1.11.1 and using the M_{ASE} parameter data of Fig. 2.1.11.6.

Pump Overlap with Slabs

In modeling scaled Mercury-like systems in which lower doped and thicker slabs may be utilized, it is important to correctly account for the overlap between the doped slabs and the expanding pump light as it propagate from slab to slab as shown in Fig. 2.1.11.8.

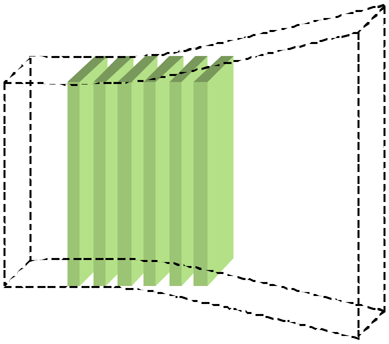

Fig. 2.1.11.8 As the pump light propagates from slab to slab it continues to expand. Slabs closest to the homogenizer have better overlap with the pump than those farther away.

The measured pump irradiance profiles at ever increasing distances from the output of the duct homogenizer used in the Mercury system is shown in Fig. 2.1.11.9. As seen in Fig. 2.1.11.9 the pump beam expands due to diffraction as it propagates away from the duct.

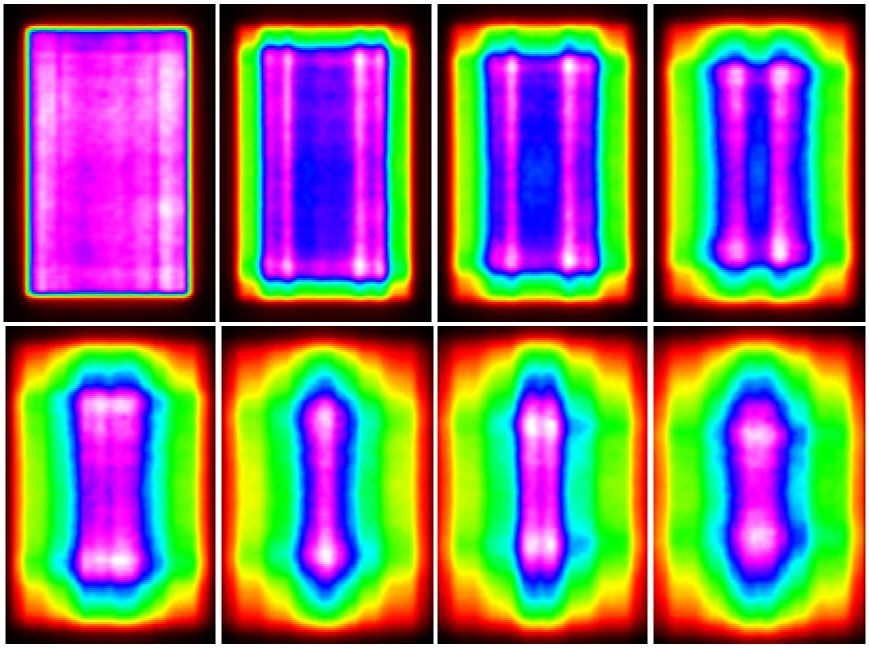

Fig. 2.1.11.9 Measured pump irradiance profiles at ever increasing distances from the output of the duct homogenizer used in the Mercury system. Starting at the upper left and going clockwise, the profile locations measured from the duct location are: duct homogenizer output or 0 cm, 1st slab location or 1.2 cm, 2nd slab location or 1.8 cm, 3rd slab location or 2.3 cm, 4th slab location or, 2.9 cm, 5th slab location or 3.5 cm, 6th slab location or 4.0 cm, and 7th slab location or 4.6 cm.

To incorporate this data into our energetics model we have measured the transverse size of the beams at each of the locations called out in Fig. 2.1.11.9 and then fit the half widths of the profiles, W, to the following expression,

$$W^2 = W_0^2 + \left(q_{HW}\ z\right)^2 , \tag{10}$$

which describes the behavior of the beam half-width with propagation after exiting the duct. In general, paraxial propagating beams are characterized by a constant divergence angle, θ_{HW} in free space propagation. Fig. 2.1.11.10 plots the half-width data of Fig. 2.1.11.9 and shows the overlay with the functional fit of the data to expression (10).

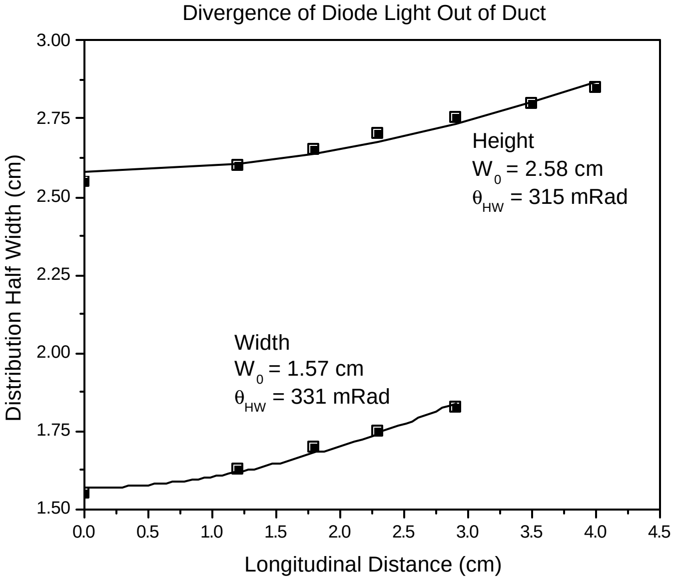

Fig. 2.11.1.10 Measured pump beam half-width in both the height and width dimension on exiting the duct homogenizer as a function of the longitudinal propagation distance out of the homogeneizer. The solid lines are fits of expression (10) to the data.

In our energetics modeling the fits to the data shown in Fig. 10 are used to calculate the overlap of the pump beam with the slabs in the amplifier heads using the following expression,

$$h_{overlap} = \frac{h_{slab} w_{slab}}{\sqrt{W^2_{0-height} + q^2_{hw-height} z^2_{slab}}\sqrt{W^2_{0-width} + q^2_{hw-width} z^2_{slab}}} , \tag{11}$$

where the various parameters are from the functional fits in Fig. 9, and z represents the optical path length from the center of the slab to the output of the duct.

System Modeling

Applying the foregoing modeling to Mercury-like laser systems, we can find the optimal tradeoff between transverse slab size and Yb doping density as the slab size increases. From a scaling point a view, there are obvious advantages to scaling the transverse aperture size of the laser system so that larger pulse energies can be extracted from a single beam line. However, just increasing the slab size alone quickly puts one into a regime where ASE losses are unacceptably high. To some extent, this ASE problem can be mitigated if as slab aperture size is increased, slab-doping density is concomitantly decreased, such that the transverse gain in the laser slabs remains a constant. However, to maintain constant pump absorption as the slab doping density is dropped, the slab thickness must be increased as doping density decreases. This increase in slab thickness leads to a decrease in the overall coupling of the pump light to the slabs because of the pump divergence problem discussed in the last section. An additional issue associated with increasing slab thickness is the impact it has on stress loading. All other things remaining constant, increasing the slab thickness and simultaneously decreasing the slab doping density, such that the pump absorption through the slab is unchanged, has the effect of increasing the fraction of fracture the slab is operating at by the same factor that the slab thickness was increased. To get an overview of what will be possible in terms of slab aperture scaling, we consider two specific slab doping densities. The first density considered is 3×10^{19} /cm^3 which is higher than the optimized slab doping density for the current Mercury laser geometry with 0.75 cm thick slabs. At this doping density we further consider two scaled slab apertures, one with transverse dimensions of 10 x 15 cm and one with transverse dimensions of 20 x 30 cm. In all cases, we hold the delivered pump intensity to each side of the amplifier heads at the ~10 kW/cm^2, representative of the Mercury laser system. The optical-optical efficiencies possible for these systems are plotted in Fig. 2.11.1.11 as a function of B-integral (i.e. nonlinear phase accumulation), with the black dashed line representing the 10 x 15 cm aperture and the dashed red line representing the 20 x 30 cm aperture. Assuming the maximum permissible B-integral at which the system can be safely operated is ~3 Radians, then the optical efficiency drops from 25% to 13% in going from the smaller to the larger slab aperture.

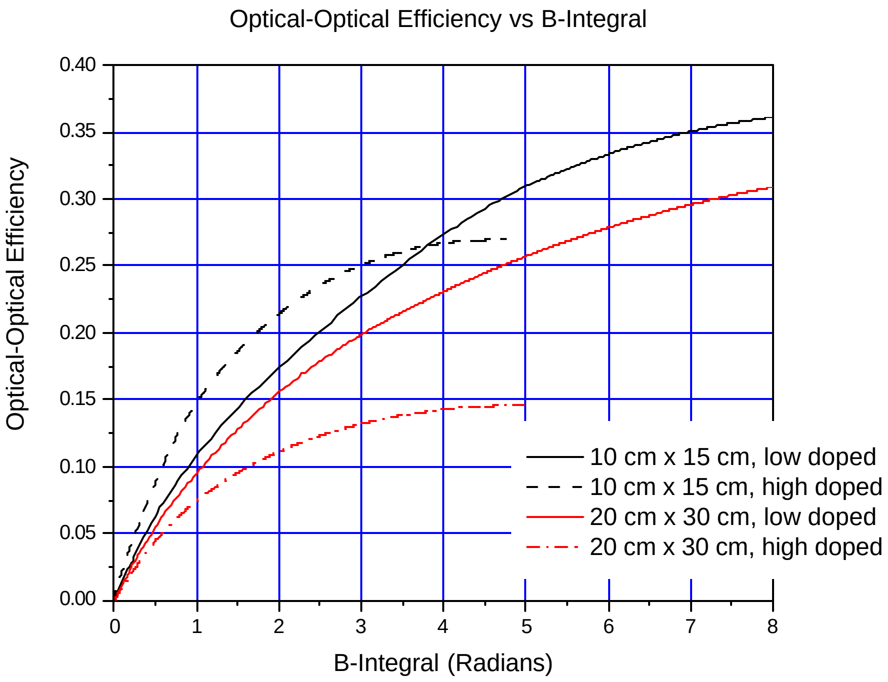

Fig. 2.11.1.11 Optical-optical efficiency from a Mercury like laser amplifier system as a function of B-integral. Varying the front-end pulse energy injected into the system varies the B-integral. For each slab aperture investigated, two different doping densities were also investigated as explained in the text.

Also shown in Fig. 2.11.1.11 are optical-optical efficiencies for the same slab aperture sizes, but with the slab doping density reduced by a factor of three to 1×10^{19}/cm^3 and the slab thickness increased by the same factor of three to 2.25 cm. Comparing the smaller slab aperture sizes (the dashed and solid black lines) with the two dopings at 3 Radians of B-integral, it is seen that the heavier doped and thinner slabs have higher efficiency, 25%, than the lighter doped and thicker slabs at 23%. This is because, in this region of the parameter space, the loss in pump overlap in going to the thicker and lighter doped slabs dominates the gains made due to better ASE performance in the lighter doped slabs. However, the situation is reversed at the larger slab aperture size of 20 x 30 cm. Here, the lighter doped and thicker slabs have higher efficiency, 20%, than the heavier doped and thinner slabs at 13% (the solid and dashed red lines in Fig. 2.11.1.11). At this larger aperture size, the improved ASE situation in the lighter doped and thicker doped slabs dominate the loss in pump overlap in going from the thin and heavier doped slabs to the thick and lighter doped ones. Table 2.11.1.2 summarizes the performance characteristics of the four systems described in Fig. 2.11.1.11.

Table 2.11.1.2 Performance summary of the four systems described in Fig. 2.11.1.11

	System 1	**System 2**	**System 3**	**System 4**
Yb doping density	$3x10^{19}/cm^3$	$1x10^{19}/cm^3$	$3x10^{19}/cm^3$	$1x10^{19}/cm^3$
Aperture size	10 x 15 cm	10 x 15 cm	20 x 30 cm	20 x 30 cm
Slab thickness	0.75 cm	2.25 cm	0.75 cm	2.25 cm
Front-end energy for B-integral = 3 Radians	1.6 mJ	0.1 mJ	5.51 J	1 mJ
Output Energy for B-integvral = 3 Radians	1.56 kJ	1.44 kJ	3.29 kJ	4.96 kJ
Opt-opt efficiency	0.25	0.23	0.13	0.20
Average slab overlap with pump	0.98	0.95	0.99	0.98
Average slab fraction of fracture	0.18	0.61	0.21	0.62

Summary

We have developed a suitable model that accounts for ASE in a Mercury-like architecture. We found that 20 cm x 30 cm slab apertures can be considered if optical-optical efficiencies of 20% are acceptable. In going to these larger aperture sizes, lower Yb doping and thicker slab dimensions are required to properly balance the impacts of both ASE and pump delivery efficiency. Employing our pumping, extraction, and propagation models, we are proceeding with the design of the next generation system.

2.2 Chambers

2.2.1 Magnetic Protection

In FY02 we began to develop a concept for a magnetically protected variation of the SOMBRERO power plant design. Our FY02 tasks in this area were:

- Install and learn operation of LSP code.
- Benchmark LSP results against those obtained by John Perkins.
- Calculate time-of-flight spread without an external field.
- Obtain ion fluxes resulting from transport of direct-drive target output through 10 mTorr of Xe.
- Use LSP to simulate plasma expansion in uniform and mirror field configurations.
- Design shielding for deflection magnet configuration.
- Use finite element code to generate magnet designs.
- Consider the effects that the expanding plasma ball has upon the external magnetic field.
- Propose experiments and calculations that enable benchmarking and testing of LSP.
- Recommend future work.

The expansion of an energetic plasma into a uniform magnetic field has been addressed from a theoretical perspective [1,2]. Simple, one-dimensional (1D) relations suggest that the 400 MJ direct-drive target would "blow a bubble" of ~4.3 m, which is roughly two-thirds of the distance to the 6.5-m-radius chamber wall. This would occur with a vacuum field of ~0.9 T. If the first wall can be assumed to be a flux-conserving (conductive) surface, then the required field falls to only 0.6 T. One possible configuration that could provide the uniform magnetic field is shown in Figure 2.2.1.1.

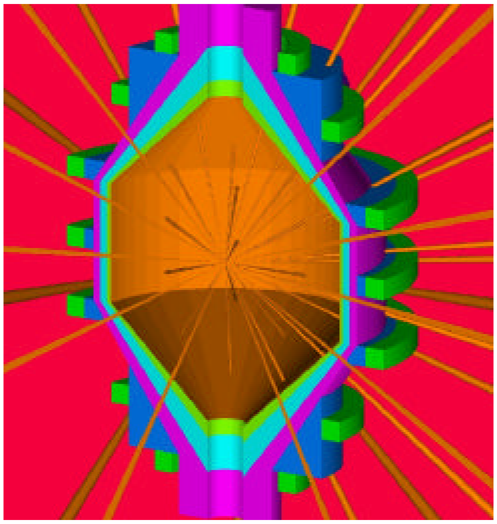

Fig. 2.2.1.1 With minor modifications to the SOMBRERO chamber design, it could be fitted with a set of seven superconducting magnet coils, which would provide a uniform (to within ~1%) magnetic field inside the chamber. In this picture, sixty incoming laser beams are shown. The superconducting coils, which have a 1 × 1 m cross section, are shown in green. Shielding (shown in dark blue) will maintain radiation damage rates at low enough levels such that the coils will not require replacement during the power plant lifetime.

Non-ideal effects, such as the Raleigh-Taylor instability at the plasma-vacuum (or plasma-gas) interface, will lead to fingering that would allow portions of the plasma to expand beyond the mean bubble radius. While the 1D radial expansion has been studied experimentally [3,4], neither the axial expansion nor the non-ideal effects have been adequately investigated.

In this past year, much progress has been made in modeling the expansion of a high-energy plasma in a uniform magnetic field. After consulting with numerous experts in the field, we obtained a state-of-the-art particle-in-cell (PIC) code from Mission Research Corp (MRC). The LSP code was ported to several multi-processor computer platforms operating at NERSC and LLNL. LSP has also been run on a fast PC under WINDOWS 2000.

Although we had hoped to benchmark LSP against previous work completed by John Perkins in collaboration with General Atomics (GA), this has not been possible. The principal investigator has left GA, and adequate details from his simulations are unavailable. Instead, we have attempted to benchmark LSP using a uniform magnetic field.

LLNL has added several new diagnostics to LSP to track plasma beta and the magnetic field at various locations within the IFE chamber. Additional diagnostics have been incorporated so that when the code becomes unstable, it gracefully ends. This enables a post-failure analysis to be performed, which improves future operations. LLNL also modified LSP to handle files that contain an externally generated list of non-uniform grid points. This enables LSP to use a finer mesh where needed. Finally, LSP was upgraded so that it can process a list of magnetic field data generated by the finite element code TOSCA. With this option, a realistic, three-dimensional (3D) set of external magnetic coils can be simulated.

Many two-dimensional (x-y) radial expansion simulations have been performed. In addition, several r-z simulations have also been completed. Figure 2.2.1.2 shows the expansion of the ions from a 400 MJ yield direct-drive target. The plasma expands into a vacuum with a 0.8 T uniform magnetic field. A chamber radius of only 3.5 m was used in order to simplify the calculation.

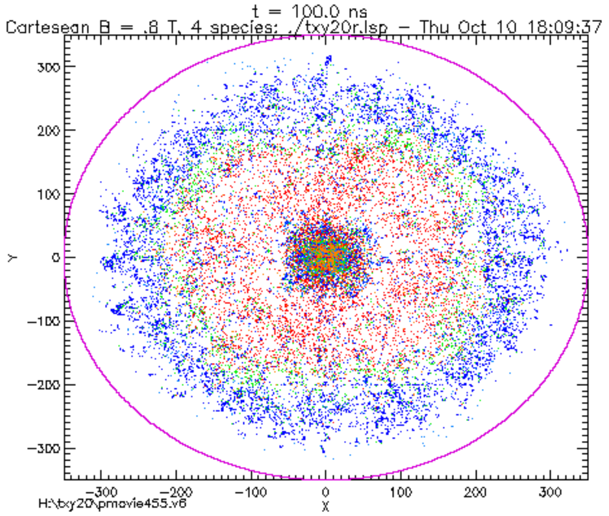

Fig. 2.2.1.2 The direct-drive target ions expand into a 0.8 T uniform magnetic field.

At a time of 100 ns, the plasma has expanded to approximately 3 m. Eventually, one would expect to see the expansion go to 3.6-4.7 m, depending upon whether or not the first wall is a flux-conserving surface. The simulation was stopped at ~130 ns for two reasons: (1) a significant portion of the plasma had expanded beyond the problem domain, and (2) LSP is not conserving energy. Figure 2.2.1.3 demonstrates the latter point. It is believed that the lack of energy conservation is due to a numerical problem with the implicit solver. Our colleagues at MRC are investigating this matter. Also, MRC has provided us with a new version of LSP that treats all species as a fluid. We are studying the regimes under which this is a reasonable approximation.

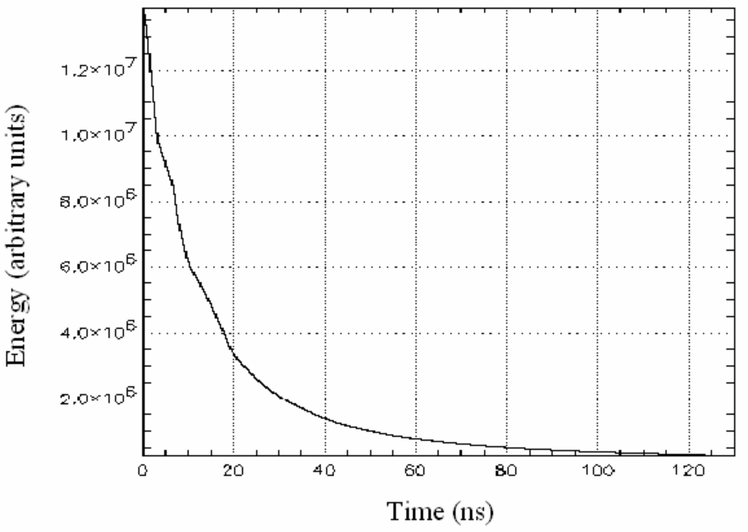

Fig. 2.2.1.3 As the plasma expands, it rapidly looses energy due to a numerical problem in LSP.

Currently, LSP is quite unstable for the plasma parameters present shortly after ignition of a target within an IFE chamber. The plasma is initially quite dense and hot. It expands into a vacuum, a low density of gas, or even a low-density plasma, which is in a large chamber (~6.5 m in radius). Simulation of the hot, dense plasma requires small cell sizes, many particles and small time steps. The relatively large confinement chamber requires many cells to simulate the plasma expansion. An additional difficulty is that the plasma is composed of many ion species with each species having a wide range of initial energies. Finally, the electrons can become quite hot and require a kinetic treatment, resulting in a drastically smaller cell size and time step.

The above complications have significantly hindered our progress. We had hoped to model at least one complete IFE-scale plasma expansion during the past year. However, this problem has proven to be more numerically challenging than previously anticipated. LSP has not yet successfully simulated a full IFE plasma expansion. Although LSP is a fully 3D code, we do not, at the present time, have access to a sufficiently large and fast computer to perform such calculations. We have scaled back our analysis to a series of 2D (radial and axial) expansion calculations. We have found that the transition of electrons from a fluid description to a kinetic one causes LSP to become unstable. After unsuccessfully using various transition models, we have found that treating the electrons as purely fluid greatly increases the robustness of the code. It is not yet clear whether or not this is a valid assumption.

Since the target plasma is initially at very high density and temperature, and thus, a very high value of beta, there is little reason to follow the early time history of the expanding plasma. It does not feel the influence of the external magnetic field until beta of order unity is reached. To understand the implications of this, a “concentric shells” model was developed. The model visually demonstrates the time-of-flight expansion of the various particles and energies. This simplified the process of determining the point at which—after some initial free expansion—the calculation should begin. By starting the calculations at a later time and density, we have been able to reduce the computing time needed for our simulations.

In addition to our computational work, we have interpreted experimental data that was collected on the Large Plasma Device Upgrade (LAPDU) at the University of California at Los Angeles. LAPDU, shown in Figure 2.2.1.4, is a jointly funded (NSF and DOE) user facility for the study of plasma phenomena [5]. This facility can produce a completely ionized plasma ~0.75 cm diameter and 16 m in length. The plasma lifetime is ~10 ms with density fluctuations less than 3%. The plasma is created using solid Al, C, or Ba targets and a 1.5 J Nd-YAG laser operating at 1.06 µm. Approximately 0.75 J of laser power is directly coupled into the target plasma. The laser spot size of 0.5 mm diameter results in a laser power deposition of ~10^{11}W/cm^2. Typically experiments operate at 0.5–1 Hz. Since thousands of shots are taken per data plane, the target rod is rotated and translated between shots to keep the surface “fresh”.

Fig. 2.2.1.4 LAPDU is ~0.75 m in diameter and 16 m in length.

Previous experiments on the LAPDU facility have collected data of interest to our work. According to ref. 1, a plasma will expand until it reaches the β=1 surface. This bubble radius, R_b, in MKS units, is given by:

$$R_b = (3E\mu_0/2\pi B^2)^{1/3}$$

where:

E is the plasma energy,
μ_0 is the magnetic permeability of free space, and
B is the magnetic field.

Figure 2.2.1.5 shows data collected during previous experiments on the LAPDU facility [7]. These experiments appear to validate the 1D plasma bubble equation. Although agreement is quite good, this work needs to be extended to higher fields and background plasma densities. Also, we are interested in the axial transport and 2D effects, such as fingering.

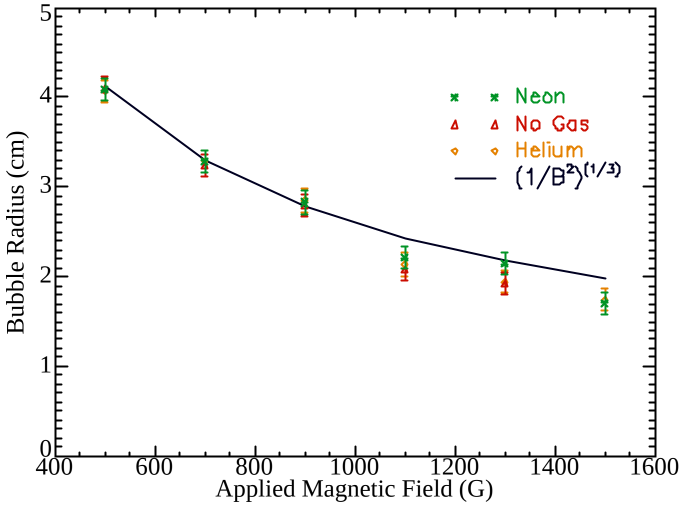

Fig. 2.2.1.5 Experimental results on LAPDU appear to validate the 1D plasma bubble equation given in ref. 1. Experiments conducted with a background plasma density of 10^{12} cm^{-3} do not appear to significantly deviate from the vacuum prediction.

In summary, we have made progress on the development of a magnetically protection variation of the SOMBRERO design. There is, however, considerable work remaining to be done. The LSP code has been installed and is operational. We have calculated the time-of-flight spread of the fast and debris ions using an expanding shell model. John Perkins has used the LASNEX code to provide us with chamber wall ion fluxes, including attenuation through 10 mTorr of xenon gas. Unfortunately, for the problems we are trying to solve, the LSP code is both unstable and computationally expensive. This combination has hindered our progress, and has limited our progress in analyzing point designs. A preliminary shielding design has been developed, which would provide an adequate lifetime for the superconducting magnets. Finite element modeling has been used to develop the coil designs for the uniform field case. The effect that the expanding plasma has upon the background magnetic field has been included in our analyses. Due to the slower than anticipated progress and the difficulty in performing computations that are stable and timely, we are opting to discontinue this effort. The FY03 effort will be limited to the production of a detailed summary of our progress and lessons learned.

References

[1] Yu. P. Raizer, “Retardation and energy transformations of plasma expanding in an empty space containing a magnetic field,” Zh. Prikl. Mekh. Tekh. Fiz., No. 6, 19-28 (1963).
[2] S.A. Nikitin and A.G. Ponomarenko, “Dynamics and spatial boundaries of retardation of the plasma cloud of an explosion in a dipole field,” J. Appl. Mech. & Tech. Phys., 34, 745 (1993).
[3] Yu. P. Zakharov, A.M. Oriahich, A.G. Ponomarenko and V.G. Posukh, “Effectivness of the slowing of expanding clouds of diamagnetic plasma by a magnetic field (experimental),” Sov. J. Plasma Phys. 12(10) 674-678 (Oct. 1986).
[4] Guy Dimonte and L.G. Wiley, “Dynamics of exploding plasma in a magnetic field,” Phys. Rev. Let., 67, 1755 (1991).
[5] W. Gekelman, H. Pfister, Z. Lucky, et al, “Design, construction, and properties of the large plasma research device – The LAPD at UCLA”, Rev. Sci. Instrum. 62(12), 1991 p. 2875.
[6] B. H. Ripin, E. A. McLean, C. K. Manka, et al, “Large-Larmor-Radius Interchange Instability”, Phs. Rev. Let. 59(20), 1987 p. 2299.
[7] M. VanZeeland, W. Gekelman, S. Vincena, and G. Dimonte
, “Expansion of a laser-produced plasma embedded in an ambient magnetic background plasma,” 44th Annual Meeting of the APS Division of Plasma Physics, Orlando, FL, (Nov. 2002).

2.2.2 Fast Ignition

In FY02 we have continued addressing the key development issues for a laser IFE power plant using fast ignition (FI). The FY02 tasks in this area were:

- Continue literature review on the subject.
- Obtain best estimate of DT ice surface roughness that can be tolerated.
- Consult with General Atomics on target fabrication issues.
- Assess the laser pointing and timing requirements and the implications for target injection, tracking and beam steering.
- Evaluate of potential for directional target output.
- Address optics protection schemes for ignitor laser.
- Complete basic beam and chamber layout.

As a starting point, we performed a detailed literature search. This search included the most recent conferences featuring papers on the subject, such as IFSA2001 and the 5th Workshop on Fast Ignition of Fusion Targets in Madeira, 2001. This initial evaluation pointed out several technology areas requiring a specific development path in the case of a power plant using FI, including target fabrication, injection and tracking, ignitor laser propagation, focusing and timing, and size, location, and protection of final optics for the ignitor beams.

In the area of target roughness, we have revisited work from target designers at LLNL for tolerable surface finish for IFE targets. Recent studies have shown that high yield targets may be less unstable than low yield ones and may be less susceptible to surface perturbations fed-out from initial ice roughness. Calculations should be benchmarked with ignition experiments to choose final fabrication specifications.

We have consulted with target fabrication experts on FI specific issues and opportunities. Ongoing work at general Atomics is investigating the possibility to stamp hard-frozen DT hemispheres and "weld" them together. If this approach succeeds, the DT fuel could serve as ablator so no capsule or overcoat would be needed. This could significantly reduce T inventory in target factory due to fast fuel layer formation (eliminates diffusion fill step). Also, if hard frozen DT can be used, heating during injection is less of an issue. Particularly, in the case of the cone-focused target design, injecting the target cone first could reduce effects of chamber gas on the DT fuel. Finally, it has been found that since a generic FI target weighs substantially more than a direct drive target, it would be less affected by residual atmosphere and contact forces and should be somewhat easier to reproducibly deliver it to the target chamber center.

Regarding target tracking and timing precision, this should be similar to hot-spot ignition for compression beams. The ignitor beams should be triggered off of the compression beams with a fixed delay. Also, one should be able to use movable mirrors at the low power end of system for pointing of the ignitor beams, similarly to the technique used for pointing the compression beams. Propagation of the ignitor beams through the chamber environment is another critical issue. Propagation through chamber gas is more difficult for high-intensity ignitor beams as laser-plasma interactions lead to a highly non-linear index of refraction, which could "steer" beams away from the ignition spot. Therefore, the chamber background gas density could be limited to a value lower than that allowed for the compression beams. Measurements of the interaction of high power density beams with background gas are needed to resolve these issues.

Most of the work during FY02, was devoted to the last three bullets listed at the beginning of this section. These tasks are related to the layout and survivability of the final optics system for the ignitor beam. Fast ignition targets require that the ignitor energy be delivered into a spot on the order of ~30 µm, thus requiring precise pointing and focusing of the beams or some mechanism of channeling the laser energy to the final spot size. Due to the likely directionality of debris emission from the cone focused target design, final optics survivability for ignitor beams is a critical issue for the development of an attractive FI power plant design. Projections for a future ignitor laser using a DPSSL technology scaled from that of the Mercury laser estimate a maximum of 2-4 kJ per beam. This means that 25-50 beams would be required for a total of ignitor beam energy of 100 kJ. The number of optics would be reduced by a factor of two if two polarizations per final optic is used.

We have used a systems code to study the number of ignitor beams that would be required as a function of their size, location, and spot size requirements. For optics that are 2× diffraction-limited and a spot size of 33 µm, even 1-m-diameter optics result in an optic stand-off distance of only ~13 m. At such a short distance, the optics will be in an extremely harsh environment (neutrons, gamma-rays, x-rays, ions, and debris), and multiple protection techniques are likely to be needed. In particular, for the cone focused FI target, debris may be directed back at the ignitor beam final optics. Development of large-diameter diffractive optical components that are "robust" is needed. There is also a need to pursue techniques for optics protection.

Also, chirped pulse amplification (CPA) lasers use diffraction gratings to recompress the beams to extremely high power (>10^{15} W). Optical elements after the gratings in the final optics package will be quite vulnerable to damage from such high power beams. The number of final optics required will depend upon size, fluence damage limit, and beam coupling efficiency, as seen in Figure 2.2.2.1. If the area of the ignitor beams is too large due to a low optical damage limit, they would subtend an unacceptably large solid-angle fraction.

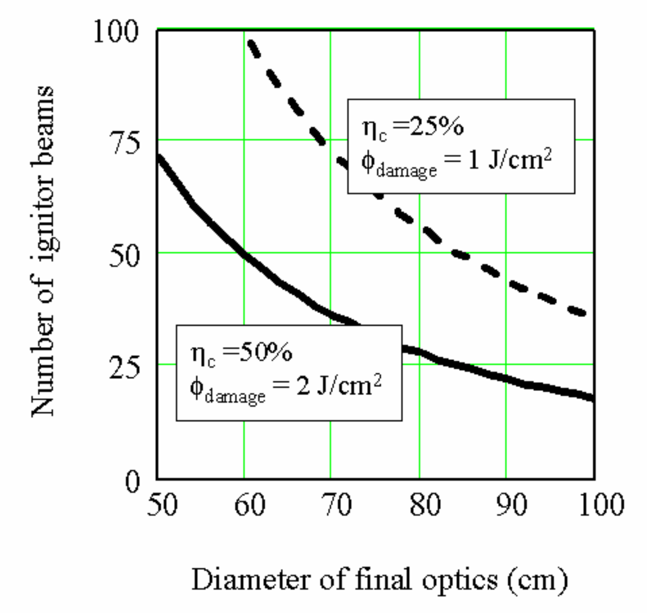

Fig. 2.2.2.1 The required number of ignitor beams varies as a function of coupling efficiency and laser damage limit. A total ignitor energy of 40 kJ has been assumed.

We have performed a preliminary assessment of the different options for the ignitor laser final optics. Conventional available metallic gratings do not have sufficient laser damage threshold for use in FI. Multi-layer dielectric gratings are currently being designed and tested for FI requirements. Simultaneously, large, thin transmissive Fresnel lenses are being developed for the Eyeglass project (LLNL) and are also being evaluated for FI. Fresnel lenses have been already fabricated in 80-cm diameter, 1-mm thick fused silica substrate using 2-mask lithography and HF etching. Expectations are that monolithic 80-cm diameter, 1 mm thick fused silica Fresnel lenses can also be fabricated using the same technology. However, there are still issues that need to be addressed regarding the use of Fresnel lenses with such short pulses. Temporal blurring of a Fresnel lens may be incompatible with the ignitor pulse of a few ps in length. This is due to the fact that a Fresnel lens focuses the beam spatially, but the pulses are "defocused" in time as a result of uncompensated transit time differences for different radial components of the beam after the lens. It has been shown that for a 40-cm beam, it is impractical to use Fresnel lens to focus pulses shorter than ~10 ps. However, in applications that require pulse lengths longer than 10 ps, it may be advantageous to use Fresnel lens to simplify the final focusing arrangement. Currently envisioned FI-IFE beams would be ~20 ps.

The work on the FI task during the past year produced a journal paper and two presentations, which may be consulted for further information:

1) S. Reyes, R. C. Schmitt, J. F. Latkowski, J. Sanz, "Liquid Wall Options for Tritium-Lean Fast Ignition Inertial Fusion Energy Power Plants," *Fusion Eng. Des.* **63-4** (Dec. 2002) 635-640.

2) S. Reyes, W. R. Meier, J. F. Latkowski, "Update on Fast Ignition Laser IFE Activities," presented at the HAPL Program Meeting, San Diego, April 4-5, 2002.

3) W. J. Hogan, "Technology Developments Needed for an IFE Power Plant Using Fast Ignition," presented at Institute for Laser Engineering, Osaka University, Japan, March 5, 2002.

This modest effort to consider many of the integration issues associated with fast ignition has been quite fruitful. Due to priorities within the High-Average Power Laser (HAPL) Program and the fact that fast ignition enjoys support outside of HAPL, this work will not be continued in FY03.

2.2.3 Safety and Environment

During FY02 we continued providing safety and environmental support to the overall HAPL Program (including the Materials Working Group) as well as to the LLNL effort in Chamber Studies. Our tasks for FY2002 included:

- Provide neutron and gamma-ray transport and activation calculations for the magnetically-protected chamber design.
- Provide neutron/gamma-ray transport and activation calculations for a direct conversion system or ion dump.
- Provide the overall program, including the Materials Working Group with safety and environmental (S&E) support.

Neutron and gamma-ray transport calculations were completed for the uniform field version of the magnetically protection chamber. Calculations indicated that it should be possible to provide adequate protection for the large superconducting magnets. Neither the radiation-damage-limited lifetime nor the recirculating power for cooling the coils to liquid helium temperatures should pose a serious feasibility problem.

Due to the slow progress in the plasma expansion modeling, we have not begun the design of an ion dump. This work will be completed once information regarding the ion output spectra and exit hole size become available.

We have continued to work on target materials in order to provide designers with appropriate guidance from the S&E point of view. Safety issues do not only consider radioactivity hazards but also chemical toxicity issues of some candidate target materials. Also, we continued addressing different options for waste disposal of IFE power plant components, emphasizing the benefit of clearance and/or recycling of materials versus the traditional shallow land burial disposal.

In collaboration with the Fusion Safety Group in INEEL, we have identified accident Initiating Events (IEs) for Probabilistic Risk Assessment of the SOMBRERO laser IFE power plant design. In order to determine the risks posed to members of the public in the vicinity of a power plant one must identify and analyze each one of the possible IEs. A set of accident IEs creates a basic framework of types of events to consider in future risk characterization of new plant designs. A variety of IE identification techniques are available for use on completed designs, but only some of these techniques apply to conceptual designs. The ongoing work SOMBRERO uses all applicable techniques: preliminary hazard analysis, review of operating experiences from other facilities, review of past safety analyses applicable to the IFE designs and master logic diagrams.

The latest developments on laser IFE S&E during the past year were presented at the last IAEA Technical Meeting on Physics and Technology of Inertial Fusion Energy Targets and Chambers [1]. Also, an invited talk on the safety and environmental aspects of IFE was given at the American Nuclear Society's Fifteenth Topical Meeting on the Technology of Fusion Energy [2].

References

[1] S. Reyes, J. F. Latkowski, L. C. Cadwallader, "Safety and Environmental Aspects of Inertial Fusion Energy: An Overview of Recent Activities and Developments in the US," IAEA Technical Meeting on Physics and Technology of Inertial Fusion Energy Targets and Chambers, San Diego, June 17-19, 2002.)
[2] J. F. Latkowski et al., "Status of Safety and Environmental Activities for Inertial Fusion Energy," Invited talk at the 15th Topical Meeting on the Technology of Fusion Energy, Nov. 17-21, 2002, Washington, DC. To appear in *Fusion Sci. Technol.*

2.2.4 Radiation Damage Modeling for Chamber Materials

During the FY02, we have demonstrated proof of principles studies of using molecular dynamics (MD) simulations to understand the effects of neutron and ion irradiation on bulk graphite and graphitic materials. FY02 tasks include:

- Calculate activation energies for hydrogen and tritium transport and detrapping in graphite.
- Calculate migration and binding energies of hydrogen with vacant sites, single vacancies, and vacancy clusters.
- Compare calculated values to experimental measurements.
- Perform ab initio calculations for single defects.
- Calculate threshold displacement energies for graphite.
- Estimate the total number of defects produced.

Graphitic materials are particularly challenging to model. Due to the required use of Brenner hydrocarbon potentials, graphitic simulations require 10-15× more computing power than those previously completed for metals.

We performed cascade simulations in graphite using 1-2 keV primary knock-on atoms. From these detailed atomistic simulations we were able to identify several different types of defects in graphite. Interstitials atoms are those defined as lying between graphitic planes, and are important factors in encouraging dimensional changes and swelling in graphite. Additionally, we observed a large number of two- and four-fold coordinated carbon.

Simulations with 1 keV and 2 keV recoils in graphite show similar cascade structures to those observed in metals. Figure 2.2.4.1 shows the cascade structures produced by 1- and 2 keV recoils in a graphite lattice 5 nm by 5 nm wide along the basal plane directions, and 11 nm long along the transverse direction.

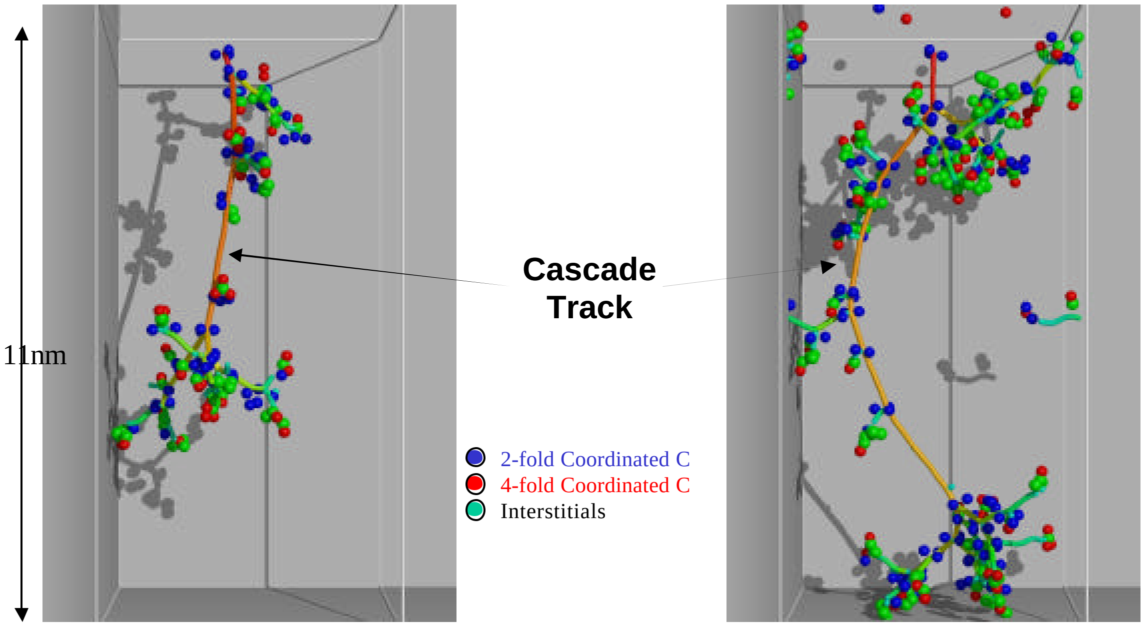

Fig. 2.2.4.1 The cascade track and defects produced by 1- and 2 keV recoils in graphite.

We have not been able to observe defect nucleation and interstitial and vacancy platelet evolution in the MD simulations due to the short timescales involved (picoseconds) and the computationally intensive nature of the Brenner potentials. Figure 2.2.4.2 shows the temporal evolution of the defects formed from a 1 keV recoil in graphite. The most striking observation is the absence of a rapid falloff in the number of defects due to localized defect recombination. In previous calculations (for other materials), a rapid decrease in the defect concentration has been observed. This suggests that other modeling techniques such as kinetic Monte Carlo must be applied to understand the much longer time-scale behavior of the defects.

Finally, we have developed and implemented a non-lattice kinetic Monte Carlo code that will be used to model the interaction of defects with point and extended defects such as dislocations, platelets and grain boundaries.

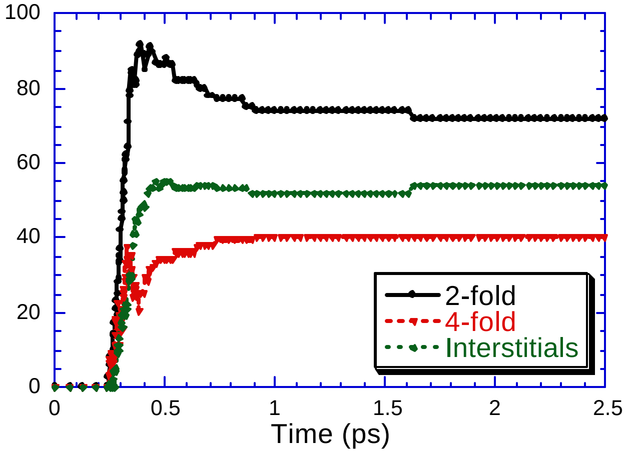

Fig. 2.2.4.2 The time-evolution of the number of defects formed in a 1 keV recoil in graphite.

2.2.5 Systems Modeling

Our FY2002 task was:

- Update and improve DPSSL model, which dates to 1994. For example, include beam smoothing, improve extraction model, and consider different architectures.

The diode-pumped solid-state laser (DPSSL) systems code, created by Orth, has been updated during FY02. The systems code was re-written (utilizing modern, best practices programming rules), modularized, and translated into Fortran 90. The resulting source code is significantly shorter and much easier to understand. The updated code was tested with a set of benchmark problems and verifying that the new results agree with the old ones. In addition, a new nonlinear optimization package was added. Unfortunately, we have been unable to utilize this feature due to remaining programming logic difficulties in the subroutines. In its current state, the code fails when moving to points off the benchmark case Additional effort will be required before the DPSSL systems code is in a condition where individual physics modules can be updated to include the latest models and experimental data.

2.3 Final Optic

The most fundamental threat experienced by the final optic in inertial fusion energy is that imposed by the neutrons and gamma rays, since MeV ionizing radiation cannot be blocked without impeding the laser light itself. These threats are also important in NIF, although much less severe because of its lower repetition rate.

2.3.1 Gamma and Neutron Irradiation Studies

Our FY02 tasks were:

- Complete the analysis and write a detailed journal article on the deployment of a SiO_2 final optic.
- Complete the irradiation studies of the Al_2O_3 and MgF_2 transmissive optics, and the 3ω, 4ω and aluminum mirrors.

During FY02, we completed our assessment of the 0.35 μm (3ω) SiO_2 final optic. The crucial issues have been addressed: defect formation and saturation, radiation-hardness, cooling, and fabrication. The suggested deployment is to use a *thin* (< 0.5 mm) diffractive optic to minimize the defect-induced absorption, which both focuses and deflects the 0.35 μm beam. An extensive peer-reviewed journal article has been completed on this topic [J. F. Latkowski, A. Kubota, M. J. Caturla, S. N. Dixit, J. A. Speth, and S. A. Payne, "Fused Silica Final Optics for Inertial Fusion Energy: Radiation Studies and System-Level Analysis", to appear in *Fusion Science. and Technology*, June 2003], which includes a systems study of the predicted performance of the optic in an IFE power plant, as well experimental and kinetic analyses of the radiation-induced defects. We have modeled the final optic as an off-axis Fresnel lens that provides for both focusing and deflection of the beam. In Figure 2.3.1.1 below, we plot the impact of the temperature of the final optic from 300 °C to 600 °C, where it is seen that at higher temperature the residual laser absorption at 3ω can be reduced to a negligible level (corresponding to 20 m stand-off for a 1 GW_e plant).

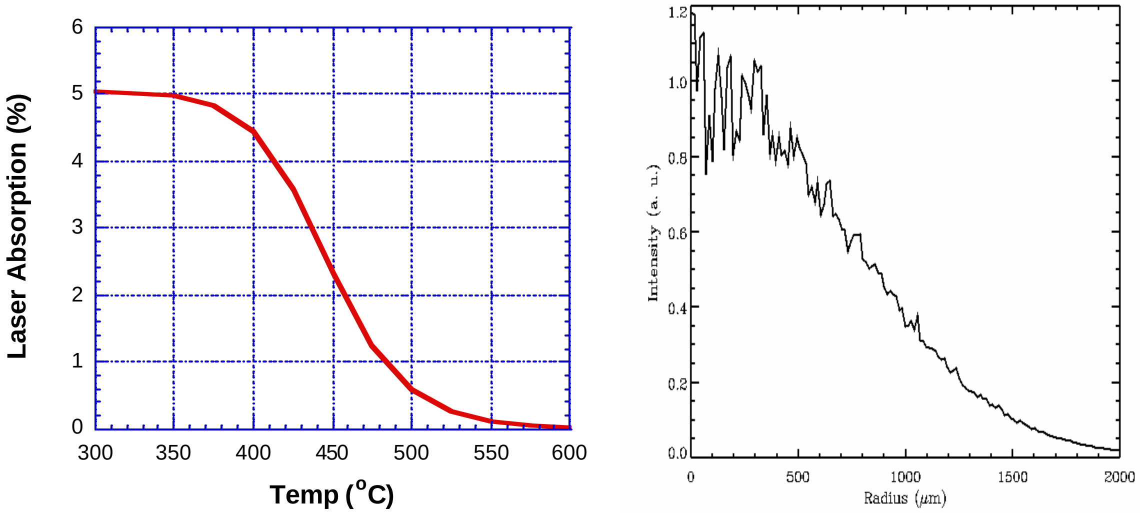

Fig. 2.3.1.1 LHS: Increasing the steady-state temperature of a fused silica final optic anneals away structural defects, and the laser absorption at 3ω can be reduced to a negligible level. RHS: The spot size on target has been calculated for a Fresnel lens with phase plate at 20 m.

The 3ω defect absorption was quantitatively explained in terms of the formation of E' centers, which saturate when the collisional cascades begin to overlap, and can be annealed away at elevated temperature. Also, in Figure 2.3.1.1 is the calculated shape of the focal spot, based on the Fresnel lens and a phase plate. The result is that the chromatic effects of the Fresnel lens have little impact on the target spot size, (which can easily be enlarged or reshaped if required for the target).

We have studied several optical materials that are potential alternatives to fused silica, and have determined that SiO_2 is the best choice for operation at 3ω. The spectra of these alternatives are pictured in Figure 2.3.1.2, where they all incurred a 1.0 Mrad neutron dose and 8.7 Mrad of γ-rays. The CaF_2, MgF_2, and Al_2O_3 samples were all selected for their high purity, implying that the features observed in Figure 2.3.1.2 are all "intrinsic" to the material (i.e. due to color centers).

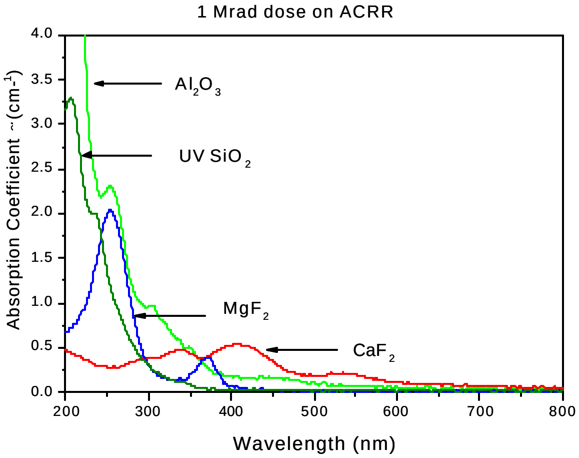

Fig. 2.3.1.2 Absorption spectra of several candidate optical materials suggesting that SiO_2 is the preferred material at this time.

We are in the process of having dielectric mirrors neutron-irradiated at Oak Ridge National Laboratory (ORNL). To perform these tests we needed to first obtain and verify that the specialty mirrors did not have any hafnia or tantala present (as is usually the case) since they present serious problems with activation, as is presented below in Figure 2.3.1.3. These samples have been cut and sent to ORNL several months ago, and are waiting for time in the HFER reactor. Preliminary results from 100 Mrad exposures by γ-rays alone indicate that the reflectivity change is small.

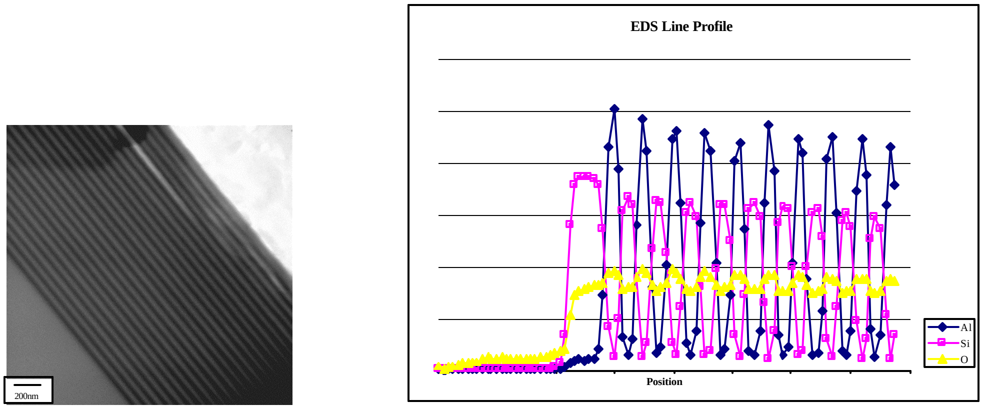

Fig. 2.3.1.3 TEM micrograph (LHS) and elemental analysis (RHS) of specialty mirrors produced by CVI Corporation, assuring that the 3ω and 4ω mirrors are comprised of SiO_2 and Al_2O_3 amorphous layers. No hafnia or tantala (i.e. most common constituents) were introduced due to issues associated with activation.

2.3.2 Molecular Dynamics Simulations of Neutron-Induced Defects

In the area of molecular dynamics simulations (MDS) for final optic materials, there were two tasks for FY02:

- Completed MDS evaluations for fused silica.
- Begin MDS evaluation of neutron-induced damage of reflective optics.

During FY02 we have completed our studies of radiation damage in SiO_2 glasses. We have performed simulations with recoil energies between 1 and 5 keV, obtained the total number of Oxygen Deficient Centers (ODC) produced by the irradiation and compared with experimental measurements of optical absorption. We have performed simulations of damage accumulation to understand the effect of defect saturation observed experimentally. Figure 2.3.2.1 shows the number of ODCs produced as a function of time for cascades that begin from the same point in the lattice (overlapping). This figure shows how after only a few overlapping cascades (five in this case) the total number of ODCs does not increase and the total damage saturates. This is the result of a recombination between the pre-existing damage and the damage produced by the following cascade during irradiation.

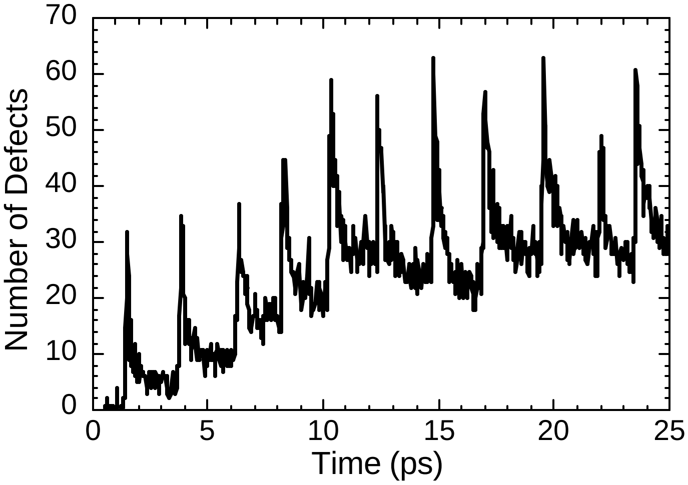

Fig. 2.3.2.1 The number of 3-fold coordinated Si atoms versus time, over eleven successive and overlapping 1 keV recoils. Each sharp peak roughly corresponds to a single recoil. Saturation behavior is observed after about 5 overlaps.

Additionally, we investigated the topological and structural changes in silica irradiated by successive overlaps of the energetic recoil atoms. We found that overlap regions (regions exposed to the energetic cascade) showed substantial changes in topology, namely an increase in the number of smaller (2,3 and 4-membered) rings. We found saturation to occur after five cascade overlaps. These topological changes have been observed in fused silica damaged and densified through various mechanisms, such as under ion, electron, and neutron radiation and under static and dynamic high-pressure conditions. The permanent densification has always been associated with topological changes observed through Raman spectroscopy. However, this work demonstrates that topological changes in fused silica can occur under prompt and short-time-scale conditions during collision cascades. Also, we speculate that the saturation in the topological changes may be related to the defect saturation, but we do not provide any concrete evidence.

This work has resulted in the following publications, which were submitted during FY02:

1) Kubota, M. J. Caturla, S. A. Payne, T. Diaz de la Rubia, J. F. Latkowski, “Modeling defect production in silica glass due to energetic recoils using molecular dynamics simulations,” accepted for publication in *J. Nucl. Mater.*

2) Kubota, M. J. Caturla, J. F. Latkowski, S. Reyes, T. Diaz de la Rubia and S. A. Payne, “Modeling Neutron Irradiation Induced Modifications in Fused Silica”, accepted for publication in Nuclear Instruments and Methods B.

3) Kubota, M. J. Caturla, J. Stolken, B. Sadigh, S. Reyes, T. Diaz de la Rubia and J. F. Latkowski, “Threats to ICF Reactor Materials: Computational Simulations of Radiation Damage Induced Topological Changes in Fused Silica,” Proceedings of the Sixth International Conference in Computer Simulations of Radiation Effects in Solids, Dresden, Germany, June 23-27, 2002, to appear in Nuclear Instruments and Methods B.

Finally, during FY02 we initiated study of radiation-induced surface roughening of aluminum mirrors. A kinetic Monte Carlo model can be used to study the diffusion of those defects produced in the bulk of the material due to neutron irradiation. We have modified our kinetic Monte Carlo code to account for those defects that diffuse to the surface. With this modified code a 2D profile of the number of defects accumulated at the surface can be obtained. This model can be used to estimate the stresses building up underneath the surface oxide layer due to radiation damage and that could result in buckling or roughening of the surface.

2.3.3 X-Ray Ablation of Optical Materials

FY02 tasks for x-ray damage studies include:

- Form a steering committee to assist in setting of program priorities.
- Develop a detailed experimental plan.
- Procure, install, and operate a rep-rated x-ray irradiation facility.
- Equip facility with a suite of diagnostics.
- Upgrade ABLATOR code.
- Characterize x-ray output.
- Complete an experimental campaign, including irradiations and analysis, for two leading materials.

The overall objective in this task is to develop and experimentally benchmark a predictive capability, which can be used to analyze x-ray damage and/or ablation of optical and chamber wall materials. While one can design components to avert single-shot melting and/or vaporization, little data are available for many-shot exposures at sub-threshold fluences. Similarly, only limited knowledge exists on the effects that impurities, surface contamination, rough surfaces, and neutron/gamma-ray irradiation have upon x-ray ablation. Through use of the X-Ray Ablation using Plasma Pinch in the EUV Region (XAPPER) facility, we will continue to build and validate our predictive capabilities.

A steering committee was formed, made up of members of the HAPL community. The committee was consulted in setting priorities for irradiation campaigns and in selecting the particular materials of interest. The committee also has been helpful in providing advice for real-time diagnostics, which will be fielded on the experiment.

An experimental plan was developed during the time leading up to procurement. The use of a laser-based plasma source was considered, but it was dismissed based upon development needs and concerns over the ability to provide adequate fluence on the samples and a relevant number of pulses per year (system availability). A decision was made to procure a star pinch based source from PLEX LLC. An ellipsoidal condensing optic is used to collect soft x-rays and bring them to focus at the sample plane.

The major accomplishment for this fiscal year is the procurement and installation of the XAPPER source. The PLEX source is capable of delivering IFE-relevant doses to materials of interest. While XAPPER produces only soft x-rays, the mean free path of these x-rays is short, and thus, more energy can be deposited per unit mass than would be the case in an actual IFE system. Figure 2.3.3.1 shows XAPPER as currently installed at LLNL. The soft x-ray spectrometer will be delivered before the end of the calendar year. It will be installed in a vertical orientation as shown in Figure 2.3.3.2.

Due to delays in funding, the procurement process, and the prime contractor, the XAPPER source was not delivered until October 2002. Full system installation was completed in November. System characterization and optimization is still underway. Preliminary results indicate that the source is performing as expected. The ellipsoidal condensing optic, however, does not appear to meet specifications. In particular, it appears that the optic is failing to bring the soft x-rays to a tight focus of ~2 mm. Instead, we have measured a spot size of nearly 15-20 mm. As a result, the peak fluence is down by more than 40-50× relative to what was expected.

Our current understanding is that the optic contains a mid-frequency spatial roughness (micron-level roughness with a centimeter wavelength superimposed upon the expected 2 nm RMS, which was specified by the prime contractor), which leads to a flare in the image. Two solutions are being pursued in parallel. First, the subcontractor has been tasked with producing a replacement optic. Second, PLEX LLC is attempting to purchase a replacement optic from another company. Independently, LLNL has undertaken energy and spot size measurements, and we will soon perform a direct source measurement to ensure that the problem really is with the optic, rather than the source. Finally, we have met with local experts in EUV optics and we believe that an optic could be produced in-house, at additional expense, if necessary.

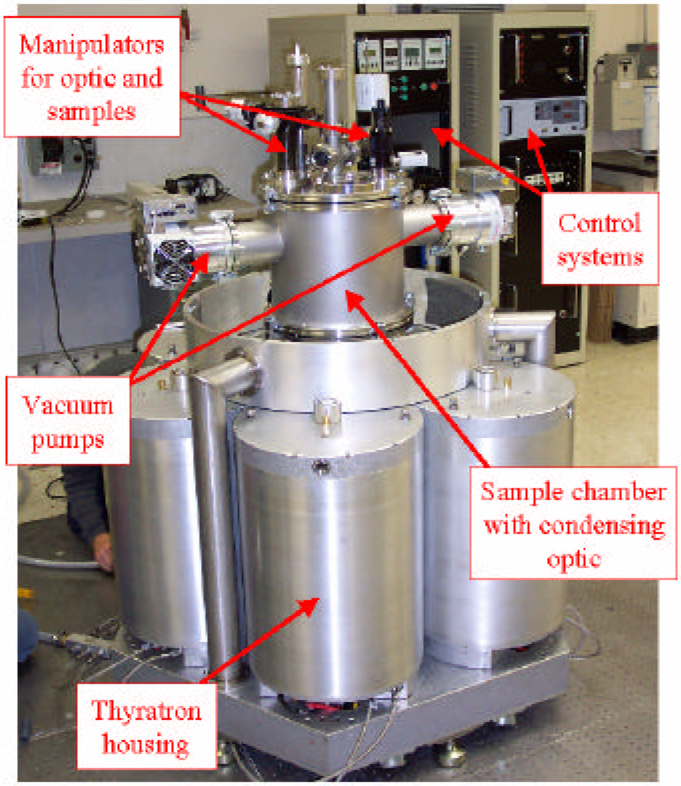

Fig. 2.3.3.1 The XAPPER source has been installed at LLNL. Source testing is underway, and sample exposures are expected to begin in November.

During FY02, the ABLATOR code was modified in order to simulate x-ray heating of chamber wall and final optic materials, when exposed to either the IFE x-ray spectrum or that from the XAPPER experiment. We have introduced various usability improvements. Some of the more significant code modifications are:

- Implemented various techniques to improve numerical stability
- Introduced direct-drive target spectra for the bare target, as well as the escape spectrum after 6.5 Torr-cm of xenon gas
- Introduced ability to attenuate IFE x-ray spectra out to distances of more than 6.5 m
- Added restart capability (read in temperature/enthalpy profile)
- Modified to allow user input of initial temperature
- Added tungsten to materials database
- Debugged/tested grazing incidence module
- Collaborated with UCSD to add flibe to the materials database
- Introduced indirect drive target spectra

Fig. 2.3.3.2 X-rays are collected with an ellipsoidal condensing optic and directed vertically upwards towards the target. When the target is rotated out of view, the soft x-ray spectrometer has a direct view of the plasma.

Using the new restart capability, one can simulate the heating of a material resulting from the series of photon pulses that are experienced during power plant operation. Figure 2.3.3.3, for example, shows the time-temperature history of a grazing incidence aluminum final optic. The figure was generated assuming a 30 m stand-off distance, an 85° angle of incidence, a 30 ns laser pulse delivering a fluence of 2 J/cm^2 to the final optic, and a reflectivity of 99%. The prompt x-ray pulse has a 1 ns pulse length and a total energy of 6.1 MJ. An LLNL calculation shows that a longer, secondary pulse occurs when soft x-rays are emitted as the debris ions stop in 10 mTorr of Xe gas in the chamber and beam line. While this pulse is nearly 1 µs in duration, it delivers over 45 MJ of total energy. Whether or not such large fluxes of soft x-rays will actually be produced due to ion stopping is an active area of debate among the target physicists in the HAPL Program. Similar temperature histories have been generated for the chamber wall materials, as well as for a fused silica transmissive optic.

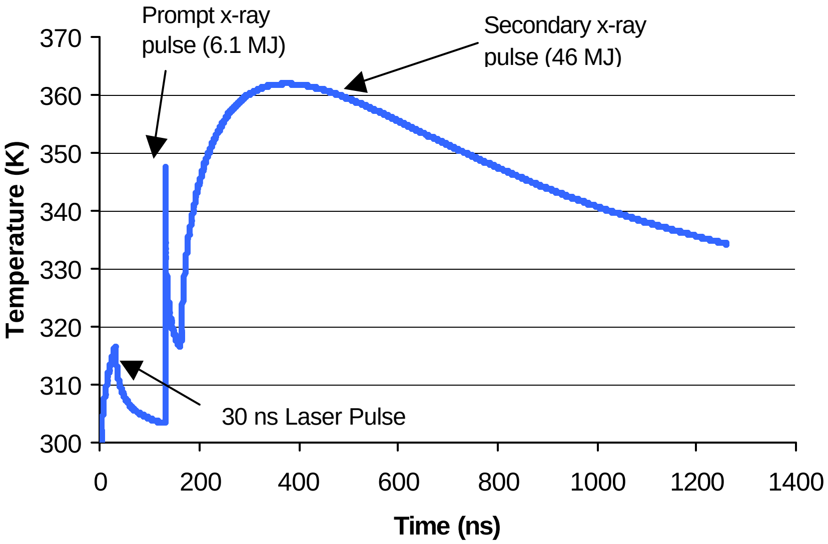

Fig. 2.3.3.3 An aluminum final optic experiences multiple temperature transients for each fusion pulse.

2.4 Target Physics

Our FY2002 tasks were:

- Perform calculations for direct-drive targets employing thin films to reduce imprint, and evaluate the wavelength dependence and "threat spectra." Continue assessing the impact of 2D hydrodynamic instabilities.

Introduction

Direct-drive target designs for the HAPL program employ 2D and 3D radiation-hydrodynamic-burn codes that are under development for the Stockpile Stewardship Program. Our work in 2001-2002 has encompassed (a) 1-D analyses to optimize target yields and gains, (b) the production of output "threat" spectra (radiation, particles and debris) to gauge wall interactions and, in particular, (c) 2-D studies to determine the symmetry and stability of such targets from initial laser interaction through full compression and burn. These IFE target calculations are excellent test beds for the capabilities of our ASCI codes. They contribute directly to the validation of such codes for high energy density physics applications, while exploring the spin-off application to inertial fusion energy.

1-D Studies

Fig. 2.4.1 shows the high yield, direct drive target presently under study in collaboration with NRL. It comprises a cryogenic DT fuel layer and a mainly DT ablator– i.e., DT fueled wicked into low density CH foam – surrounded by a 5.8 µm solid CH shell. A variant of this target is also under consideration – variant B in Fig. 2.4.1 – in which an additional thin, 1000A outer shell of palladium is added to reduce early-time laser imprint; preliminary results indicate that this shell also reduces Rayleigh-Taylor growth through radiation heating of the ablator.

The figure also summarizes the LASNEX performance of this target, namely 1-D yields in excess of 400 MJ, gains of ~170, and requiring laser drive energies of ~2.4 MJ. These results agree well with the independent calculations of NRL. We propose that increasing drive energies may be required for stability reasons; however, we are confident that gains in excess of 100 may be realizable for these target designs.

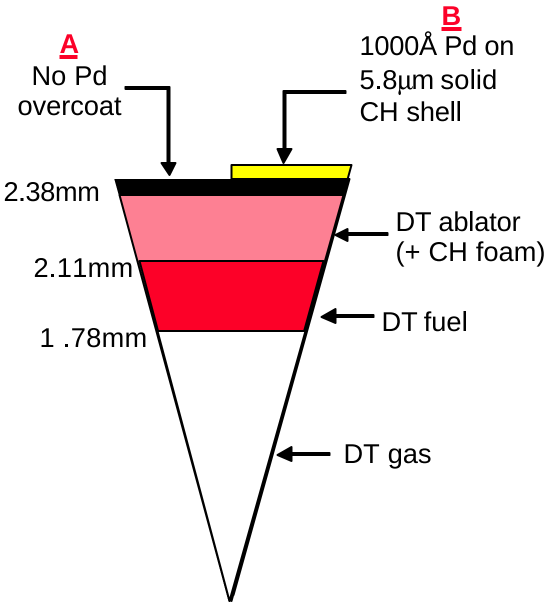

NOMINAL 1-D PERFORMANCE

• Yield	420 MJ
• Gain	170
• E_{laser}	2.4MJ
• Max ρR	2.9 g/cm^2
• KE margin	55%
• Velocity	3.1e7 cm/s

Fig.2.4.1 A 400 MJ (nominal) high-yield direct-drive target

2-D Stability Studies

Fig. 2.4.2 illustrates the major critical issues in the design of a high-gain direct-drive target. Of these, target stability is probably the greatest source of concern. Success with direct-drive targets for IFE will depend fundamentally on our ability to achieve Rayleigh-Taylor stabilization through full compression and burn. Note that "success" is defined as (a) achieving an ignited hotspot at the center of the compressed field with conditions of ρ-R ~0.3g/cm^2 at an ion temperature of ~10-12keV, and (b) a surrounding cold, compressed fuel mass of ~3 g/cm^2 for adequate fuel burn-up and gain.

Laser-target coupling	Ü	*Beam geom., intensity, l, ablator design (scale lengths)…*
Target isentrope control (ablator/fuel)	Ü	***Pulse shaping…***
Implosion symmetry (low modes)	Ü	*Beam geometry and balance…*
Implosion stability (higher modes)	Ü	*Laser imprint, inner/outer surface finish, target build, adiabat control..*
Ignition and propagating burn	Ü	*All of the above!*

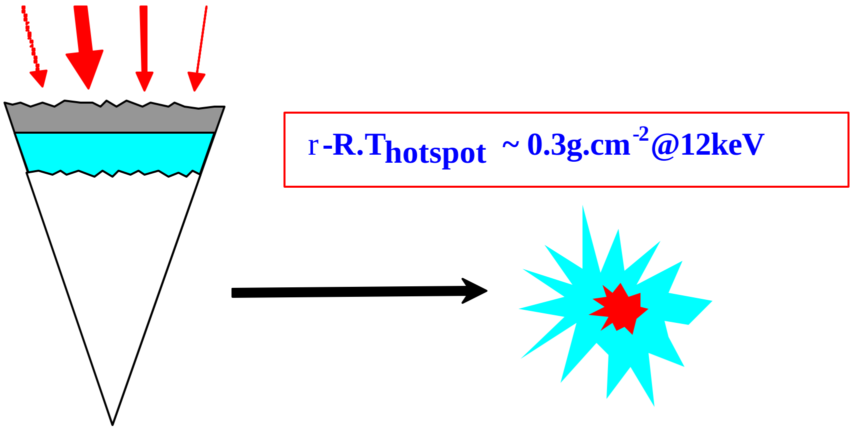

Fig. 2.4.2 Critical issues in the design of a high-gain direct drive target for inertial fusion energy

We have achieved considerable success this year in the coupling of the isotrope control (Fig. 2.4.2) with implosion stability. Such "adiabat tailoring" is achieved by optimizing the driver pulse shape as follows: High fuel gains and minimum drive energies for ignition, E_{ign}, result from producing a low adiabat α as:

$$E_{ign} \sim \alpha^{1.8} v^{-6} ? P^{-0.8}$$

where α is the ratio of the plasma pressure to the irreducible Fermi degeneracy pressure. Now obtaining a high ablation velocity V_A is a key attribute in reducing the Raleigh-Taylor growth rates γ_{RT} where:

$$\gamma_{RT} \sim c_1 \sqrt{(Akg)} - c_2 k V_A k$$

But ablation velocity increases with increasing adiabat α?as:

$V_A \sim (dm/dt)/\rho$?~?$\alpha^{3/5}$?

The solution to this conundrum – i.e the requirement of a low adiabat for ignition and gain but a high adiabat for high ablation velocity and good stability – is realized by tailoring the adiabat profile through the ablator and fuel. The laser pulse shape is modified from the conventional continuous foot pulse by producing a large prepulse ("picket stake") at time zero after which the laser turns off for several ns. The prepulse launches a high initial shock in the ablator that decays as it reaches the fuel. The subsequent resumption of the foot pulse is timed to catch up with the decaying shock at the inside fuel radius. Thus, the ablator is set on a high adiabat giving high ablation velocity while the fuel is maintained on a low adiabat.

Fig. 2.4.3 shows three pulse shapes we have used in LASNEX 2-D stability studies of this phenomenon, normalized to the same peak power. Pulse shape A (black curve) has a standard foot pulse, pulse shape B (red curve) has a modest prepulse (20% of the peak drive power but only 0.65% of the total drive energy), pulse shape C (blue curve) has a large prepulse (20% of the peak drive power and 2.1% of the total drive energy).

Fig. 2.4.4 compares the resulting adiabat profile through the fuel and ablator for pulse shapes A and C; both profiles were obtained at a time when the main pulse had reached 30% of its peak height. Note that the standard pulse shape achieves approximately an adiabat of unity throughout the fuel and ablator. By contrast, the large prepulse produces a high adiabat =6 in the ablator, yielding high ablation velocities, while relaxing to ~1-2 in the fuel. As shown below, these higher adiabats provide for considerable improvement in stability but at the expense of some increase in laser energy and somewhat reduced gains.

7

Fig. 2.4.5 illustrates the result of applying the picket stake pulse shapes where single-mode growth factors (e-folds) for the target shown in Fig. 2.4.1 above are plotted versus spherical mode number, $l = \pi r(t)/\lambda(t)$, for the three pulse shapes shown in Fig 2.4.3. Note that at spherical mode numbers around l ~ 100, growth factors have been reduced from ~11.5 (standard pulse shape, A) to ~6.5 e-folds (tailored pulse shape with large prepulse, C). These reduced growth factors are comparable to those seen for targets indirectly-driven with uniform temperature x-ray sources (e.g. heavy-ion IFE targets).

The 2-D growth factors for the standard pulse A are seen to be in good agreement with the semi-analytic Betti-Goncharov 1-D model plus Bell-Plesset convergence. However, this model does not fit the tailored adiabat results so well (the dashed lines are merely linear interpolations between the 2-D data points); we believe we understand why this is so and are investigating methods to modify the model.

The impact of these growth factors on late time target breakup are shown in Table 2.4.1 Here, we apply the non-linear, multimode saturation model of Haan using an initial roughness spectrum based on present NIF specifications. Note that late-time shell breakup — i.e., Rayleigh-Taylor bubble amplitude divided by shell thickness – has been reduced from ~80% for the standard pulse shape to a negligible 2% for the tailored pulse shape. Also, as shown in the table, the penalty for this much improved stability is higher drive energy and somewhat reduced gains.

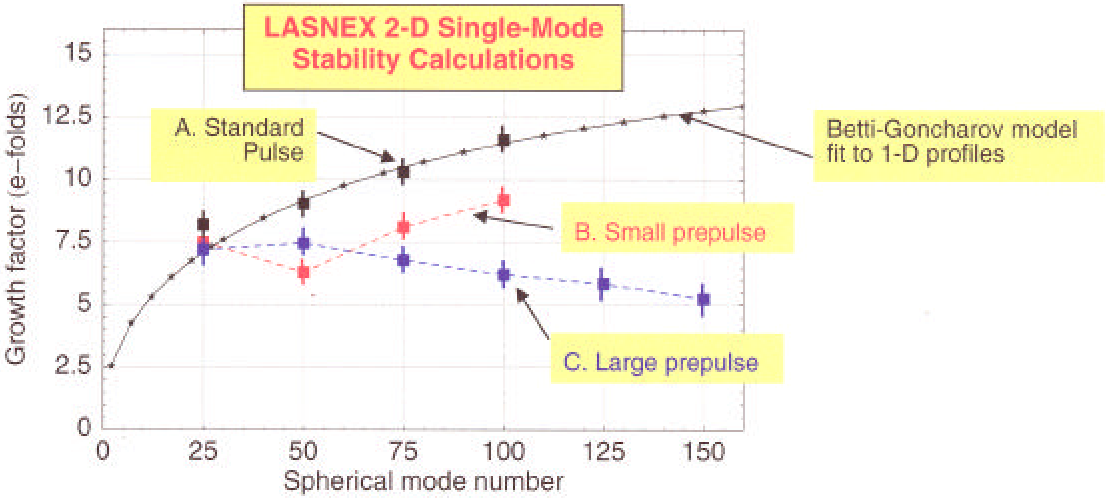

Fig. 2.4.5 2-D single mode growth factors obtained from Lasnex plotted versus spherical mode number for the laser three pulse shapes shown above.

Table 2.4.1 Target 2-D performance with tailored adiabat pulse shaping.

Pulse Shape	Laser Energy (MJ)	Target Yield (MJ)	Gain	Shell Breakup Fraction
A. Standard	2.4	430	180	0.83
B. Small prepulse	2.5	420	170	0.21
C. Large prepulse	3.1	360	110	0.02

2.5 Table of Deliverables and Accomplishments

3.1 DPSSL DEVELOPMENT	***Deliverable:***	***Accomplishment:***
3.1.1 Build Two Pump Delivery Systems		
3.1.1.1 Diode tiles	Produce and characterize 150 tiles	100% Completed
3.1.1.2 Pulsed power and control system	Installation and full operation of at least 1×10^5 shots for 144 tiles with upgraded control system	100% Completed. Control system upgraded and backplanes 1-8 operated.
3.1.1.3 Pump delivery system	Full characterization and assembly of two pump delivery systems	25% Completed. Pump delivery hardware was designed. Fabrication and installation delayed.
3.1.2 Fabricate Yb:S-FAP Crystals		
3.1.2.1 Crystal growth (Northrop-Grumman)	Produce at lease one high optical quality crystalline boule, with three as goal	100% Completed. Produced three boules One has good optical quality.
3.1.2.3 Crystal growth (LLNL)	Produce seven high optical quality crystalline boules.	100% Completed. Produced 16 boules. Nine have good optical quality.
3.1.2.4 Crystal fabrication	Produce seven bonded and coated full-size 4x6 cm^2 Yb:S-FAP crystals	100% Completed 7 slabs with some slabs slightly undersized. 5 installed in amplifier.
3.1.3 Build Second Wedged Amplifier Head		
3.1.3.1 Wedged amplifier cassette	Activation of second amplifier head with seven Nd:glass surrogate slabs and evaluate flow performance.	40% Amplifier hardware was designed and fabricated. Offline tests conducted. Installation delayed.
3.1.4 Build Full Scale Reverser		
3.1.4.1 Reverser hardware	Installation of injection and reverser hardware into mail beamline	25% Reverser hardware was designed. Fabrication and installation delayed.
4.1.4.2 Full-aperture Pockels cell demonstration	Integrate full aperture Pockles cell into reverser system	100% Completed. Pockels cell installed into beamline and operated. Extinction of 200:1 was achieved. Wavefront was 0.15 λ.
3.1.4.3 Kilowatt IRE class Pockels cell design	Complete conceptual design of IRE aperture (10x15 cm^2) Pockels cell and high voltage driver	100% Completed. Two designs were scoped and documented
3.1.5 Integrated Tests and Code Benchmarking		
3.1.5.1 Integrated system performance	Integrated operation of the laser system at 20 J and 10 Hz with Yb:S-FAP slabs in one head.	100% Completed. Demonstrated 21 J at 10 Hz.
3.1.5.2 Diagnostics packages	Full integration of diagnostics packages with laser and control systems	100% Completed. Temporal, nearfield, farfield, darkfield diagnostics all implemented. Two sets of damage diagnostics implemented
3.1.5.3 Ray trace and propagation codes	Comparison of experimental and theoretical predictions	90% Completed. Ray trace, energetics, and propagation codes benchmarked with data. Thermal wavefront codes written.
3.1.6 Advance Yb:S-FAP Crystal Growth	Report on whether these methods offer a pathway to large aperture Yb:S-FAP crystals	100% Completed. One 5 cm LLNL boule grown and three 6.5 cm Northrop boules grown. HEM growth method not as promising at this stage.
3.1.7 Facility Upgrades	Full installation, operation and interface of diode chillers and helium gas blower to control system	25% Completed. Chillers installed and facility layout completed. Full installation delayed.

3.2. CHAMBERS DEVELOPMENT	***Deliverable:***	***Accomplishment:***
3.2 Chamber		
3.2.1 Magnetic Protection		
3.2.1.1	Install and learn to operate LSP, a 3D PIC code, on the PC. Work with Mission Research personnel to generate a relevant geometry input file and select the appropriate cross section libraries.	100% Completed. We have successfully installed LSP and completed several test cases. We have worked closely with Mission Research Corporation to obtain realistic 1D, 2D (x vs y and r vs z) and 3D geometries.
3.2.1.2	Benchmark LSP results against those obtained previously by John Perkins in collaboration with General Atomics.	Incomplete. Due to personnel changes at General Atomics, access to the previous code and results is not possible. Instead, we have started to benchmark LSP against published analytic calculations and experimental results (see section 3.2.1.9 below).
3.2.1.3	Calculate the time-of-flight spread of the burn and debris ions at the first wall. Compare these results to those obtained by LASNEX and BUCKY.	100% Completed. We have developed a basic "shell" model using LASNEX data and have used this model to provide input to LSP. This model uses simple "time-of-flight" calculations to determine the initial plasma species density and energy profiles.
3.2.1.4	Use LASNEX to examine the extent of gas ionization and its effect upon the charged particle stopping power.	100% Completed. LASNEX has been used to model the transport of target ions through 6.5 m of xenon gas at 10 mTorr. We find that the debris ions are stopped, but that the burn ions are largely unaffected. Stopping of the debris ions generates additional x-rays, which must be addressed.
3.2.1.5	Run Lsp for a case with an ideal magnetic field (mirror) and vacuum conditions. Calculate charged particles trajectories, collection efficiency, confinement time, and fluxes at the exit ports as a function of time and magnetic field strength.	35% Completed. We have started using LSP to model plasma expansion into a vacuum with a uniform magnetic field. We have also started calculations to determine the plasma axial confinement time and the required size of the axial exit holes. This work is ongoing.
3.2.1.6	Perform shielding, nuclear heating, radiation damage, and neutron activation calculations for NbTi superconducting magnets. Estimate total cold mass, cooling requirements, radiation lifetime, and radioactive waste.	100% Completed. Neutron/gamma-ray shielding and activation calculations were completed for the baseline, uniform field coil configuration. Results indicate that radiation damage and nuclear heating are unlikely to be a significant constraint.
3.2.1.7	Use OPERA3D to generate the mesh for the external field resulting from various coil configurations.	100% Completed. We have successfully integrated magnetic fields generated by OPERA3D/TOSCA into LSP. We have calculated coil configurations to produce a nearly uniform (~1% variation) magnetic field. The design would use seven large but simple loop coils. This set of coils provides the magnetic field for our LSP benchmark results.
3.2.1.8	Use the Vector Fields code SCALA in an iterative fashion with OPERA3D to include effects that the expanding plasma ball will have upon the external magnetic field. Update the results obtained in tasks (3.2.1.5) and (3.2.1.7).	100% Completed. LSP self consistently calculates the magnetic field taking into account the magnetic field provided by external coils and the expanding plasma. This task does not require SCALA. SCALA will be used to compare with LSP in regions where collective plasma effects and collisions are negligible.
3.2.1.9	Propose experiments and calculations that could be performed to benchmark LSP.	100% Completed. We are proposing to utilize the0 Large Plasma Device Upgrade (LAPDU) at UCLA to study plasma expansion in a magnetic field. Initially, we will examine radial and axial expansion in uniform magnetic fields from 0.05 to 0.4 T. We will use these results to assist in benchmarking LSP and to compare with previous experiments. We will then examine the effects that various levels of background plasma may have on these expansions. Some experimental results already obtained by M. VanZeeland at UCLA appear quite promising.
3.2.1.10	Report with risk/benefit analysis and recommendations for future work, if any.	35% Completed. Results have been reported at HAPL Program meetings. Report has not been written, as the design is not sufficiently mature.

3.2.2 Fast Ignition	***Deliverable:***	***Accomplishment:***
3.2.2.1	Continue literature review including gathering most recent info from IFSA2001 conference that features several papers on the subject.	100% Completed. Completed detailed literature search including the most recent conferences featuring papers on the subject, such as IFSA2001 and the 5th Workshop on Fast Ignition of Fusion Targets in Madeira, 2001.
3.2.2.2	Obtain best estimate of DT ice surface roughness that can be tolerated.	100% Completed. Revisited work from target designers at LLNL for tolerable surface finish for IFE targets. Results show that high yield targets may be less unstable than low yield ones and may be less susceptible to surface perturbations fed-out from initial ice roughness.
3.2.2.3	Consult with General Atomics on target fabrication issues.	100% Completed. Consulted with target fabrication experts on FI specific issues and opportunities. Ongoing work at GA is investigating the possibility to stamp hard-frozen DT hemispheres and "weld" them together.
3.2.2.4	Assess the laser pointing and timing requirements and the implications for target injection, tracking and beam steering.	100% Completed. Target tracking and timing precision should be similar to hot-spot ignition for compression beams. The ignitor beams should be triggered off of the compression beams with a fixed delay. One should be able to use movable mirrors at the low power end of system for pointing of the ignitor beams, similarly to the technique used for pointing the compression beams.
3.2.2.5	Complete basic beam and chamber layout.	75% Completed. We have used a systems code to study the number of ignitor beams that would be required as a function of their size, location, and spot size requirements.
3.2.2.6	Evaluate of potential for directional target output and its effects upon the chamber and optics if the cone-focused target is used.	50% Completed. In the case of the cone focused FI target, debris may be directed back at the ignitor beam final optics. Development of large-diameter diffractive optical components that are "robust" is needed.
3.2.2.7	Assess chamber design implications of FI target emissions compared to direct drive targets.	75% Completed. For optics that are 2× diffraction-limited and a spot size of 33 µm, even 1-m-diameter optics result in an optic stand-off distance of only ~13 m. At such a short distance, the optics will be in an extremely harsh environment and multiple protection techniques are likely to be needed.
3.2.3 Safety and Environment		
3.2.3.1	Provide neutron and gamma-ray transport and activation calculations for the magnetically protected chamber design concept.	75% Completed. Neutron transport and activation calculations were performed for the baseline, uniform field magnet layout.
3.2.3.2	Provide neutron and gamma-ray transport and activation calculations for either a direct conversion system or ion dump.	Incomplete. Due to slow progress in task 3.2.1.5, it is premature to begin design of the ion dump.
3.2.3.3	Provide the Materials Working Group with ongoing support in the selection of chamber and target materials.	100% Completed. We provided target designers with guidance on the selection of target materials. Also, we addressed different options for waste disposal of IFE power plant components.
3.2.4 Radiation Damage Modeling for Chamber Materials		
3.2.4.1	Calculate activation energies for hydrogen and tritium transport and detrapping in graphite.	100% Completed. Calculated hydrogen detrapping from vacancies.
3.2.4.2	Calculate migration and binding energies of H with vacant sites, single vacancies and vacancy clusters, as well as migration energies of defects, vacancies and interstitials, produced during irradiation.	50% Completed. Vacancy-related properties have been completed.
3.2.4.3	Compare values calculated in task (2) to experimental measurements whenever possible and to those values used in trapping models such as the two-region model of A.A. Haasz, et. al	50% Completed. Hydrogen vacancy binding energies found to be 3.2-3.8 eV versus experimental values of 2-3 eV from the literature.

	Deliverable:	*Accomplishment:*
3.2.4.4	Perform ab initio calculations for single defects in order to validate the empirical potential.	25% Completed. Calculated equilibrium structures of pristine graphite. Electronic structure calculations of defect structures and system-size-dependence of defect energy are pending.
3.2.4.5	From molecular dynamics, calculate threshold displacement energies for graphite	100% Completed. Threshold energy for formation of a vacancy was found to be 15 eV.
3.2.4.6	Using the threshold displacement energies (calculated in task (5)) in conjunction with the Kinchin-Pease formulation, estimate the total number of defects produced. Perform calculations for displacement cascades at higher energies to test the validity of the Kinchin-Pease approximation.	75% Completed. Calculated defects, according to Kinchin-Pease model, for recoil energies of up to 2 keV. Higher energy recoil calculations are pending.
3.2.5 Systems Modeling		.
3.2.5.1	Update and improve DPSSL model. Include beam smoothing, improve extraction model, and consider different architectures	35% Completed. Code structure and logic reorganization completed. Existing modules ported to new structure. Improved optimization package added. Debugging of subroutines incomplete
3.3 Final Optics		
3.3.1 Gamma and Neutron Irradiation Studies		
3.3.1.1	Complete the analysis and write a detailed journal article on the deployment of a SiO_2 final optic.	100% Completed. Article submitted to and accepted for publication in *Fusion Science and Technology*. Tentative publication date is June 2003.
3.3.1.2	Complete the irradiation studies of the Al_2O_3 and MgF_2 transmissive optics, and the 3ω, 4ω and aluminum mirrors. Examine materials for scattering and absorptive losses. Develop models of defect formation and final optic operation.	50% Completed. Gamma-ray irradiation studies completed. Samples have been sent to ORNL for irradiation in HFIR facility.
3.3.2 Molecular Dynamics Simulations of Neutron-Induced Defects		
3.3.2.1	Complete the Molecular Dynamics Simulations of SiO_2, including: systematic calculations of defect generation versus the neutron impact energy, varying the amount of overlap of collisional cascades and increased primary knock-on collisional energy.	100% Completed. Demonstrated defect generation and radiation self-annealing effect. Provided sections for journal article mentioned in 3.3.1.1.
3.3.2.2	Begin evaluation of the neutron-induced damage of aluminum mirrors.	100% Completed. Determined that implementation of Al-O hybrid potentials (for modeling of surface effects on subsurface defect formation and migration) would be feasible.

3.3.3 Rep-Rated X-ray Ablation	***Deliverable:***	***Accomplishment:***
3.3.3.1	Form the x-ray abalation Steering Committee to assist in setting of program priorities.	100% Completed. Committee has assisted in prioritization of irradiation schedules. Tungsten will be the first chamber material studied, and aluminum will be the first optical material.
3.3.3.2	Develop detailed experimental plan and an exit strategy.	100% Completed. Plan was developed prior to issuing the contract. Decision was made to procure a star-pinch-based x-ray source. A laser-based source was considered but ruled out due to development needs, concerns about system availability, and concerns about the source's ability to provide adequate x-ray fluence.
3.3.3.3	Procure, install, and operate the PLEX or related x-ray irradiation facility using nitrogen and xenon fill gases to produce x-rays at 113 and 430 eV.	90% Completed. Contract was placed in April 2002. Equipment arrived on-site in early-October, and full installation was completed by the end of October. Source has been operated, at up to 3 Hz, for $>10^4$ pulses at a time. Operation has only occurred with xenon gas, which produces x-rays at 113 eV.
3.3.3.4	Equip x-ray source with a suite of real-time diagnostics for characterization of the pinch and x-ray output. Obtain and/or identify available facilities for pre- and post-irradiation analysis of samples.	75% Completed. Appropriate equipment has been identified. Photodiode, CCD camera, and phosphorescent materials are currently used for on-line characterization of the x-ray output. X-ray spectrometer was received in December 2002.
3.3.3.5	Upgrade ABLATOR x-ray deposition model with coupling to a Monte Carlo particle transport code.	100% Completed. Rather than coupling directly to a Monte Carlo transport code, we have built the direct-drive IFE x-ray output spectra directly into ABLATOR.
3.3.3.6	Characterize x-ray output (spectrum and pulse length) for the two fill gases with and without filters. Characterization must include repeatability.	50% Completed. Operation with xenon (113 eV) was characterized by vendor. On-site spectral measurements will be completed in December. Repeatability measurements will be performed once optic has been replaced and/or repaired.
3.3.3.7	Complete an experimental campaign for two leading materials in either the optics or chamber wall arena as suggested by the Steering Committee.	25% Completed. Due to delays in funding and procurement, equipment was not installed until the end of October 2002. Aluminum tests have been conducted, using powder met samples, at low fluence (~0.1 J/cm^2). This fluences provides a surface temperature rise of ~220 °C per pulse. This exceeds the temperature rise resulting from the prompt x-rays in the IFE case (~45 °C).On-site testing indicates that the condensing optic is not properly focusing the beam. Effort has been directed towards fixing this problem.
3.4 Target Physics	Provide documentation of direct-drive target performance in terms of gain, threat spectra, and the utility of metal film..	90% Completed. Wavelength dependence of target design for DPSSL driver deferred to following year. Adiabat tailoring investigated instead. Results show successful results in terms of target stability.

3. PROGRAM PLAN DESCRIPTIONS

3.1 DPSSL DEVELOPMENT

3.1.1 Fabricate Yb:S-FAP Crystals

Crystals will continue to be grown both at LLNL and at Northrop-Grumman. The emphasis this year will be on growing crystalline boules at each facility which are large enough in diameter (> 6 inches) to harvest two full-size crystalline slabs. The growth of larger diameter boules will be challenging and therefore a growth parameter matrix involving thermal gradients, doping, cool-down, pull, rotation and growth rates will be worked through. The goal of the FY03 effort is to produce one full-size (4 x 6 cm^2) high optical quality crystalline slab from each facility.

3.1.1.1 Crystal growth (Northrop-Grumman)

The current contract will be continued with Northrop-Grumman to produce 6 inch diameter crystalline boules from their Czochralski (CZ) furnaces. The crystals will be fully characterized in terms of doping, wavefront, and spectroscopic requirements.

3.1.1.2 Crystal growth (LLNL)

One furnace will be upgraded and dedicated to producing 6 inch diameter crystalline boules. This large-growth furnace will be provide a parallel effort to the Northrop contract to understand the impact of thermal gradient, doping, gas-purge, and rotation rate on the crystalline quality in that information learned at LLNL will be shared. The goal is to reduce core and surface defects. Power supplies will be upgraded on all furnaces to allow for more stable growth conditions.

3.1.1.3 Crystal fabrication

After each crystal has been shown to meet Mercury specifications, it will be precision shaped, bonded, anti-reflection coated, and mounted with edge cladding into the aluminum vane elements. Seven crystals will provide a full amplifier assembly. Existing crystals will be remounted with lower doped edge cladding, bubble-free uropol, and conductive glue to decrease the heat loading on the edge cladding and uropol. The amplifier assembly will finally be tested under full pumping and high speed gas flow to ensure that flow conditions have not been perturbed.

3.1.1.4 Alternate Bonding Processes

A contract will be placed with an outside vendor to explore “glue bonding” as an alternative process to the high temperature techniques currently used to make full sized crystalline slabs. Preliminary results on first generation parts are encouraging. Proper index matching and uniform layering of the glue between parts will be investigated. Wavefront quality and damage threshold measurements will be made to qualify the process.

3.1.2 Front End Laser

An upgraded front end laser system will be assembled to allow for temporal, spatial, and spectral shaping of the injected beam. The system will employ a fiber oscillator and amplifier, a BBO optical parametric amplifier pumped a Nd:YLF laser and a two pass booster Yb:S-FAP amplifier to bring the output beam energy to 100 mJ in a 3x5 cm^2 rectangular shape with 50:1 temporal contrast and up to 200 Hz of bandwidth. Diagnostics will be implemented at several stages to measure output characteristics and monitor alignment stability.

3.1.3 Full System Activation with Two Yb:S-FAP Amplifiers

The task will involve the activation of the front end, reverser, pump delivery, and two fully populated Yb:S-FAP amplifiers along with the diagnostics packages required to monitor and measure the energy, pulse shape, wavefront, near-field and far-field of the amplified beam. Additional damage detection diagnostics will be implemented to assess the onset of optical damage during the shot to terminate operations. Phase plates will be installed for each amplifier to correct for static wavefront distortions incurred during the bonding process. Experimental data will be benchmarked against ray trace, energetics, and propagation codes. The goal of this milestone is to demonstrate integrated performance with two Yb:S-FAP amplifier heads by producing 70 J of output energy at 1047 nm at 10 Hz repetition rate.

4.1.3.2 Reconfigure and upgrade facility

In order to accommodate the second amplifier the facility must be reconfigured and upgraded to accommodate the new hardware. We will install optical tables, clean room enclosures, and utilities.

4.1.3.3 First amplifier activation

The first amplifier will be fully populated with 7 Yb:S-FAP slabs in order to provide up to 40 J of extracted energy at 10 Hz. To improve the beam quality we will fabricate a phase plate to correct for static wavefront distortions in the system.

4.1.3.4 Second amplifier activation

The second amplifier will be populated with up to 3 S-FAP slabs to allow for up to 60 J of extracted energy for the system at 10 Hz. We will also fabricate phase plates to correct for both static and thermal wavefront distortions.

3.1.4 Controls System and Diagnostics

3.1.4.1 Control system

The current control system will evolve into a distributed control system to allow more reliable and consistent operation and performance of the eight diode arrays. Power control will be developed into a completely distributed system which will be expandable with the size and number of diode bays deployed. Most importantly each major subsection of the control system will operate independently thus allowing future modifications to be made without affecting the balance of the control system.

Each diode pulser bay that control one diode array will have a dedicated controller to set and monitor the power supply and pulsers providing power to the diodes. This configuration will enable much faster operator response and provide an improved method of detecting & correcting pulser faults. Each controller will consist of a PXI chassis without a monitor but with sufficient I/O to communicate with all pulser bay electronics efficiently. All user interactions will be handled by the power control computer and communications with the individual controllers will be performed over Ethernet.

3.1.4.2 Alignment Diagnostics

Closed loop pointing and centering controls will be added to the system to assist keeping the laser aligned during operation. Motorized mounts and electronic cables will be added to several mirrors and existing software will be modified to bring the system online expeditiously.

3.1.5 Wavefront, Frequency Conversion and Diodes

The efficient conversion of the Mercury Laser to the third harmonic will require good beam quality and a frequency conversion scheme the will convert the beam at 10 Hz repetition rate without degradation to the beam quality and efficiency. Wavefront control and frequency conversion designs will be scoped and completed in order to prepare for hardware fabrication and installation the following year.

3.1.5.1 Wavefront Control

Mercury will require wavefront correction for the thermally induced distortions. Wavefront control options will be scoped and a design involving either pre-correction of the injected beam or corrections during the amplification process will be completed. Benchmarked calculations will be used to predict the wavefront distortions and magnitude for the corrections required.

3.1.5.2 Average Power Frequency Conversion

A gas cooled frequency conversion module will be designed. Calculations involving the tradeoff of non-linear materials, expected thermal loading and frequency conversion efficiencies will be performed.

3.1.5.3 Enhanced High Power Diode Tiles

Laser diode bars will be tested at 150-200W/bar levels for $>10^8$ lifetimes. An assessment of the damage mechanisms will be made. Enhanced heatsinking technologies will be explored for IRE performance levels

3.2 Chambers

3.2.1 Magnetic Protection

Due largely to the difficulty of solving this problem computationally, progress in this area has not occurred at the desired rate. Although there are now opportunities to perform scaled experiments at an interesting facility located at the University of California at Los Angeles (the Large Plasma Device Upgrade, or LAPDU), LLNL is electing to close out this activity during FY03. Therefore, the FY03 effort will be minimal and will be limited to detailed documentation of the FY02 effort.

3.2.2 Safety and Environment

During FY03 we will continue to provide safety and environmental (S&E) support to the overall HAPL Program (including the Materials Working Group) as well as to the magnetic protection design effort. We will continue our collaboration with domestic (INEEL) and international (Instituto de Fusion Nuclear, UNED, in Spain) research centers in this area.

Important tasks to be completed as part of the S&E support are:

1. Continue to provide the Materials Working Group with support in both the selection of chamber and target materials and in the determination of threats to chambers and optics. Support will be provided on an as-needed basis.
2. Analyze impact of activation-cross section uncertainties upon neutron activation results.

3.2.3 Radiation Damage Modeling for Chamber Materials

During FY03, we will begin study of the neutron-induced radiation damage in tungsten using atomistic simulations to calculate defect production rates and compare these with experimental results.

1. Begin the implementation of W embedded atom interatomic potentials for MDCASK massively parallel molecular dynamics code.
2. Perform 10-40 keV primary knock-on/recoil calculations for tungsten to determine point and extended defect production rates under IFE-relevant conditions.

3.2.4 Chamber Scaling and Scoping Studies

The Laser IFE program needs an improved, integrated systems modeling capability that includes current understanding of the physics, engineering and costing information for candidate drivers, targets, chambers, and power conversion subsystems. In FY03 we will focus our attention on updating and improving the chamber scaling models for various chambers of interest to Laser IFE. A prime objective will be to develop scaling relations for chambers as a function key operating parameters and design choices. One important example would be to develop the information necessary to determine the chamber first wall radius as a function of target yield (including energy partitioning between x-rays, ions and neutrons) for candidate first wall materials. Dependence on other chamber design variables, such as the buffer gas density in the case of gas filled chambers, wall operating temperature, pulse rep-rate, etc. would also need to be included. Various constraints must also be considered, such as avoidance of first wall melting and cryogenic target survival.

Eventually, the geometric scaling will provide input to cost scaling calculations, but economic aspects will not be emphasized at this point in the chamber development process. At this time it is more important to develop understanding of key trade-offs in chamber design and provide information on areas that could have high leverage in reducing design uncertainties (i.e., where new data would have the greatest impact) and opening up the potential operating space. Eventually, as we develop fully integrated code with info on the drivers, target performance and balance of plant systems, the systems codes will help direct the Laser IFE Program toward the most attractive overall operating point. The chamber scaling work proposed here is just a single step in that direction.

The chamber scaling work is intended to include currently design approaches (dry walls with and without gas protection and magnetic protected walls) and new ideas as they are developed, thus the scoping studies nature of the task. LLNL will work closely with UCSD and UW to incorporate the chamber physics information resulting from the detailed chamber and first wall response calculations. We will also work with Boeing to assure that the IFE systems code uses assumptions consistent with past ARIES systems modeling where appropriate (e.g., material properties, unit const, etc.).

Tasks for FY03 are:

1. Determine scaling for gas-protected dry wall chamber as a function of target yield (100 – 500 MJ), pulse repetition rate, chamber gas density, and first wall material based on first wall response constraints (e.g., avoiding melting).
2. Determine other possible design and operating constraints and show how these may affect the chamber design and/or the plant operating space (e.g., add constraints on target survival, target tracking, chamber clearing, beam propagating, etc.).
3. Work with UCSD and UW to incorporate results of previously completed chamber scoping studies and advise on additional modeling and calculations needed to developing the chamber scaling equations over the desired range of parameters.
4. Begin assembling framework and database for an integrated Laser IFE systems code.

3.3 Final Optics

3.3.1 Gamma and Neutron Irradiation Studies

We will evaluate the suitability of aluminum mirrors as the final optic in an IFE power plant, and dielectric mirrors as the "secondary" optic (i.e. optic directly before the "final optic"), in terms of their response to γ-rays and neutrons. Two basic types of analyses will be performed: (1) The wavelength dependence and absolute reflectivity of the mirrors will be measured. (2) An interferometer will be employed to determine if the substrate has deformed. These measurements will assist in judging whether the optics can function in an IFE environment. The samples will first be irradiated in HFIR at ORNL where containers will be used to remove the low energy neutrons. The wave front determination will indicate if the substrate has deformed, and the reflectivity measurements will reveal whether the layers in the dielectric mirrors have been altered by the neutrons and gammas. We have established a radiation laboratory, appropriate procedures, personnel training, and health services oversight to perform these measurements.

Tasks to be completed during FY03 include:

1. Determine the operating window of reflective dielectric and aluminum optics that are exposed to gamma and neutron radiation environments relevant to IFE. Samples are to be irradiated at ORNL.
2. Perform post irradiation evaluations of optics in terms of their reflectivity and induced wave front distortions.

3.3.2 Ion Debris Mitigation Study

Protection of the final optics—using magnetic fields and flowing gas—will be assessed during FY03. The ion and x-ray threat assessments will be characterized as a function of the gas species and pressure, and particle transport calculations will be completed. Optics protection systems will be evaluated in a stepwise fashion. We will, for example, consider methods that might be used to stop a class of particles, such as the light ions. Systems applicable to normal and grazing incidence final optics will be considered.

Threat calculations, which will be performed in parallel with mitigation assessments, will assist us in determining what must be protected against. A chief concern is the relatively high sensitivity of the final optics–roughening, for example, may be acceptable for the chamber, while it might be disastrous for the final optic.

Starting from a baseline concept with the highest possible chamber gas pressure, we will calculate the ion fluxes incident upon either reflective or transmissive final optics. Using this, we will estimate the effects resulting from such fluxes and estimate the degree to which the fluxes must be reduced. We will then design a set of deflection magnets each sized to deflect a respective class of ions. Turning towards an engineered ion dump, we will estimate the sputtered fluxes and ion energies. Using these, we will estimate the gas flow required to sweep the beamline free of sputtered material. The effect that the gas will have upon the incident x-rays will be calculated as well.

The following tasks will be completed during FY03:

1. Characterize ion and x-ray threats as a function of gas species and pressure.
2. Develop ion mitigation concept, including, for example, deflection magnets, engineered ion dumps, and gas flow.
3. Propose experiments and/or additional analyses that could validate the models used in the FY03 analyses.

3.4 X-ray Damage Studies

3.4.1 Modeling of Fundamental Mechanisms

In FY03 we plan to continue developing a predictive capability, which can be used to analyze x-ray ablation from optical and chamber wall materials. The ABLATOR code will be further modified to simulate the conditions of both the IFE real case and our experiments on the XAPPER facility.

In addition to ABLATOR, the XAPPER program is making use of the Topaz and Dyna codes. Thermal diffusion calculations, using the LLNL heat transfer code Topaz3d, are performed to determine the temperature profile and history in the target material. These results are compared to those obtained with ABLATOR. Due to the relatively small dimensions for energy deposition, the thermal diffusion plays a major role in keeping temperatures low. Dynamic structural calculations with the thermal results as input are subsequently performed, using the LLNL dynamic structural finite element code, Dyna3d, to determine the stress levels in the wall material. The stress levels are determined from the thermal expansion of the material and from material properties of stress versus strain. Input to the code includes temperature-dependent values of the thermal coefficient of expansion, Young's modulus, Poisson's ratio, and yield strength.

The following tasks will be completed during FY03:

1. Add and benchmark strain and strain rate modules to ABLATOR. Predict stresses based upon stress-strain relations.
2. Benchmark the ABLATOR and Topaz time-temperature profiles against multi-color fiber optic thermometer measurements.

3.4.2 Rep-Rated Exposure of Chamber and Optical Materials

During FY03, activities on the XAPPER facility will be divided between material exposures, pre- and post-irradiation measurement of material properties and condition, and the addition of real-time diagnostics.

Experimental campaigns will be completed for tungsten and aluminum. Each campaign will include a variety of material variations. Tungsten, for example, will be studied in both powder-metallurgy and chemical vapor deposition forms. The latter is a significantly more pure material, and thus, is expected to be more robust against exposure to x-rays. For aluminum, we plan to expose Al-1100, which has been studied by UCSD, as well as single-crystal aluminum. Each campaign will culminate in a long-duration run of ~10^6 pulses.

Pre- and post-irradiation evaluation will be performed for each material. Evaluation techniques range from profilometry to white-light interferometry. During exposure, evaluation will include use of a non-contact fast thermometry system, to be procured from UCSD.

In summary, the following tasks will be completed:

1. Complete experimental campaign for various types of tungsten.
2. Complete experimental campaign for various types of aluminum.
3. Procure and field a non-contact fast optical thermometer (procure from UCSD).

3.5 Target Design

We will optimize IFE direct-drive target design and performance and assess the option of an outer thin Pd overcoat to reduce laser imprint. Target output spectra (burn products, X-rays and debris) will be obtained for various applications for use in assessment studies of wall interaction and damage. We will continue assessment of the impact of 2-D hydrodynamic stabilities on our baseline target design(s) including the coupling of single mode perturbations into the non-linear, saturated regime, full multi-mode analyses and, in particular, the employment of adiabat tailoring through the use of picket stake laser pulse shapes.

4. STATEMENTS OF WORK AND DELIVERABLES

4.1 DPSSL DEVELOPMENT

4.1.1 Fabricate Yb:S-FAP Crystals

4.1.2.1 Crystal growth (Northrop-Grumman)
Statement of work:
Place crystal growth contract with Northrop for large diameter (> 6 cm) crystal growth and help guide operations through bi-weekly conference calls.
Deliverable:
Produce one high quality crystalline boule with three as goal.

4.1.2.2 Crystal growth (LLNL)
Statement of work:
Upgrade all furnace power supplies and convert one furnace chamber to accommodate large diameter (> 6 cm) crystal growth.
Deliverable:
Produce seven high quality crystalline boules and at least one large diameter boule of > 6 cm.

4.1.2.3 Crystal fabrication
Statement of work:
Deliver crystals to Onyx Optics for bonding. Following bonding process, have crystals polished and anti-reflection coated.
Deliverable:
Produce three coated full-size 4x6 cm^2 crystals.

4.1.2.4 Alternate Bonding Processes
Statement of work:
Place a contract with Schott Technologies and explore feasibility of glue bonding as an alternative to diffusion bonding.
Deliverable:
Produce at least one full size, glue-bonded, Yb:S-FAP test piece.

4.1.2 Front End Laser

Statement of work:
Build a front end laser system capable of temporal and spatial shaping of the injected beam.
Deliverable:
Demonstrate output energy of 300 mJ with 20:1 temporal contrast, <10% rms intensity fluctuations, <500 ps pulse-to-pulse jitter, <1.5x diffraction limited beam quality, and 1-10 ns operation flexibility.

4.1.3 Full System Activation with Two Yb:S-FAP Amplifiers

4.1.3.1 Complete and procure full energy and beam size hardware and optics
Statement of work:
Complete design packages for pump delivery, reverser, telescopes, and pinhole assemblies
Deliverable:
Procure and assemble hardware and optics in system for one amplifier operation

4.1.3.2 Reconfigure and upgrade facility
Statement of work:
Install optical tables, clean room enclosures, and utilities to allow for 2 amplifier operation
Deliverable:
Optically align the injection beam through two amplifiers.

4.1.3.3 First amplifier activation
Statement of work:
Install 7 slabs in first amplifier and fabricate phase plates to correct for static wavefront distortions
Deliverable:
Demonstrate 40 J at 10 Hz and up to 1 hour operating times.

4.1.3.4 Second amplifier activation
Statement of work:
Activate second amplifier with 3 S-FAP slabs and fabricate phase plates to correct for static and thermal wavefront distortions
Deliverable:
Demonstrate 60 J at 10 Hz.

4.1.4 Controls System and Diagnostics

4.1.4.1 Control system
Statement of work:
Design and implement distributed control system.
Deliverable:
Demonstrate operation of 4 backplanes with new control system.

4.1.4.2 Backplane wavelength diagnostics
Statement of work:
Design closed loop software controls for backplane temperature stability.
Deliverable:
Demonstrate simultaneous wavelength stability of 4 backplanes to <0.5 nm.

4.1.4.3 Alignment Diagnostics
Statement of work:
Design and implement distributed closed loop pointing and centering controls by addition motorized mirror mount, cabling, and modifying an existing software algorithm to accommodate the Mercury laser architecture.
Deliverable:
Demonstrate operation of closed loop alignment on the injection laser.

4.1.5 Wavefront, Frequency Conversion and Diodes

4.1.5.1 Wavefront Control
Statement of work:
Scope a design involving either pre-correction of the injected beam or correction within the 4-pass system.
Deliverable:
Complete a hardware design package for dynamic (thermal) wavefront correction.

4.1.5.2 Average Power Frequency Conversion

Statement of work:

Perform calculations to assess the tradeoffs between average power non-linear materials for the expected thermal loading and beam quality on the Mercury laser.

Deliverable:

Complete a hardware design package for a gas cooled frequency conversion module.

4.1.5.3 Enhanced IRE High Power Diode Tiles

Statement of work

Explore performance of diode powers for 150-200 W/bar.

Deliverable:

Assess damage mechanisms.

4.2 Chambers

4.2.1 Magnetic Protection

Statement of Work:

Close-out of activities on the magnetically-protected IFE chamber.

Deliverable:

Produce document with full details of design effort to date.

4.2.2 Safety and Environment

Statement of Work:

Provide support to other elements within the HAPL community and assess importance of activation cross section uncertainties.

Deliverable:

Document progress and make recommendations for future work, if needed.

4.2.3 Radiation Damage Modeling for Chamber Materials

Statement of Work:

Initiate study of neutron-induced radiation damage in tungsten.

Deliverable:

Implement interatomic potentials for tungsten and perform PKA calculations to determine defect production rates.

4.2.4 Chamber Scaling and Scoping Studies

Statement of Work:

Develop scaling relationships for IFE chambers as a function of target yield and rep-rate for various first wall protection schemes and materials.

Deliverable:

Report on updated chamber design scaling models.

4.3 Final Optic

4.3.1 Gamma and Neutron Irradiation Studies

Statement of Work:

Perform neutron and gamma irradiations of aluminum and dielectric mirrors at ORNL, and evaluate impact on the optical properties at LLNL.

Deliverable:

Quantitative measurements and analysis of candidate final and secondary mirrors extrapolating to IFE-relevant gamma ray and neutron doses.

4.3.2 Ion Debris Mitigation Study

Statement of Work:

Assess the threat to the final optics posed by incident ions and design a combined magnetic deflection/gas protection system to reduce ion fluxes to a tolerable level.

Deliverable:

Produce a self-consistent ion mitigation concept for the final optic and propose experiments to validate the models used in the analyses.

4.4 X-ray Damage Studies

4.4.1 Modeling of Fundamental Mechanisms

Statement of Work:

Further develop predictive capability by upgrading the ABLATOR code as necessary and validating ABLATOR and Dyna/Topaz code predictions with XAPPER results.

Deliverable:

Use modeling resources to simulate damage induced by soft x-rays and predict behavior of tungsten and aluminum in an IFE power plant.

4.4.2 Rep-Rated Exposure of Chamber and Optical Materials

Statement of Work:

Complete experimental campaigns for tungsten and aluminum, including pre- and post-irradiation evaluation.

Deliverable:

Characterize x-ray damage as function of x-ray fluence and number of pulses using XAPPER facility.

4.5 Target Design

Statement of Work:

(a) Optimize 1-D design and performance including the option of Pa coatings,
(b) Obtain output "threat spectra." for use in wall damage assessments, and
(c) Assess the impact of 2-D hydrodynamic stability through single-mode and multi-mode analyses using picket-stake laser pulses and discrete, 3-D laser geometries.

Deliverable:

Provide documentation of direct-drive target performance in terms of 1-D performance (yields, gains and drive energies), output threat spectra and 2-D stability.

5. COST BY ELEMENT (Total = $8,814,390, 3% rescission)

5.1 DPSSL DEVELOPMENT (Total = $7,476,760)

5.1.1 Fabricate Yb:S-FAP Crystals	**$1,795,760**
5.1.2 Front End Laser	**$522,730**
5.1.3 Full System Activation with Two Yb:S-FAP Amplifiers	**$2,916,640**
5.1.4 Controls System and Diagnostics	**$690,810**
5.1.5 Advanced Components	**$847,600**
Management Overhead	**$703,220**

5.2 Chambers (Total = $269,660)

5.2.1 Magnetic Protection	**$51,410**
5.2.2 Safety and Environment	**$44,620**
5.2.3 Radiation Damage Modeling for Chamber Materials	**$86,330**
5.2.4 Chamber Scaling and Scoping Studies	**$87,300**

5.3 Final Optic (Total = $238,620)

5.3.1 Gamma and Neutron Irradiation Studies	**$112,520**
5.3.2 Ion Debris Mitigation Study	**$126,100**

5.4 X-ray Damage Studies (Total = $564,540)

5.4.1 Modeling of Fundamental Mechanisms	**$144,530**
5.4.2 Rep-Rated Exposure of Chamber and Optical Materials	**$420,010**

5.5 Target Design	**$264,810**

6. TECHNICAL CONTRIBUTORS TO THIS PLAN

Lawrence Livermore National Laboratory
Ryan Abbot (Fusion Materials)
Andy Bayramian (Lead Experimentalist)
Camille Bibeau (Mercury Project Leader)
Don Blackfield (Magnetic Deflection Simulations)
Maria Caturla (Molecular Dynamic Simulations)
Ray Beach (Diodes, Laser Modeling)
Steve Telford (Control System)
Sham Dixit (Phase Plate Technology)
Chris Ebbers (Pockels Cell)
Alison Kubota (Molecular Dynamic Simulations)
Jeff Latkowski (Fusion Materials)
Wayne Meier (Chambers)
Don Blackfield (System Modeling)
Stephen Payne (Associate Program Leader)
Susana Reyes-Suares (Fast Ignition Studies)
John Perkins (Target Physics)
Kathleen Schaffers (Crystal Growth)

LLNL Managers:
Lloyd Hackel (Acting Program Leader for Laser Science and Technology)
John Lindl (Program Manager for MFE and IFE)

Point of Contacts:

Coherent, Inc.(Didoes)
Paul Rudi

Northrup Grumman (Crystals)
Mark Randles

Onxy Optics, Inc. (Diffusion Bonding)
Oliver Meissner

Directed Energy Inc. (Pulsers)
Ron Sherwood

Filename: DP_FY_03LLNLHAPL Proposal1.doc
Directory: C:\Documents and Settings\lambert2\Desktop
Template: C:\Documents and Settings\lambert2\Application Data\Microsoft\Templates\Normal.dot
Title: DRAFT
Subject:
Author: Valued Gateway Client
Keywords:
Comments:
Creation Date: 10/25/2005 1:46 PM
Change Number: 7
Last Saved On: 11/4/2005 3:17 PM
Last Saved By: lambert2
Total Editing Time: 10 Minutes
Last Printed On: 11/4/2005 4:41 PM
As of Last Complete Printing
Number of Pages: 104
Number of Words: 31,107 (approx.)
Number of Characters: 177,316 (approx.)